Development of a Global/Local Approach and a Geometrically Non-linear Local Panel Analysis for Structural Design

Scott A. Ragon

Dissertation submitted to the Faculty of the

Virginia Polytechnic Institute and State University

in partial fulfillment of the requirements for the degree of

Doctor of Philosophy

in

Engineering Mechanics

Zafer Gürdal, Chair

Michael Hyer

Eric Johnson

Scott Hendricks

Saad Ragab

October 7, 1998

Blacksburg, Virginia

keywords: non-linear analysis, postbuckling, stiffened panels, design optimization

Development of a Global/Local Approach and a Geometrically Nonlinear Local Panel Analysis for Structural Design

Scott A. Ragon

(ABSTRACT)

A computationally efficient analysis capability for the geometrically non-linear response of compressively loaded prismatic plate structures was developed. Both a "full" finite strip solution procedure and a "reduced" solution procedure were implemented in a FORTRAN 90 computer code, and comparisons were made with results available in the technical literature. Both the full and reduced solution procedures were demonstrated to provide accurate results for displacement and strain quantities through moderately large post-buckling loads. The full method is a non-linear finite strip analysis of the semi-analytical, multi-term type. Individual finite strips are modeled as balanced and symmetric laminated composite materials which are assumed to behave orthotropically in bending, and the structure is loaded in uniaxial or biaxial compression. The loaded ends of the structure are assumed to be simply supported, and geometric shape imperfections may be modeled. The reduced solution method makes use of a reduced basis technique in conjunction with the full finite strip analysis. Here, the potentially large set of non-linear algebraic equations produced by the finite strip method are replaced by a small set of system equations. In the present implementation, the basis vectors consist of successive derivatives of the non-linear solution vector with respect to a loading parameter.

Depending on the nature of the problem, the reduced solution procedure is capable of computational savings of up to 60%+ compared to the full finite strip method. The reduced method is most effective in reducing the computational cost of the full method when the most significant portion of the cost of the full method is factorization of the assembled system matrices. The robustness and efficiency of the reduced solution procedure was found to be sensitive to the user specified error norm which is used during the reduced solution procedure to determine when to generate new sets of basis vectors.

In parallel with this effort, a new method for performing global/local design optimization of large complex structures (such as aircraft wings or fuselages) was developed. A simple and flexible interface between the global and local design levels was constructed using response surface methodology. The interface is constructed so as to minimize the changes required in either the global design code or the local design codes(s). Proper coupling is maintained between the global and local design levels via a "weight constraint" and the transfer of global stiffness information to the local level. The method was verified using a simple isotropic global wing model and the local panel design code `PASCO`.

Dedication

The author wishes to dedicate this work to the memory of his father, Hugh C. Ragon.

Acknowledgment

The author wishes to express his sincere appreciation to his advisor, Dr. Gürdal, for his guidance and support during the course of this research. He is also grateful to Drs. M. Hyer, E. Johnson, S. Hendricks, and S. Ragab for their time spent serving on the advisory committee.

The author would also like to express his deepest appreciation to his mother, Karen Burnett, and her husband, Ron Burnett, for their suppport and encouragement.

Portions of this research were supported by the NASA-Langley Research Center, the Air Force Office of Scientific Research, and the McDonnell Douglas Corporation. This support is gratefully acknowledged.

Contents

List of Figures

List of Tables

Chapter 1

Introduction

In recent years, structural design optimization methods have seen increasing use in the aircraft industry. The need for weight efficient and cost effective structures has led to the use of mathematical optimization techniques both in the overall (global) design of large scale structures, such as complete wing boxes or fuselages, and in the detailed (local) design of individual structural elements, such as stiffened panels.

Optimization algorithms have been incorporated into large finite element based structural analysis codes and capabilities have been developed that allow designers to obtain minimum mass wing and fuselage structures subject to a wide variety of global level constraints. One example of such a global design code is the Aeroelastic Design Optimization Program (`ADOP`) developed by the McDonnell Douglas Corporation [1]. `ADOP` allows minimum weight global wing structures to be obtained subject to strength, displacement, vibration, and flutter constraints. Optimized designs are obtained by varying the thicknesses and cross sectional areas of the finite elements comprising the global model.

Because of the large size of the typical global finite element model, it is usually not practical to model individual structural elements (such as skin, spar, and rib panels) with a high level of detail. For example, an individual stiffened panel is often modeled using membrane finite elements to represent the panel skin and rod finite elements to represent the stiffeners and stringers. The neglected local panel details (such as stiffener height, flange thickness, laminate stacking sequence etc.) are, of course, important to the final wing design; local analysis and design methods must be used to obtain them. Over the years, numerous local panel design optimization codes have been developed which allow these details to be obtained. One example is the Panel Analysis and Sizing Code (PASCO) [2]. Using this code, local panel details such as cross sectional shape, stiffener spacing, ply thicknesses, and ply orientations may be obtained subject to strength and bifurcation buckling constraints. In order to obtain a consistent and complete wing design, it is desirable to link the global design level with the local design level(s) in some manner. This is typically accomplished by constructing specialized interfaces between the global design code and the local design code(s).

The present work addresses two different aspects of the global/local wing design problem. The primary aspect of this work is the development of a local panel analysis code for the geometrically non-linear response of wing panels and other linked plate structures. Many of the currently existing local panel analysis codes (such as PASCO) are based on linear analysis of the structure; designs obtained using these codes are often overly conservative (heavy). Codes based on non-linear analysis, on the other hand, are often computationally expensive. The goal of the present work is to develop a cost effective non-linear analysis tool that is both accurate and efficient enough to be used in the global/local design process. In the secondary portion of the present work, a new method for performing global/local optimization is proposed and tested. The proposed interface is based on response surface approximation techniques and allows the global design code to interact with a variety of local design codes in a flexible and efficient manner.

1.1 Geometrically Non-linear Analysis of Prismatic Plate Structures

An analysis capability for the geometrically non-linear static response of prismatic plate structures is developed. This analysis is based on a non-linear finite strip method similar to that described in [3], and is applicable to structures, such as stiffened panels or box columns, which can be modeled as assemblages of finite length prismatic plate strips. In an attempt to reduce the potentially high computational cost of the non-linear finite strip method, reduced basis techniques similar to those described in [4] and [5] are investigated. The objective of this portion of the work is to develop a geometrically non-linear local panel analysis package suitable for use in conjunction with an appropriate optimization code (such as a genetic algorithm). Such an analysis code/optimization code pairing could then be used as the basis for an effective non-linear local panel preliminary design code.

The types of structures considered in the present work are thin-walled prismatic compression members found, for example, in aircraft wing structures (skin, spar, and rib panels) or civil engineering applications (open and closed section columns). Structures of this type are often analyzed and designed using a bifurcation buckling analysis, where the lowest eigenvalue obtained from the buckling analysis is assumed to correspond to the maximum load that the structure may withstand. There are two potential drawbacks to this design approach, however. First, because of inevitable geometric or loading imperfections, the structural response of the real structure will often be non-linear from the onset of loading. In some cases, the structure may collapse at loads well below the theoretical buckling load. For example, optimized panel designs obtained using a classical buckling constraint often have simultaneous buckling eigenvalues for both global and local buckling modes [6]. Designs of this type are sometimes termed "naive" optimums because interaction between the global and local buckling modes often results in premature collapse of the structure. Secondly, many thin-walled structures are capable of withstanding additional load beyond the theoretical buckling load; if this is the case, the structure is said to have postbuckling strength. A design obtained without taking this fact into account will often be heavier than necessary. In order to accurately predict the load carrying capability of the structure and obtain accurate results from the optimization procedure, then, it is necessary to utilize an analysis that takes into account the effects geometric non-linearities and imperfections.

The analysis presented in this dissertation was motivated by the work of Stoll [7]. Stoll developed a semi-analytical method for the geometrically non-linear analysis of prismatic plate structures composed of linked plate strips. The structures were assumed to be simply supported at the longitudinal ends and were allowed to have a variety of support conditions at the side boundaries. Stoll's analysis utilizes a perturbation approach based on the use of a series of buckling eigenmodes to represent the non-linear displacement fields. The buckling eigenmodes were obtained from the `VIPASA` buckling analysis program [8] (which is incorporated in the panel design code `PASCO` [2]). Stoll's analysis is valid for structures loaded in uniaxial or biaxial compression, and includes the effects of geometric shape imperfections. The method was incorporated into the `FORTRAN` code `NLPAN`, and was successfully applied to several flat plate and stiffened panel configurations. In later work, `NLPAN` was linked to an optimization algorithm by Perry [9], and was successfully used to generate several minimum weight stiffened panel designs. During this study, it often proved difficult to select appropriate sets of buckling modes for a given problem that were robust enough to represent the non-linear displacement field over the entire postbuckling range.

For the present work, an alternative (and possibly complementary) approach for the geometrically nonlinear analysis of prismatic plate structures is investigated. The analysis presented here is based on a geometrically non-linear finite strip analysis. In an attempt to reduce the potentially high computational cost of the full finite strip analysis, the nonlinear displacement fields are expressed using a set of basis vectors which are the derivatives of the nonlinear finite strip solution vector with respect to a loading parameter, λ. These "path derivative" derived basis vectors are described in several papers by Noor (see, for example, [5] where they are used in the context of a finite element analysis). As applied to the present research, the path derivative derived basis vectors may lead to solutions that are more easily obtained (especially at higher load levels) than those obtained using basis vectors composed of buckling eigenmodes. This is because the path derivatives are easily re-computed at different points along the load-displacement "path"; the basis vectors may be updated as the solution progresses in order to take into account the changes in the displacement field as the loading is increased. Ultimately, it is envisioned that some combination of the path derivative and eigenmode based basis vectors may lead to the most efficient and robust analysis capability for the geometrically nonlinear analysis of prismatic plate structures.

The theoretical development of the nonlinear finite strip analysis and the reduced basis method is presented in Chapter 3, and results obtained with the analysis are presented in Chapter 4.

1.2 Global/Local Wing Design

In the second portion of the present work, a new methodology for performing global/local design optimization of large wing structures is proposed. A simple but flexible interface between the global and local design optimization levels is constructed using response surface methodology. This interface is structured so as to minimize the changes required in either the existing global design code or the local design code(s). Proper coupling is maintained between the global and local design levels via a "weight constraint" and the transfer of global stiffness information to the local design code.

During global wing design iterations, the global optimizer must satisfy global level constraints (such as displacement and aeroelastic constraints) while minimizing an objective function (usually the total structural weight of the wing). Global design variables usually include such quantities as stringer area and aggregate ply thicknesses. In general, the global model is not detailed enough to accurately represent local panel details and to accurately evaluate constraints at the local level. In order to evaluate these local panel constraints, an efficient local design code is needed. Once an appropriate local design code has been identified, it must be interfaced in some manner with the global design code.

In the conventional manner of performing global/local design optimization, the interface between the local design code and the global design code must be carefully constructed in order to take into account the specific requirements of each code. In the simplest implementations, the operation of the local design code is de-coupled from the global design code (the local code is not provided with any information about how its actions may affect global level constraints).

Such a simple global/local interface is illustrated schematically in Figure 1.1. In this scheme, the global optimizer calls the local optimizer (as a subroutine) whenever information about the local panel is needed. At a given global design iteration, the global design code passes the current global loads to the local optimizer. Given these loads, the local optimizer then iterates until an optimal design is obtained for the local panel. At the end of this procedure, the optimized local panel design is passed back to the global optimizer in the form of various local panel dimensions; these dimensions are then used to update the appropriate global dimensions. One serious problem with this simple procedure is that the local optimizer has no way of determining how its actions affect the global panel design. It is quite possible that when the optimized local panel design is returned to the global level, one or more global level constraints, such as aeroelastic or stress constraints, may be violated. As a result, this arrangement often leads to non-converging and non-optimal results.

The global/local interface proposed in the present work, which is based on response surface techniques, provides a simple and flexible way to avoid these difficulties. A schematic representation of the proposed interface is shown in Figures 1.2 and 1.3. Before the global design iterations begin, the output from the local design code is approximated by a response surface model over appropriate ranges of the loading and stiffness parameters. The local panel optimizations may take into account all local panel details including the stacking sequence design of skin and stiffener elements. Once the global design iterations begin, the global design code interacts with the response surface model, and not directly with the local optimizer. As compared to the procedure illustrated in Figure 1.1, the response surface provides the global optimizer with the information that it needs to continue with the global iterations (constraint values and derivatives), but does not directly modify the global design.

Once the proposed procedure has been implemented at the global level, any number of local design codes may be utilized in the design process without requiring additional changes in either the local or global design codes. The local design code(s) may potentially incorporate

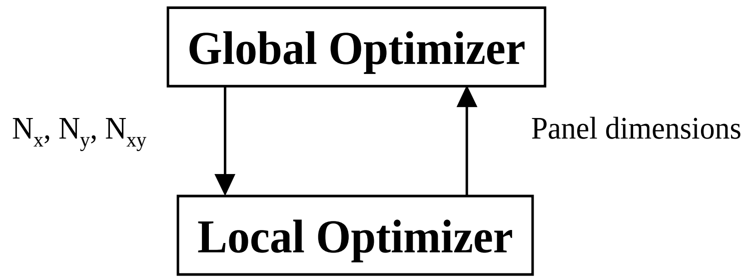

Figure 1.1: Simple global/local interface

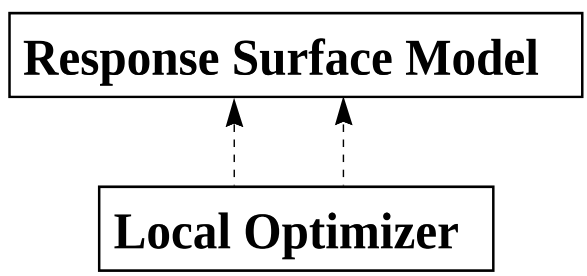

Figure 1.2: Proposed Global/Local Interface - Step 1: *Building the Surface*

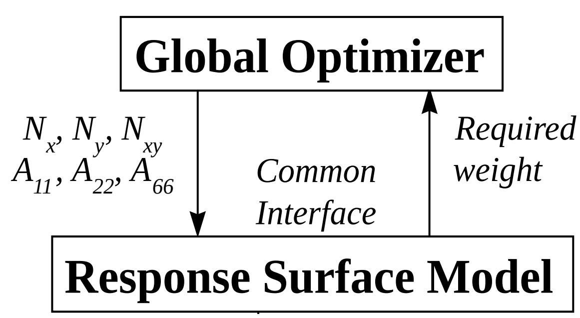

Figure 1.3: Proposed Global/Local Interface - Step 2: *Using the Surface*

a variety of local failure constraints, such as buckling, strength, damage tolerance, and manufacturing and cost constraints while taking into account a variety of local structural details. The proposed procedure is described in more detail in Chapter 5, and sample results obtained with `ADOP` and `PASCO` are presented in Chapter 6.

Chapter 2

Literature Review

In this chapter, a brief survey of the literature relevant to the present work is presented. First, the development and application of the finite strip method, as it pertains to both linear and non-linear analysis, is examined. Next, the development of reduced basis techniques for the solution of non-linear problems is discussed, with particular emphasis on the techniques developed by Noor, et al [4]. Finally, a very brief overview of the work that has been performed in the area of wing panel design optimization in the context of global wing design is presented. Several excellent literature reviews pertaining to the buckling and postbuckling of plates have been presented elsewhere, and are not repeated here. In particular, the reviews presented in [7] and [10] are relevant.

2.1 Finite Strip Analysis

The finite strip method (FSM) is a computationally efficient procedure that may be used to analyze the buckling and non-linear response of rectangular plates and prismatic plate structures. Typical structures that may be effectively analyzed using this method include stiffened panels and box columns. The basic idea behind the finite strip method is to apply the classical Rayleigh-Ritz technique in a piecewise manner to individual sections or "strips" of the complete structure. Each finite strip typically has a length equal to that of the complete structure, but is characterized by a small but finite width. A complex structure may be built up by joining several of these finite strips along their lateral edges in the desired configuration.

In comparison to the related finite element method, which uses simple polynomials to approximate the displacement fields within each finite element, the finite strip method typically uses trigonometric or spline functions to approximate the displacement fields along the length of the strip (which coincides with the length of the structure) and simple polynomials (as in the finite element method) in the transverse direction. The longitudinal functions are chosen to satisfy the boundary conditions at the longitudinal ends of the strip, and the polynomial functions may be used to simulate a variety of boundary conditions at the transverse edges of the strip. As reported in several sources [11], the finite strip method is considerably more efficient than the finite element method when applied to the class of structures considered here.

An excellent overview of the application of finite strip methods to the solution of buckling, vibration, and geometrically non-linear problems is presented in [11], where it is noted that applications of the finite strip method to practical problems may be divided into several broad categories depending on the solution technique and the plate theory used for the individual finite strips. Solution techniques are differentiated depending on whether the governing differential equations are solved directly or indirectly, and depending on whether the displacement fields are approximated in the longitudinal direction using a single term or a series of terms. Plate behavior is either based on classical plate theory (CPT) or some form of shear deformable plate theory (SDPT).

2.1.1 Linear Static, Buckling, and Vibration Analysis

When it was first developed over 25 years ago, the finite strip method was used primarily to solve linear static, bifurcation buckling, and vibration problems. In this section, a brief overview of the major developments of the finite strip method in this context is presented.

In 1968, Wittrick [12] derived in-plane and out of plane stiffness matrices for an isolated plate structure. The plate was assumed to be subjected to a known state of plane stress, and it was assumed that the buckled mode shape varied sinusoidally in the longitudinal direction. As in the method of Kantorovich [13], this assumption allowed the governing partial differential equations to be reduced to ordinary differential equations. In Wittrick's derivation, no explicit assumptions were made regarding the form of the displacement functions in the transverse direction. In solving the governing partial differential equations, the forces and displacements of the component plates were expressed as complex quantities; both shear loading and general biaxial loading were considered. This work was extended by Williams and Wittrick in 1969 [14] to the analysis of built-up plate structures, and then further in 1974 [8] to include the effects of material anisotropy and plate eccentricities. This work culminated in the buckling and vibration code VIPASA [8] that was later incorporated in the panel design code, PASCO [2]. For a given plate structure, VIPASA is able to compute the critical buckling loads or vibration frequencies corresponding to specified buckling half-wavelengths. The component plates may be modeled as balanced and symmetric composite laminates. Classical plate theory (CPT) is used.

The procedure of Wittrick and Williams is sometimes referred to as the "exact" finite strip approach because, for a given buckled half-wavelength, the analysis yields results that are effectively exact as long as there is no applied shear loading. If shear loads are applied, the assumption of sinusoidal buckling modes in the longitudinal direction breaks down, and the analysis loses accuracy. The assumption of sinusoidal buckling modes, of course, implies either that the longitudinal ends of the panel are simply supported, or that the half-wavelength of the buckling mode of interest is much smaller than the overall length of the structure.

In 1968, Cheung [15], [16] first developed what would come to be referred to as the "semi-analytical" finite strip method. The displacement fields in the longitudinal direction were approximated by analytic functions (sin, cos, sinh, cosh) which satisfied the boundary conditions at the ends of the strip. As in the related finite element method, the finite strip displacement fields were approximated in the transverse direction using simple polynomials. Given these assumed displacement fields, the principle of minimum potential energy was used to derive a set of discretized algebraic equations governing the structural response of the individual finite strips. The resulting strips could then be joined along their longitudinal edges to construct the complete structure (in this case, a flat plate). The method was used to perform a linear static analysis for several different isotropic and orthotropic flat plates with both clamped and simply supported ends. The author reported that the computational effort was considerably reduced compared to the finite element method.

In 1973, Przemieniecki [17] developed a procedure similar to that of Cheung, which he used to investigate the local stability of prismatic plate structures. The method of virtual work was used along with standard finite element techniques to derive equations governing the behavior of a single finite strip. As was the case with Cheung, displacement fields were represented in the longitudinal direction using a trigonometric function and in the transverse direction using polynomials. In his development, biaxial loading was admitted, and classical plate theory was used. In developing his method, Przemieniecki's primary intention was to analyze the local instability of prismatic plate structures. Accordingly, he made the assumption that the component plates did not translate in their own plane during buckling and that the junctions between attached plates remained fixed in space. The result of these assumptions is that the allowed modes of deformation of the component plates consisted of rotation about their common edge lines only. For a given buckling half-wavelength, then, results could be obtained using a finite strip whose length was equal to the buckling half-wavelength.

In contrast to the method of Wittrick and Williams (the exact finite strip method), both Cheung's and Przemieniecki's method (the semi-analytical finite strip method) usually require several finite strips placed edge to edge to represent the response of a single component plate. This is because simple polynomials are used to approximate the displacements in the transverse direction and, as in the finite element method, several strips may be required in order to accurately represent the potentially complex structural response in this direction. The stiffness matrices that result are in general larger than those obtained using the exact finite strip method. The advantage of the semi-analytical approach is that the coefficients of the resulting stiffness matrices are linear functions of the load factor, and the resulting eigenvalue problem may be easily solved using existing techniques. In contrast, Wittrick and Williams had to develop a specialized solution technique, as the coefficients of their matrices were complex transcendental functions of the load factor and buckling wavelength [18].

The work of Przemieniecki was extended in 1974 by Plank and Wittrick [18]. They note that while Przemieniecki's kinematic assumptions regarding the allowed deformations of the component plates were valid for local buckling modes, they were invalid for longer wavelength modes, such as torsional or overall modes of stiffened panels. In their work, they relax this assumption and allow for a more complicated state of loading, including transverse loads, shear loads, and axial loads that are allowed to vary linearly across the width of the finite strip. As in the development of the exact finite strip method, the strip loads and displacements are expressed as complex quantities. In the case of applied shear loads, this results in strip stiffness matrices containing complex quantities.

Both Przemieniecki's and Plank and Wittrick's analyses were of the single term type; in each case the longitudinal displacement was represented by a single trigonometric function corresponding to a given buckling half-wavelength. As noted by Graves Smith and Sridharan [19], this assumption restricts the resulting analyses to the case where there is no coupling between buckling modes represented by the various harmonics in the longitudinal direction. In their paper, they represent the longitudinal displacement field as a series of trigonometric functions, each of which has a different half-wavelength. They also abandon the assumption that the pre-buckling stresses are known a priori, allowing the compressive end load to vary arbitrarily in the transverse direction and allowing the pressure loading to vary arbitrarily in the longitudinal direction. The arbitrarily varying compressive load is incorporated by adding a term to the longitudinal displacement field that represents the effects of the resulting pre-buckling displacements, and the arbitrarily varying pressure load is incorporated using a Fourier series. The bifurcation point is obtained using a perturbation method.

In 1971, Cheung and Cheung [20] obtained the vibration frequencies of several stiffened panels using a multi-term approach to allow for other than simply supported end-conditions at the longitudinal ends of the finite strip. They allowed for several different combinations of simple supports, clamped, and free longitudinal ends. This was accomplished by expressing the longitudinal displacement fields in terms of a series of characteristic Euler-Bernoulli beam functions.

Shear deformation plate theory (SDPT) was first incorporated into the finite strip method by Manewa and Davies [21] in 1974 in the context of a linear static analysis. Benson and Hinton [22] used SDPT and a single term approach to solve buckling and vibration problems in 1976.

In 1986, Lau and Hancock [23] analyzed the buckling response of thin-walled plate structures using the spline finite strip method. Instead of using a series of trigonometric functions to approximate the displacement fields in the longitudinal direction, they used a number of B3 spline functions distributed at equal intervals along the strip length. This technique was originally developed by Cheung and Fan in the context of static analysis [24]. This approach allows any number of different boundary conditions to be specified at the longitudinal ends of the panel by slightly modifying a few local splines. Convergence of the solution is obtained by increasing the number of spline functions in the longitudinal direction. Although the spline finite strip method is more versatile than the semi-analytical finite strip method, it is more computationally expensive for the same level of accuracy [11]. In 1989, Lau and Hancock extended their analysis into the inelastic buckling range [25].

Building on the work of Dawe [26] and Morris and Dawe [27], Mohd and Dawe [28] extended the finite strip method to the buckling and vibration of shell structures. Their method is based on the thin shell theory of Koiter and Sanders. They allow the individual finite strips to be fiber reinforced laminates of an arbitrary lay-up, and allow combinations of simply supported, clamped, and free longitudinal edges using the multi-term approach. The longitudinal approximation functions are Euler-Bernoulli beam functions. In the case of simply supported ends, this work was extended to include SDPT in [29].

2.1.2 Geometrically Non-linear Analysis

Many of the structures which are suitable for being analyzed using finite strip techniques (thin-walled prismatic plate structures) tend to behave in a geometrically non-linear manner. Realizing this, several researchers have extended the finite strip technique to take into account the geometrically non-linear response of these structures.

In 1978, Graves Smith and Sridharan [30] used the semi-analytical finite strip method to analyze the post-local buckling response of prismatic plate structures subject to end compression. The displacement fields were expressed as a series of trigonometric terms in the longitudinal direction and using simple polynomials in the transverse direction. In the longitudinal direction, a sine series was used for the non-linear longitudinal (u) and out-of-plane (w) displacement fields, and a cosine series was used for the transverse (v) displacement field. These longitudinal functions are suitable for satisfying the in-plane equilibrium equations and may be obtained from the von Karman plate equations using a perturbation technique [31]. They have a disadvantage when it comes to satisfying the compatibility between attached plates, however. Because v and w are described by different harmonic series, compatibility cannot be maintained at the corners of structures where the plates meet at an angle. In order to resolve this difficulty, the "classical" assumptions of local postbuckling were invoked. These assumptions may be stated as follows [31]:

- The w displacement for each strip is assumed to be zero at strip junctions.
- The transverse stress, σ_y, is assumed to be zero along the edge of each strip meeting at a junction.

These assumptions de-couple the v and w displacements of the attached strips. The first condition implies that the second order in-plane displacements are negligible compared with the out-of-plane displacements, and the second condition implies that the in-plane forces are negligible. These assumptions are considered acceptable for local buckling modes, but are unacceptable for overall buckling modes. In the transverse direction, a linear polynomial was used for the in-plane (u and v) displacement components and a cubic polynomial was used for the w displacement component.

The analysis proceeds by writing the total potential energy in terms of the global degrees of freedom and then invoking the principle of stationary potential energy to obtain the non-linear equilibrium equations. The strain-displacement relations used in this procedure are those of von Karman [32]. An eigenvalue analysis is used to obtain the bifurcation point of the structure, and then the secondary path is obtained using a perturbation method in conjunction with the Newton-Raphson procedure. Results are obtained for isotropic simply supported plates and an open channel section. The authors report that their method displays great computing economy compared with the finite element method.

In 1981, Hancock [33] extended this analysis to consider the non-linear response of imperfect plate strips. Hancock's analysis is of the single-term type (a single term is used to describe each of the displacement components in the longitudinal direction). He claims that this approach results in accurate solutions up to 1.5 times the local buckling load when the wavelength of this single term is the wavelength of the local buckling mode. The longitudinal functions used for the non-linear u, v, and w displacement components are $\sin\cos$, $\sin^2$, and sin, respectively. In the transverse direction, the in-plane displacements are described using linear polynomials and the out-of-plane displacement using a cubic polynomial. As in [30], the assumptions of classical post-local buckling analysis are invoked. The theory of virtual work is used to formulate the non-linear equilibrium equations, which are solved using the Newton-Raphson procedure. Results are presented for square plates and several thin-walled columns.

In 1981, Sridharan and Graves Smith [31] continued their work in this area by comparing results obtained using the classical post-local buckling assumptions with those obtained using a more exact procedure. Results were obtained for several different example problems, including a stiffened panel and a box-column. In this paper, "version 1" utilizes the classical assumptions and is essentially the same method that was presented in [30]. In "version 2", compatibility between strip edge displacements is maintained by representing the v and w displacement fields by the same harmonic function. In this case all three of the u, v, and w displacement components are represented using a sine series. The choice of a sine series to represent the v displacement field implies that the component strips are restrained in-plane at their ends.

The equilibrium equations are obtained using a total potential energy approach and solved using a perturbation approach. It is concluded that version 1 (utilizing the classical post-local buckling assumptions) is more computationally efficient than version 2, but that version 2 is more reliable in advanced postbuckling states where the edge displacements tend to reduce the stiffness of the structure. Using version 2, the elastic collapse of a box column was successfully modeled. It was found that it was necessary to include additional terms in the non-linear strain-displacement equations in order to achieve this. The important terms in this regard were found to be those containing the expression $\partial v/\partial x$.

In 1990, Kakol [34] obtained results using finite strips which approximated the transverse u and v displacement fields using quadratic polynomials and the w displacement field using a fifth order polynomial. He reports that the use of higher order polynomials both improves the accuracy of the results and reduces the computational cost (for a given level of accuracy) compared to the usual (linear and cubic, respectively) approximations for these quantities. The principle of virtual work is used to formulate the governing equations, which are based on the von Karman strain-displacement equations with the addition of $\partial u/\partial y$ and $\partial v/\partial x$ terms. The author notes that it is necessary to retain these terms in cases where the transverse in-plane displacements are of the same order of magnitude as the out-of-plane deflections. This may be true, for example, in a blade-stiffened panel where these terms would prove necessary in order to model the in-plane stability of the stiffeners. In generating results for several stiffened plate models, continuity between the v and w displacements at strip attachment points is maintained.

Azizian and Dawe extended the non-linear finite strip method to include shear deformation plate theory (SDPT) in [35] and [36] where they obtained results for flat Mindlin plates subject to lateral loads and end shortening. The method was extended to flat laminated composite plates with general lamination in [3] (CPT) and [37] (SDPT). This work culminated in [38], where the analysis of prismatic plate assemblies subject to uniform end shortening was performed. The analysis allowed for orthotropic laminated composite materials and results were obtained using both CPT and SDPT. The authors examined the effects of linear, quadratic, and cubic representations for the transverse in-plane displacement fields. They conclude that the linear approximation is much less efficient (for the same level of accuracy) as compared to the higher order representations. Applications include blade and hat stiffened panels as well as a box-column. The classical post-local buckling assumptions are invoked and the results appear to be accurate up to two to three times the critical buckling strain value.

2.2 Reduced Basis Techniques for Non-linear Analysis

An examination of the static load-deflection characteristics of complex structural systems reveals that they are generally no more complicated than those for simpler structures. The large number of degrees of freedom necessary to analyze these structures is primarily a result of the structure's topology and not necessarily a result of complex behavior [5]. Because of this, several methods have been proposed to reduce the total number of degrees of freedom that describe a given structure's response. The general idea is to represent the deformations of the structure using a relatively small number of global shape functions.

Most of the reduction techniques that have been proposed for non-linear analysis combine the finite element technique with the classical Rayleigh-Ritz technique. In this case, the structure is first discretized using finite elements, and then the Rayleigh-Ritz technique is used to represent the structure's response using a small number of basis vectors. The actual selection of these basis vectors varies with the application. In [39], bifurcation buckling modes are used as basis vectors. In [40], the linear solution is used at the beginning of the analysis; as the analysis progresses, "correction" vectors are computed using the residual vector. These correction vectors, along with the linear solution, constitute the basis vectors.

In 1980, Noor and Peters [41] proposed using a set of basis vectors that consist of the nonlinear solution vector at a given load level and the higher order derivatives of the solution vector with respect to a path parameter. These derivatives are the same as those commonly used in the static perturbation technique [42], and may be obtained by successive differentiation of the discretized governing equations. These vectors are linearly independent and may be calculated using a single matrix factorization.

In the proposed procedure, the global structure is first discretized in some manner (Noor and Peters use finite elements), and the governing equations are obtained as a function of the n discretized degrees of freedom. Using these equations, r path derivatives are generated, where $r \ll n$. The n structural degrees of freedom are then expressed in terms of the r path derivatives using the Rayleigh-Ritz method. The reduced problem can then be solved using the Newton-Raphson technique at various points along the load-displacement curve. During the solution progress, the error of the reduced solution is monitored; this is accomplished by periodically computing the residual, R, of the full system of equations. When R exceeds a proscribed tolerance, a new set of basis vectors is generated at the current point on the load displacement curve, and progress then continues.

This method differs from the static perturbation technique (which uses the same set of basis vectors) in that the coefficients multiplying the path derivatives in this case are unknown and are computed as part of the problem solution. In the static perturbation technique, the coefficients are fixed functions of the perturbation parameter.

Several simple sample problems are solved using the proposed technique, including the large deflections of a clamped beam and a shallow circular arch. The authors estimate that saving of CPU time for these problems was on the order of five to ten, and note that the full potential of the proposed procedure could best be realized for much larger problems. The authors credit the efficiency of the proposed procedure to minimizing the number of times that the full system of equations is solved, and by minimizing the number of times the residual vector, R, is computed. They recommend computing a full set of new basis vectors each time the error tolerance is exceeded in order to maximize the distance that may be traversed along the load-displacement path before new vectors must be computed. It is proposed that solution progress along the load-displacement path be controlled using the current stiffness parameter [43], and that the frequency or error sensing (computation of R) be related to changes in this parameter.

In 1980, these techniques were used to improve the efficiency of the classical Rayleigh-Ritz technique [4]. The general procedure is the same as described above, but instead of applying it to structures that were discretized using the finite element method, it was applied to structures that were discretized using the Rayleigh-Ritz technique. The resulting procedure was dubbed the "Two-Stage Rayleigh-Ritz Technique".

The structure is first discretized using the Rayleigh-Ritz technique. This is the first stage of the procedure, and corresponds to the spatial discretization of the problem. The global shape functions used during this stage are selected by the analyst. In the second stage of the procedure, the Rayleigh-Ritz technique is used a second time to reduce the number of degrees of freedom of the discretized structure. The global shape functions used during this stage are the path derivatives of the response as described above. The solution procedure then proceeds as described above, and new sets of path derivatives are generated as necessary. Two example problems involving a spherical cap are solved.

The authors conclude that the method is both accurate and effective and that it alleviates one of the major drawbacks of the classical Rayleigh-Ritz technique, namely the repeated solution of a large system of non-sparse algebraic equations. They note that "the full potential of the proposed technique can best be realized when solving non-linear problems of structures with simple geometry but complex construction (such as stiffened plates and shells)".

In later papers, the authors extend the applications of their reduced basis method to the solution of stability problems [44], shell collapse problems [45], and the bifurcation and post-buckling analysis of laminated composite plates [46], to name a few. In all of these later applications, the method was implemented in the context of finite element analysis.

2.3 Wing Panel Design Optimization

Over the years, a number of design studies have focused on the optimal design of individual wing box structural panels such as skin panels, spar panels, and rib panels. Optimal panel designs have been obtained subject to a variety of constraints, such as strength and buckling, and under a variety of different loading conditions.

An early example of this type of work may be found in a study performed by Stroud and Agranoff [47], where hat stiffened and corrugated panels subject to longitudinal compression and shear loads were considered. Each panel was modeled as an assembly of rectangular plate elements connected along their longitudinal edges. Minimum mass designs were obtained subject to constraints on overall and local buckling, strength, stiffness, and minimum gage size. The design variables were taken to be the thicknesses and lengths of the elements that define the panel cross sections. Overall buckling modes were taken into account using the smeared stiffness approach, and local buckling modes were taken into account through a simplified analysis in which each plate element was considered individually assuming that it had simply supported boundary conditions.

A more recent study by Swanson and Gürdal [48] considered the minimum mass design of aircraft rib panels subject to axial compression, shear, and normal pressure loads. Following the method of [47], each panel was modeled as an assemblage of longitudinally connected plate elements. A variety of cross sections and stiffener arrangements were compared. Design variables were the thicknesses and lengths of cross sectional elements, and constraints included global and local buckling, strength, and geometric constraints. The design optimization and panel analysis was performed using the `PASCO` design code [2], which, unlike the analysis in [47], accounts for the continuity of local buckled mode shapes across neighboring plate elements.

While this individual panel approach has generated much useful data, ultimately the overall goal is to design a complete wing structure comprised of numerous such individual panels. It is well known that in the case of the optimization of a redundant structure made up of several components, minimization of each of the component masses does not guarantee minimization of the total mass [49]. In a redundant structure, increasing the thickness of one component will draw more load to that component, thus reducing the loads that must be resisted by the other components. Likewise, reducing the stiffness of a given component will increase the load that must be carried by neighboring components. Changing the thickness of a given component, then, not only changes the stress state in that component, but affects the load path in the structure as a whole. These effects cannot be taken into account when optimizing an isolated component.

Several researchers have focused on obtaining optimal designs for complete wing box structures. In addition to having the potential to address the shortcomings associated with individual panel design, this approach allows constraints to be imposed on the wing box global structural response as well as on the response of the individual sub-component panels. Global constraints may include aeroelastic constraints, overall buckling or vibrational constraints, and overall displacement or twist constraints. The disadvantage of the global approach is the complexity and potential expense of the resulting design problem. In order to hold the problem to a manageable size, details of individual panel design and response must often be neglected.

A study involving the optimization of complete composite wing box structures was described by Sobieszczanski-Sobieski in 1979 [49]. Here, a series of optimal designs pertaining to the low aspect ratio wing of a large transport aircraft were generated in order to compare a number of different design alternatives. Loads were generated by an aerodynamic model and the effects of aeroelasticity were included in the analysis. The design variables described the construction of each of the sandwich skin panels: the thicknesses and orientations of the plies in the composite face sheets and the total sandwich thickness. Constraints included panel buckling, strain, stress, and minimum gage constraints.

The optimization of each of the wing cover panels was performed separately and in isolation from the structure as a whole. For each panel, the corresponding membrane forces N_x, N_y, and N_{xy} were extracted from the global model and held constant while the mass of the isolated panel was optimized. After each individual panel was minimized, the global model was updated and new loads were generated. This procedure was continued until the process converged. Breaking the larger optimization problem down into a series of smaller optimization problems in this way drastically reduces the complexity and expense of the design problem, but, as noted by Sobieski, does not guarantee optimization of the structure as a whole. This is because this approach is still essentially the same as the individual panel approach described previously. During each individual optimization problem, the loads are held constant and a change in the panel stiffness is not allowed to affect the load path in the structure as a whole.

One of the first times panel buckling constraints were handled directly at the global level was in a study by Starnes and Haftka [50]. Here, the `WIDOWAC` [51] program was used to obtain minimum mass designs for a multi-spar high aspect ratio wing. An unstiffened panel buckling constraint was combined with strength, minimum gage, displacement, and twist constraints to obtain results for both isotropic and laminated composite structures. In this study, all constraints were imposed on the global wing box level, and a single optimization problem was formulated for the entire structure. The unstiffened panel buckling constraints were based on a semi-empirical buckling analysis for simply supported plates subject to in-plane forces. A global finite element model composed of rod elements for the rib and spar caps, constant strain membrane elements for the skin panels, and shear elements for the rib and spar panels was used. Design variables were the thicknesses or areas of these structural elements.

In order to demonstrate the advantages of including all the constraints at the global level, the results of this study were compared to the results obtained using the individual panel approach. One of the skin panels was removed from the global model (along with the applicable edge loads) and optimized separately. The optimal thickness for this individual panel was about 7% less than the corresponding panel that was optimized as part of the global structure. As a check, the thicker panel was replaced by the thinner panel in the global structure, and the global structure was re-analyzed. Because of significant internal load redistribution away from the thinner panel, several of the other panels violated their buckling constraints. This demonstrated the importance of including constraints on the global level, and clearly illustrated the pitfalls associated with the individual panel approach.

Although the global approach used in this work corrected a major problem with the individual panel approach and resulted in better a better global design, the complexity of the design problem was greatly increased. Instead of solving many simple optimization problems, a single complex problem was solved. Because of the size, complexity, and potential cost of this problem, details of the individual panel designs were neglected. Instead of modeling the panel cross section in detail, each panel was instead modeled as an unstiffened panel.

Schmit and Mehrinfar [52] used a global/local approach to address this problem. Here, a compromise was made between the individual panel approach and the global approach in the design of several simple wing box structures. Strength, deflection, and overall panel buckling constraints were treated at the global level using equivalent thickness design variables while panel global and local buckling constraints were imposed at the component level using detailed panel dimensions as design variables. The essential feature of this method was that instead of minimizing weight at the individual panel level, the objective was to minimize the change in the panel stiffness at this level. This procedure avoided a major drawback of the individual panel approach in that it allowed panel dimensions at the component level to change without significantly changing the load paths in the global structure. Consequently, it became possible to legitimately de-couple each of the detailed panel design problems from the global design problem, thus allowing the overall design to be obtained without neglecting details of local panel design.

The global finite element model used in [52] was composed of rod elements for the spar and rib caps, shear panels for the ribs and spars, and membrane elements for the skin panels. The global buckling constraints were based on a semi-empirical buckling analysis valid for a panel with simply supported edges and subject to in-plane loads. If sandwich panels were considered, the component level buckling constraints were based either on the same semi-empirical buckling equations used at the global level or on a more refined eigenvalue analysis in which the panel was treated as an equivalent orthotropic plate subject to in-plane loads. If hat stiffened panels were used, the buckling analysis was the same as that used in [47].

Watkins [53] extended this multilevel approach to include ply orientation design variables at the component level and a new objective function at the component level. The objective function used at the component level was a multi-criteria objective function involving the minimization of a linear combination of the panel weight and change in the panel strain energy. The inclusion of weight in the objective function was an improvement over [52] in that there was an incentive at the component level to reduce the weight of a panel which satisfies the buckling constraints.

2.4 Present Effort

In the present work, a geometrically non-linear finite strip analysis of the semi-analytical, multi-term type is developed. Displacements are approximated in the longitudinal direction using a series of trigonometric functions, which are chosen so as to make it possible to enforce compatibility between component plates where they meet at an angle. In the transverse direction, the in-plane and out-of-plane displacement components are modeled as balanced and symmetric laminated composite materials, and classical plate theory (CPT) is used.

The resulting non-linear system equations are solved using a reduced basis technique similar to that proposed by Noor. The reduced solution technique investigated here is a hybrid between the "Two Stage Rayleigh-Ritz Technique" and the reduction technique as applied to the finite element method. The present capabilities were developed with the intention of eventually incorporating them into a local panel design code.

In parallel with the development of the non-linear finite strip analysis, a new method for the global/local design optimization of wing structures is proposed and tested. Using response surface techniques, this method implements a flexible interface between the global design level (usually a finite element based computer code) and any number of local design codes. The interface is constructed so that the local optimizer does not directly modify the global design, but instead provides the global optimizer with the information (constraint values and derivatives) that are needed in order to proceed with the design optimization process. Stiffness information is transferred between the global and local design levels, thus assuring that the load paths in the global model are not affected by the results of the local optimizer.

Chapter 3

Non-linear Finite Strip Analysis

In this chapter, the theory behind the development of the geometrically non-linear analysis code `NLISA` (Non-LInear Strip Analysis) is described. Two different but related analysis methods are implemented in the code. The first method is a non-linear finite strip analysis of the semi-analytical multi-term type. Displacement fields are approximated in the longitudinal direction using trigonometric series and in the transverse direction using cubic polynomials. Individual finite strips are modeled as balanced, symmetric, orthotropic laminated composite materials, and the resulting structure is loaded in uniaxial or biaxial compression. Geometric shape imperfections may be modeled. The boundary conditions at the loaded ends are simply supported, while a variety of in-plane and out-of-plane boundary conditions may be modeled at the unloaded ends. The principle of minimum potential energy is used to obtain a set of non-linear algebraic equations, which are solved using a Newton-Raphson incremental/iterative arc length solution procedure.

The second analysis method which is implemented in the code makes use of a reduced basis method in conjunction with the foregoing finite strip analysis. Here, the (potentially large) set of non-linear algebraic equations produced by the finite strip method are replaced by a small set of system equations. In the present implementation, the basis vectors consist of successive derivatives of the non-linear solution vector with respect to a loading parameter, λ. The reduced set of system equations (typically 10 equations or less) is solved using the same

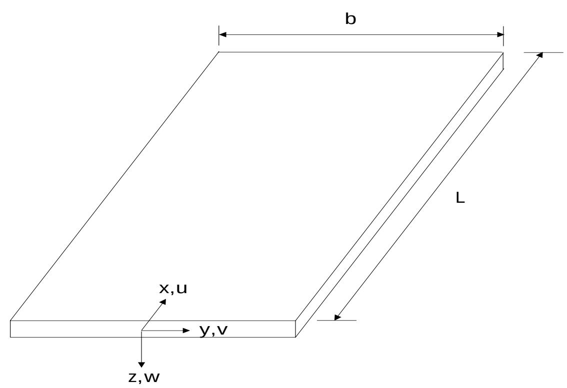

Figure 3.1: Typical finite strip

incremental/iterative arc length procedure as is used to solve the full finite strip equations.

First, the theory and assumptions underlying the basic finite strip analysis are presented. Second, the equations used to calculate the reduced basis vectors are derived and the application of the reduced basis technique to the solution of the finite strip analysis is outlined.

3.1 Geometry

The basic idea behind the finite strip method is to apply the classical Rayleigh-Ritz technique in a piecewise manner to individual sections or "strips" of the complete structure. Each finite strip typically has a length equal to that of the complete structure, but is characterized by a small but finite width. The complete structure is built up by joining several of these finite strips along their lateral edges to form the desired configuration. Practical structures that may be modeled in this manner include stiffened panels and various open and closed section prismatic columns. A single finite strip with length L and width b is presented in Figure 3.1 along with the local coordinate system.

3.2 Governing Equations for a Single Finite Strip

The governing equations for each finite strip are derived using a total potential energy approach. In the development that follows, the *material* response is assumed to be linear. Each finite strip is assumed to be in a state of plane stress, and therefore the stress components σ_z, τ_{yz}, and τ_{xz} are all assumed to be zero. Given these assumptions, the strain energy of a single finite strip may be expressed as follows:

$$U = \frac{1}{2}\int_0^L \int_{-b/2}^{b/2} \int_{-h/2}^{h/2} (\sigma_x \epsilon_x + \sigma_y \epsilon_y + \tau_{xy}\gamma_{xy})\, dx\, dy\, dz \tag{3.1}$$

where h is the total thickness of the strip.

The Kirchhoff assumptions are used to describe the nature of the displacement field through the thickness of the strip. Material lines originally perpendicular to the strip mid-surface remain straight, inextensional, and perpendicular to the mid-surface when the strip is deformed. The resulting u, v, and w displacement fields are:

$$u(x,y,z) = u^\circ(x,y) - z\frac{\partial w^\circ(x,y)}{\partial x} \tag{3.2}$$

$$v(x,y,z) = v^\circ(x,y) - z\frac{\partial w^\circ(x,y)}{\partial y} \tag{3.3}$$

$$w(x,y,z) = w^\circ(x,y) \tag{3.4}$$

where $u^\circ(x,y)$, $v^\circ(x,y)$, and $w^\circ(x,y)$ are the displacements of the middle surface of the finite strip, z=0.

Geometric non-linearities are introduced into the governing equations via the strain-displacement equations. Using the Lagrangian description, the in-plane (engineering) strains of the strip mid-surface are, in their full form, described as follows: [54]

$$\epsilon_x^0 = \frac{\partial u}{\partial x} + \frac{1}{2}\left[(\frac{\partial u}{\partial x})^2 + (\frac{\partial v}{\partial x})^2 + (\frac{\partial w}{\partial x})^2\right] \tag{3.5}$$

$$\epsilon_y^0 = \frac{\partial v}{\partial y} + \frac{1}{2}\left[(\frac{\partial u}{\partial y})^2 + (\frac{\partial v}{\partial y})^2 + (\frac{\partial w}{\partial y})^2\right] \tag{3.6}$$

$$\gamma_{xy}^0 = \frac{\partial u}{\partial y} + \frac{\partial v}{\partial x} + \frac{\partial u}{\partial x}\frac{\partial u}{\partial y} + \frac{\partial v}{\partial x}\frac{\partial v}{\partial y} + \frac{\partial w}{\partial x}\frac{\partial w}{\partial y}. \tag{3.7}$$

In the plate theory of von Karman [32], the out-of-plane displacement gradients $\partial w/\partial x$ and $\partial w/\partial y$ are assumed to be large in comparison to the in-plane $\partial u/\partial x$, $\partial u/\partial y$, $\partial v/\partial x$, and $\partial v/\partial y$ displacement gradients. As a result, only non-linear terms containing $\partial w/\partial x$ and $\partial w/\partial y$ are retained. As noted in [7] and [34], the resulting equations are not necessarily suitable for the analysis of built-up thin-walled plate structures such as those considered in the present work. For structures of this type, the in-plane displacement gradients of some plate elements may be of the same order of magnitude as the out of plane displacement gradients of other plate elements. This may be true, for example, in the case of a blade stiffened panel where the in-plane rotation of a blade stiffener may be of the same order of magnitude as the out-of-plane rotation of the skin element to which it is attached.

Following the argument put forth by Stoll [7], consider a local rotation of $\bar{\omega} = \omega\hat{k}$, where ω is the amplitude of the rotation and $\hat{k}$ is a unit vector in the z direction. The four in-plane displacement gradients corresponding to this rotation are expanded in terms of ω using a Taylor series:

$$\frac{\partial u}{\partial x} = \frac{\partial v}{\partial y} = -(1-\cos\omega) = -\frac{\omega^2}{2} + O(\omega^4) \tag{3.8}$$

$$-\frac{\partial u}{\partial y} = \frac{\partial v}{\partial x} = \sin\omega = \omega + O(\omega^3). \tag{3.9}$$

As can be seen, the displacement gradients $\partial u/\partial y$ and $\partial v/\partial x$ are of order ω, while the displacement gradients $\partial u/\partial x$ and $\partial v/\partial y$ are of order ω^2. In the present work, therefore, the in-plane displacement gradients $\partial u/\partial y$ and $\partial v/\partial x$ are considered significant and are retained in the strain expression along with the out-of-plane displacement gradients $\partial w/\partial x$ and $\partial w/\partial y$. The lower order in-plane gradients $\partial u/\partial x$ and $\partial v/\partial y$ are neglected. The strain-displacement expressions used in the present development, therefore, are:

$$\epsilon_x^0 = \frac{\partial u}{\partial x} + \frac{1}{2}\left[(\frac{\partial v}{\partial x})^2 + (\frac{\partial w}{\partial x})^2\right] \tag{3.10}$$

$$\epsilon_y^0 = \frac{\partial v}{\partial y} + \frac{1}{2}\left[(\frac{\partial u}{\partial y})^2 + (\frac{\partial w}{\partial y})^2\right] \tag{3.11}$$

$$\gamma_{xy}^0 = \frac{\partial u}{\partial y} + \frac{\partial v}{\partial x} + \frac{\partial w}{\partial x}\frac{\partial w}{\partial y}. \tag{3.12}$$

In the present implementation, there may be a w-component geometric imperfection field associated with each strip, denoted by $w^i(x, y)$. By definition, this imperfection field (and the associated strain field) does not induce stress in the strip. The "mechanical" strains (those strains which induce stress in the strip) are obtained by subtracting the strains associated with the imperfection field from the "total" strains:

$$\epsilon_x = \epsilon_x^T - \epsilon_x^i \tag{3.13}$$

$$\epsilon_y = \epsilon_y^T - \epsilon_y^i \tag{3.14}$$

$$\gamma_{xy} = \gamma_{xy}^T - \gamma_{xy}^i \tag{3.15}$$

Expressions for the "total" strains ϵ_x^T, ϵ_y^T, and γ_{xy}^T are obtained by substituting the "total" displacement field $w^T = w + w^i$ into equations 3.10 through 3.12, respectively. The strains associated with the imperfection field, ϵ_x^i, ϵ_y^i, and γ_{xy}^i are likewise obtained by substituting w^i into equations 3.10 through 3.12. The final strain-displacement relationships may then be written in the following form:

$$\epsilon_x = \epsilon_x^\circ + z\kappa_x^\circ \tag{3.16}$$

$$
\begin{aligned}
\epsilon_y &= \epsilon_y^\circ + z\kappa_y^\circ &(3.17)\\
\gamma_{xy} &= \gamma_{xy}^\circ + z\kappa_{xy}^\circ &(3.18)
\end{aligned}
$$

where

$$
\begin{aligned}
\epsilon_x^\circ &= \frac{\partial u}{\partial x} + \frac{1}{2}\left[(\frac{\partial w}{\partial x})^2 + (\frac{\partial v}{\partial x})^2\right] + \frac{\partial w}{\partial x}\frac{\partial w^i}{\partial x} &(3.19)\\
\epsilon_y^\circ &= \frac{\partial v}{\partial y} + \frac{1}{2}\left[(\frac{\partial w}{\partial y})^2 + (\frac{\partial u}{\partial y})^2\right] + \frac{\partial w}{\partial y}\frac{\partial w^i}{\partial y} &(3.20)\\
\gamma_{xy}^\circ &= \frac{\partial u}{\partial y} + \frac{\partial v}{\partial x} + \frac{\partial w}{\partial x}\frac{\partial w}{\partial y} + \frac{\partial w}{\partial x}\frac{\partial w^i}{\partial y} + \frac{\partial w}{\partial y}\frac{\partial w^i}{\partial x} &(3.21)
\end{aligned}
$$

and

$$
\begin{aligned}
\kappa_x^\circ &= -\frac{\partial^2 w}{\partial x^2} &(3.22)\\
\kappa_y^\circ &= -\frac{\partial^2 w}{\partial y^2} &(3.23)\\
\kappa_{xy}^\circ &= -2\frac{\partial^2 w}{\partial x \partial y}. &(3.24)
\end{aligned}
$$

The superscript ($\circ$) quantities are middle surface strains and curvatures.

In the present development, each finite strip is capable of representing a symmetrically laminated composite material. The stress-strain relationship for each material layer may be written as follows [55]:

$$
\left\{\begin{array}{c}\sigma_x\\ \sigma_y\\ \tau_{xy}\end{array}\right\} = \left[\begin{array}{ccc}\bar{Q}_{11} & \bar{Q}_{12} & \bar{Q}_{16}\\ \bar{Q}_{12} & \bar{Q}_{22} & \bar{Q}_{26}\\ \bar{Q}_{16} & \bar{Q}_{26} & \bar{Q}_{66}\end{array}\right] \left\{\begin{array}{c}\epsilon_x\\ \epsilon_y\\ \gamma_{xy}\end{array}\right\}. \tag{3.25}
$$

Substituting these expressions for the stresses and the expressions for the strains (3.16)-(3.18) into the energy expression (3.1) and integrating through the total thickness of the finite strip, the following expression is obtained for the strain energy of a finite strip:

$$U = \frac{1}{2}\int_0^L \int_{-b/2}^{b/2} (N_x\epsilon_x^\circ + N_y\epsilon_y^\circ + N_{xy}\gamma_{xy}^\circ + M_x\kappa_x^\circ + M_y\kappa_y^\circ + M_{xy}\kappa_{xy}^\circ)\,dx\,dy \tag{3.26}$$

where the stress and moment resultants have their usual definitions:

$$N_x = \int_{-h/2}^{h/2} \sigma_x\,dz \tag{3.27}$$

$$N_y = \int_{-h/2}^{h/2} \sigma_y\,dz \tag{3.28}$$

$$N_{xy} = \int_{-h/2}^{h/2} \tau_{xy}\,dz \tag{3.29}$$

$$M_x = \int_{-h/2}^{h/2} z\sigma_x\,dz \tag{3.30}$$

$$M_y = \int_{-h/2}^{h/2} z\sigma_y\,dz \tag{3.31}$$

$$M_{xy} = \int_{-h/2}^{h/2} z\tau_{xy}\,dz. \tag{3.32}$$

Using these expressions along with (3.25), the constitutive relationships in terms of the stress and moment resultants may be written in the following familiar form,

$$\left\{\begin{array}{c} N_x \\ N_y \\ N_{xy} \end{array}\right\} = \left[\begin{array}{ccc} A_{11} & A_{12} & A_{16} \\ A_{12} & A_{22} & A_{26} \\ A_{16} & A_{26} & A_{66} \end{array}\right] \left\{\begin{array}{c} \epsilon_x^\circ \\ \epsilon_y^\circ \\ \gamma_{xy}^\circ \end{array}\right\} \tag{3.33}$$

$$\left\{\begin{array}{c} M_x \\ M_y \\ M_{xy} \end{array}\right\} = \left[\begin{array}{ccc} D_{11} & D_{12} & D_{16} \\ D_{12} & D_{22} & D_{26} \\ D_{16} & D_{26} & D_{66} \end{array}\right] \left\{\begin{array}{c} \kappa_x^\circ \\ \kappa_y^\circ \\ \kappa_{xy}^\circ \end{array}\right\} \tag{3.34}$$

where the laminate stiffness coefficients A_{ij} and D_{ij} are defined as follows:

$$\begin{array}{ll} A_{ij} & = \int_{-h/2}^{h/2} \bar{Q}_{ij}\,dz \\ D_{ij} & = \int_{-h/2}^{h/2} \bar{Q}_{ij} z^2\,dz \end{array} \quad i,j = 1,2,6. \tag{3.35}$$

Because the stacking sequence of each finite strip is symmetric about the mid-plane, there is no material coupling between the in-plane and out-of-plane response quantities. In addition, the effects of the stretching-shearing terms A_{16} and A_{26}, as well as the bending-twisting terms D_{16} and D_{26} are neglected in the present work. The laminates are therefore assumed to behave orthotropically in bending. The former terms are identically zero if the laminate is balanced [55], and the effect of the latter terms may be minimized for moderately thick laminates.

If the strain energy (3.26) is written in terms of the displacements, the following expression is obtained:

$$
\begin{aligned}
U \;=\; & \frac{1}{2}\int_0^L \int_{-b/2}^{b/2} \Big\{ A_{11}(\frac{\partial u}{\partial x})^2 + 2A_{11}\frac{\partial u}{\partial x}\frac{\partial w}{\partial x}\frac{\partial w^i}{\partial x} + A_{11}(\frac{\partial w}{\partial x})^2(\frac{\partial w^i}{\partial x})^2 + 2A_{12}\frac{\partial u}{\partial x}\frac{\partial v}{\partial y} + \\
& 2A_{12}\frac{\partial v}{\partial y}\frac{\partial w}{\partial x}\frac{\partial w^i}{\partial x} + 2A_{12}\frac{\partial u}{\partial x}\frac{\partial w}{\partial y}\frac{\partial w^i}{\partial y} + 2A_{12}\frac{\partial w}{\partial x}\frac{\partial w}{\partial y}\frac{\partial w^i}{\partial x}\frac{\partial w^i}{\partial y} + A_{22}(\frac{\partial v}{\partial y})^2 + \\
& 2A_{22}\frac{\partial v}{\partial y}\frac{\partial w}{\partial y}\frac{\partial w^i}{\partial y} + A_{22}(\frac{\partial w}{\partial y})^2(\frac{\partial w^i}{\partial y})^2 + A_{66}\left[(\frac{\partial u}{\partial y})^2 + 2\frac{\partial u}{\partial y}\frac{\partial v}{\partial x} + (\frac{\partial v}{\partial x})^2\right] + \\
& 2A_{66}(\frac{\partial u}{\partial y} + \frac{\partial v}{\partial x})(\frac{\partial w}{\partial x}\frac{\partial w^i}{\partial y} + \frac{\partial w}{\partial y}\frac{\partial w^i}{\partial x}) + A_{66}(\frac{\partial w}{\partial x})^2(\frac{\partial w^i}{\partial y})^2 + A_{66}(\frac{\partial w}{\partial y})^2(\frac{\partial w^i}{\partial x})^2 + \\
& 2A_{66}\frac{\partial w}{\partial x}\frac{\partial w}{\partial y}\frac{\partial w^i}{\partial x}\frac{\partial w^i}{\partial y} + D_{11}(\frac{\partial^2 w}{\partial x^2})^2 + 2D_{12}\frac{\partial^2 w}{\partial x^2}\frac{\partial^2 w}{\partial y^2} + 4D_{66}(\frac{\partial^2 w}{\partial x \partial y})^2 + \\
& A_{11}(\frac{\partial u}{\partial x} + \frac{\partial w^i}{\partial x}\frac{\partial w}{\partial x})\left[(\frac{\partial v}{\partial x})^2 + (\frac{\partial w}{\partial x})^2\right] + A_{12}(\frac{\partial u}{\partial x} + \frac{\partial w^i}{\partial x}\frac{\partial w}{\partial x})\left[(\frac{\partial u}{\partial y})^2 + (\frac{\partial w}{\partial y})^2\right] + \\
& A_{12}(\frac{\partial v}{\partial y} + \frac{\partial w^i}{\partial y}\frac{\partial w}{\partial y})\left[(\frac{\partial v}{\partial x})^2 + (\frac{\partial w}{\partial x})^2\right] + A_{22}(\frac{\partial v}{\partial y} + \frac{\partial w^i}{\partial y}\frac{\partial w}{\partial y})\left[(\frac{\partial u}{\partial y})^2 + (\frac{\partial w}{\partial y})^2\right] + \\
& 2A_{66}(\frac{\partial u}{\partial y} + \frac{\partial v}{\partial x})\frac{\partial w}{\partial x}\frac{\partial w}{\partial y} + 2A_{66}(\frac{\partial w}{\partial x})^2\frac{\partial w}{\partial y}\frac{\partial w^i}{\partial y} + 2A_{66}(\frac{\partial w}{\partial y})^2\frac{\partial w}{\partial x}\frac{\partial w^i}{\partial x} + A_{66}(\frac{\partial w}{\partial x})^2(\frac{\partial w}{\partial y})^2 + \\
& \frac{1}{4}A_{11}\left[(\frac{\partial v}{\partial x})^4 + 2(\frac{\partial v}{\partial x})^2(\frac{\partial w}{\partial x})^2 + (\frac{\partial w}{\partial x})^4\right] + \frac{1}{4}A_{22}\left[(\frac{\partial v}{\partial y})^4 + 2(\frac{\partial u}{\partial y})^2(\frac{\partial w}{\partial y})^2 + (\frac{\partial w}{\partial y})^4\right] + \\
& \frac{1}{2}A_{12}\left[(\frac{\partial v}{\partial x})^2(\frac{\partial u}{\partial y})^2 + (\frac{\partial v}{\partial x})^2(\frac{\partial w}{\partial y})^2 + (\frac{\partial u}{\partial y})^2(\frac{\partial w}{\partial x})^2 + (\frac{\partial w}{\partial x})^2(\frac{\partial w}{\partial y})^2\right]\Big\}\, dx\, dy.
\end{aligned}
\tag{3.36}
$$

As noted in [3], this expression can be broken into three distinct groupings of terms, one of which is quadratic in the displacements, one of which is cubic in the displacements, and the last of which is quartic in the displacements.

The potential energy of the external loads may be written

$$V = -\int_{-b/2}^{b/2} \hat{N}_x u^\circ \Big|_0^L dy - \int_0^L \hat{N}_y v^\circ \Big|_{-b/2}^{b/2} dx - \int_0^L \int_{-b/2}^{b/2} q w^\circ \, dx \, dy \tag{3.37}$$

where $\hat{N}_x$ and $\hat{N}_y$ are known loads applied at the mid-plane of the finite strip and q is a load acting perpendicular to the plane of the strip.

The total potential energy of the finite strip, Π, is obtained by adding the strain energy (3.26) to the potential energy of the applied loads (3.37):

$$\Pi = U + V. \tag{3.38}$$

The equilibrium equations are obtained by taking the first variation of Π and setting the resulting expression to zero. After taking the first variation of Π and integrating by parts twice, the following expression is obtained:

$$\begin{aligned}
&\int_0^L \int_{-b/2}^{b/2} \Big\{ \Big[\frac{\partial N_x}{\partial x} + \frac{\partial N_{xy}}{\partial y} + \frac{\partial}{\partial y}(N_y \frac{\partial u}{\partial y}) \Big] \, \delta u + \Big[\frac{\partial N_{xy}}{\partial x} + \frac{\partial N_y}{\partial y} + \frac{\partial}{\partial x}(N_x \frac{\partial v}{\partial x}) \Big] \, \delta v + \\
&\Big[\frac{\partial^2 M_x}{\partial x^2} + 2\frac{\partial^2 M_{xy}}{\partial x \partial y} + \frac{\partial^2 M_y}{\partial y^2} + \frac{\partial}{\partial x}(N_x \frac{\partial w}{\partial x} + N_{xy} \frac{\partial w}{\partial y}) + \frac{\partial}{\partial y}(N_{xy} \frac{\partial w}{\partial x} + N_y \frac{\partial w}{\partial y}) + \\
&q \Big] \, \delta w \Big\} \, dx \, dy + \int_{-b/2}^{b/2} (N_x - \hat{N}_x) \, dy \, \delta u + \int_0^L (N_{xy} + N_y \frac{\partial u}{\partial y}) \, dx \, \delta u + \\
&\int_{-b/2}^{b/2} (N_x \frac{\partial v}{\partial x} + N_{xy}) \, dy \, \delta v + \int_{-b/2}^{b/2} (\frac{\partial M_x}{\partial x} + \frac{\partial M_{xy}}{\partial y} + N_x \frac{\partial w}{\partial x} + N_{xy} \frac{\partial w}{\partial y}) \, dy \, \delta w + \\
&\int_0^L (N_y - \hat{N}_y) \, dx \, \delta v + \int_0^L (\frac{\partial M_x}{\partial y} + \frac{\partial M_y}{\partial y} + N_{xy} \frac{\partial w}{\partial x} + N_y \frac{\partial w}{\partial y}) \, dx \, \delta w - \\
&\int_{-b/2}^{b/2} M_x \, dy \, \delta(\frac{\partial w}{\partial x}) - \int_0^L M_{xy} \, dx \, \delta(\frac{\partial w}{\partial x}) - \int_{-b/2}^{b/2} M_{xy} \, dy \, \delta(\frac{\partial w}{\partial y}) - \int_0^L M_y \, dx \, \delta(\frac{\partial w}{\partial y}) = 0
\end{aligned} \tag{3.39}$$

Because δu, δv, and δw may each vary independently of one another and independently of their values at the boundary of the domain, the equilibrium equations for the finite strip are the Euler equations in this expression. The three equilibrium equations are:

$$\frac{\partial N_x}{\partial x} + \frac{\partial N_{xy}}{\partial y} + \frac{\partial}{\partial y}(N_y \frac{\partial u}{\partial y}) = 0 \tag{3.40}$$

$$\frac{\partial N_{xy}}{\partial x} + \frac{\partial N_y}{\partial y} + \frac{\partial}{\partial x}(N_x \frac{\partial v}{\partial x}) = 0 \tag{3.41}$$

$$\begin{aligned} &\frac{\partial^2 M_x}{\partial x^2} + 2\frac{\partial^2 M_{xy}}{\partial x \partial y} + \frac{\partial^2 M_y}{\partial y^2} + \\ &\frac{\partial}{\partial x}(N_x \frac{\partial w}{\partial x} + N_{xy} \frac{\partial w}{\partial y}) + \frac{\partial}{\partial y}(N_{xy} \frac{\partial w}{\partial x} + N_y \frac{\partial w}{\partial y}) + q = 0 \end{aligned} \tag{3.42}$$

The allowed boundary conditions are obtained by requiring that each of the boundary integrals in (3.39) be zero. The boundary conditions are:

At $x = 0, L$:

- u specified **or** $N_x = \hat{N}_x$
- v specified **or** $N_x \partial v/\partial x + N_{xy} = 0$
- w specified **or** $\partial M_x/\partial x + 2\partial M_{xy}/\partial y + N_x \partial w/\partial x + N_{xy} \partial w/\partial y = 0$
- $\partial w/\partial x$ specified **or** $M_x = 0$

At $y = \pm b/2$:

- v specified **or** $N_y = \hat{N}_y$
- u specified **or** $N_{xy} + N_y \partial u/\partial y = 0$
- w specified **or** $2\partial M_{xy}/\partial x + \partial M_y/\partial y + N_{xy} \partial w/\partial x + N_y \partial w/\partial y = 0$
- $\partial w/\partial y$ specified **or** $M_y = 0$

At each corner:

- w specified **or** $M_{xy} = 0$

3.3 Application of Rayleigh-Ritz Technique

The finite strip equations are discretized using the Rayleigh-Ritz method.

3.3.1 Assumed Displacement Field

In order to apply the Rayleigh-Ritz method to the solution of the governing equations, it is necessary to assume a functional form for each of the $u^\circ(x,y)$, $v^\circ(x,y)$, and $w^\circ(x,y)$ displacement fields. In the present work, each displacement field is approximated by a trigonometric series in the longitudinal (x) direction, and by a polynomial of order P in the transverse (y) direction. The following general forms were assumed:

$$u^\circ(x,y) = \lambda\hat{\epsilon}_{xl}(x - \frac{L}{2}) + \sum_{k=1}^{Kmax} U_k^P(y)\sin(\frac{k\pi x}{L}) \tag{3.43}$$

$$v^\circ(x,y) = \lambda\hat{\epsilon}_{yl}y + \sum_{m=1}^{Mmax} V_m^P(y)\sin(\frac{m\pi x}{L}) \tag{3.44}$$

$$w^\circ(x,y) = \sum_{n=1}^{Nmax} W_n^P(y)\sin(\frac{n\pi x}{L}) \tag{3.45}$$

where $U_k^P(y)$, $V_m^P(y)$, and $W_n^P(y)$ are each polynomials of order P. The terms $\hat{\epsilon}_{xl}$ and $\hat{\epsilon}_{yl}$ are the strains obtained from a linear pre-buckling analysis of the structure (see section 3.4) and λ is a loading parameter that is used to progressively increase $\hat{\epsilon}_{xl}$ and $\hat{\epsilon}_{yl}$ during the course of the non-linear analysis.

The choice of the $\sin(n\pi x/L)$ series for approximating the w displacement field in the longitudinal direction implies that the displacement w and the curvature $\partial^2 w/\partial x^2$ are both zero at intervals of $\pm nL$ ($n = 0, 1, 2, \ldots Nmax$). The resulting finite strip may be used to model a plate with longitudinal ends ($x = 0$ and $x = L$) simply supported out of plane or alternatively, a portion of a larger structure that buckles with nodal lines at $\pm nL$. Likewise, the choice of the $\sin(k\pi x/L)$ series to approximate the u displacement field and the $\sin(m\pi x/L)$ series to approximate the v displacement field implies that there is no u or v displacement contribution from the non-linear analysis at $x = \pm kL$ ($k = 0, 1, 2, \ldots Kmax$) and $x = \pm mL$ ($m = 0, 1, 2, \ldots Mmax$), respectively.

It is, of course, possible to select different functions to approximate the displacement fields in the longitudinal direction of the finite strip. In much of the non-linear finite strip literature, for example, cos functions are used to approximate the v displacement field. The cos series enables the finite strip to accurately model a plate which has unrestrained lateral edges along its entire length. This is a common boundary condition, and numerous results are may be found in the literature corresponding to this case.

The disadvantage of using a cos series to model the v displacement field becomes apparent when the finite strips are used to model a more complex structure such as a stiffened panel. In these cases, some of the finite strips will attach at non-zero angles to one another. In order to assure the compatibility of displacements at the plate junctions, the v displacement function (of the blade stiffener, for example) must be compatible with the w displacement function (of the panel skin, for example). If the v displacement field is modeled with a cos series and the w displacement field is modeled with a sin series, it will not be possible to enforce this compatibility. In order to circumvent this difficulty, the "classical assumptions" of post-local buckling analysis are often enforced in order to de-couple the v and w displacements of the attached strips (see Chapter 2). Using the classical assumptions, it is possible to perform a limited post-local buckling analysis.

In order to obtain a more complete picture of the structure's behavior, however, it is necessary to abandon the classical assumptions and enforce compatibility between the v and w displacement fields at plate junctions. When compatibility is enforced, the structure may be modeled without prior knowledge of the buckling mode shapes. Furthermore, because the analysis is more general, it is capable of proceeding further into the post-buckling regime. As discussed in [31], enforcing compatibility between attached plate strips is sometimes necessary if the correct response is to be obtained. In [31], the collapse of a rectangular box column was investigated; it was necessary to enforce compatibility and at the strip junctions in order to accurately account for the effects of corner displacements and to accurately predict the column's collapse.

In the present work, then, displacement fields were modeled so as to allow compatibility to be enforced between the v and w displacements at plate junctions. Consequently, the resulting finite strip analysis is both more accurate and more computationally expensive [31] than it would have been had the classical assumptions been employed.

A third-order Lagrangian polynomial is used to approximate the two in-plane displacement fields in the y-direction:

$$U_k^3 = N_1(y)u_{1k} + N_2(y)u_{2k} + N_3(y)u_{3k} + N_4(y)u_{4k} \tag{3.46}$$

$$V_m^3 = N_1(y)v_{1m} + N_2(y)v_{2m} + N_3(y)v_{3m} + N_4(y)v_{4m} \tag{3.47}$$

where

$$N_1(y) = \left(-\frac{1}{16} + \frac{y}{8b} + \frac{9y^2}{4b^2} - \frac{9y^3}{2b^3}\right) \tag{3.48}$$

$$N_2(y) = \left(\frac{9}{16} - \frac{27y}{8b} - \frac{9y^2}{4b^2} + \frac{27y^3}{2b^3}\right) \tag{3.49}$$

$$N_3(y) = \left(\frac{9}{16} + \frac{27y}{8b} - \frac{9y^2}{4b^2} - \frac{27y^3}{2b^3}\right) \tag{3.50}$$

$$N_4(y) = \left(-\frac{1}{16} - \frac{y}{8b} + \frac{9y^2}{4b^2} + \frac{9y^3}{2b^3}\right) \tag{3.51}$$

In equations (3.46) and (3.47), u_{1k} and v_{1m} are the values of the u and v displacement fields at y=-b/2, u_{2k} and v_{2m} are the values of the displacement fields at y=-b/6, u_{3k} and v_{3m} are the values of the displacement fields at y=+b/6, u_{4k} and v_{4m} and are the values of the displacement fields at y=+b/2. Although a number of researchers have used a linear function to model the transverse in-plane displacement fields, references [3] and [34] suggest that the use of higher order functions results in a lower overall computational time for a given level of accuracy as well as a better representation of the structural response in the post-buckling regime. For this reason, higher order functions are used in the present work.

A third order Hermitian polynomial is used to approximate the w displacement field in the z-direction:

$$W_n^3 = M_1(y)w_{1n} + M_2(y)\psi_{1n} + M_3(y)w_{4n} + M_4(y)\psi_{4n} \tag{3.52}$$

where

$$M_1(y) = (\frac{1}{2} - \frac{3y}{2b} + \frac{2y^3}{b^3}) \tag{3.53}$$

$$M_2(y) = (\frac{b}{8} - \frac{y}{4} - \frac{y^2}{2b} + \frac{y^3}{b^2}) \tag{3.54}$$

$$M_3(y) = (\frac{1}{2} + \frac{3y}{2b} - \frac{2y^3}{b^3}) \tag{3.55}$$

$$M_4(y) = (-\frac{b}{8} - \frac{y}{4} + \frac{y^2}{2b} + \frac{y^3}{b^2}) \tag{3.56}$$

In equation (3.52), w_{1n} is the w displacement at y=-b/2 and ψ_{1n} is the slope $\partial w/\partial y$ at y=-b/2. Likewise, w_{4n} is the w displacement at y=+b/2 and ψ_{4n} is the slope $\partial w/\partial y$ at y=+b/2.

If the expressions for $U_k^3(y)$, $V_m^3(y)$, and $W_n^3(y)$ are substituted into equations 3.43 through 3.45, the following final expressions for the u°, v°, and w° displacement fields are obtained:

$$u^\circ(x,y) = \lambda\hat{\epsilon}_{xl}(x - \frac{L}{2}) + \sum_{k=1}^{Kmax}\sum_{p=1}^{4} N_p(y)u_{pl}\sin(\frac{k\pi x}{L}) \tag{3.57}$$

$$v^\circ(x,y) = \lambda\hat{\epsilon}_{yl}y + \sum_{m=1}^{Mmax}\sum_{p=1}^{4} N_p(y)v_{pm}\sin(\frac{m\pi x}{L}) \tag{3.58}$$

$$w^\circ(x,y) = \sum_{n=1}^{Nmax}\sum_{p=1}^{4} M_p(y)w_{pn}\sin(\frac{n\pi x}{L}) \tag{3.59}$$

In these expressions, there are $4 \cdot Kmax$ unknowns in the u-equation, $4 \cdot Mmax$ unknowns in the v-equation, and $4 \cdot Nmax$ unknowns in the w-equation. The u, v, and w unknowns may be written in terms of the vector, x_j:

$$x_j = \left\{ \begin{array}{c} u_p \\ v_q \\ w_r \end{array} \right\} \tag{3.60}$$

where ($p = 1, 4 \cdot Kmax$, $q = 1, 4 \cdot Mmax$, and $r = 1, 4 \cdot Nmax$).

3.3.2 Discretized Governing Equations

The assumed displacement fields are now substituted into the expression for the total potential energy, Π. In the present implementation, we are concerned only with the structure's response to an applied end shortening, and there are no external loading terms. As a result, the total potential energy in terms of the displacements is given by equation (3.36). If the final expressions for the displacement fields are substituted into equation (3.36) and the necessary integrations are performed, the expression for the total potential energy of a single finite strip may be written as follows:

$$\Pi = \lambda \bar{A}_i^{\circ} x_i + (\bar{A}_{ij} + \lambda \bar{A}_{ij}^*) x_i x_j + \frac{1}{6} \bar{A}_{ijk}^1 x_i x_j x_k + \frac{1}{12} \bar{A}_{ijkl}^2 x_i x_j x_k x_l, \tag{3.61}$$

where, for a finite strip of given dimensions, $\bar{A}_i^{\circ}$, $\bar{A}_{ij}$, $\bar{A}_{ij}^*$, $\bar{A}_{ijk}^1$, and $\bar{A}_{ijkl}^2$ contain constant terms. The equivalent expression may be written in terms of the system matrices as follows:

$$\Pi = \lambda x_i^T \bar{q}_i + x_i^T (\bar{K}_{ij} + \lambda \bar{K}_{ij}^*) x_j + \frac{1}{6} x_i^T \bar{K}_{ij}^1 x_j + \frac{1}{12} x_i^T \bar{K}_{ij}^2 x_j. \tag{3.62}$$

In this expression, $\bar{K}_{ij}$, $\bar{K}_{ij}^*$, $\bar{K}_{ij}^1$, and $\bar{K}_{ij}^2$ are all symmetric matrices. $\bar{K}_{ij}$ and $\bar{K}_{ij}^*$ are matrices of constants (for a given finite strip), while $\bar{K}_{ij}^1$ is a linear function of the unknown coefficients and $\bar{K}_{ij}^2$ is quadratic in the unknown coefficients:

$$\bar{K}^1_{ij} = \bar{A}^1_{ijk} x_k \tag{3.63}$$

$$\bar{K}^2_{ij} = \bar{A}^2_{ijkl} x_k x_l. \tag{3.64}$$

The vector $\bar{q}_i$ is a vector of constants for a given strip. In evaluating the system matrices, the x-direction integrations are carried out analytically, while the y-direction integrations are evaluated numerically (and exactly) using Gaussian quadrature. As an example, the derivation of an entry in the $\bar{K}^2_{ij}$ matrix is performed in Appendix A.

In order to analyze a structure that is made up of several finite strips, it is necessary to obtain an expression for the total potential energy of the complete structure. This is accomplished by summing the potential energies for each individual finite strip. Using the assembly techniques commonly used in matrix structural analysis [56], the expression for the total strain energy of the structure may be obtained:

$$\Pi = \lambda x_i^T q_i + x_i^T (K_{ij} + \lambda K^*_{ij}) x_j + \frac{1}{6} x_i^T K^1_{ij} x_j + \frac{1}{12} x_i^T K^2_{ij} x_j. \tag{3.65}$$

This expression has the same form as equation (3.62), except that each of the matrices and vectors now correspond to the entire structure. During this assembly process, compatibility of all three displacement components and the rotation $\partial w/\partial y$ is maintained at plate junctions. Degrees of freedom corresponding to zero-displacement boundary conditions are eliminated using standard techniques of matrix structural analysis [56].

Equilibrium equations are now obtained by differentiating the potential energy function with respect to each degree of freedom and equating the resulting expressions to zero. The resulting system equations may be arranged to have the following form:

$$\lambda q_i + (K_{ij} + \lambda K^*_{ij} + \frac{1}{2} K^1_{ij} + \frac{1}{3} K^2_{ij}) x_j = 0. \tag{3.66}$$

3.3.3 Permissible Boundary Conditions

In the application of the Rayleigh-Ritz technique, the assumed displacement functions must satisfy the kinematic boundary conditions of the problem. Consequently, the boundary conditions that may be modeled at the longitudinal ends of the structure are restricted by the functions used to approximate the displacement fields in the x-direction. In the present work, each of the u, v, and w displacement fields are represented by a sin series in this direction (repeated from equations (3.57) through (3.59)):

$$u^{\circ}(x,y) = \lambda\hat{\epsilon}_{xl}(x-\frac{L}{2}) + \sum_{k=1}^{Kmax}\sum_{p=1}^{4} N_p(y)u_{pl}\sin(\frac{k\pi x}{L}) \tag{3.67}$$

$$v^{\circ}(x,y) = \lambda\hat{\epsilon}_{yl}y + \sum_{m=1}^{Mmax}\sum_{p=1}^{4} N_p(y)v_{pm}\sin(\frac{m\pi x}{L}) \tag{3.68}$$

$$w^{\circ}(x,y) = \sum_{n=1}^{Nmax}\sum_{p=1}^{4} M_p(y)w_{pn}\sin(\frac{n\pi x}{L}). \tag{3.69}$$

In the case of the w displacement field, this means that the displacement w and the curvature $\partial^2 w/\partial x^2$ are both zero at the longitudinal ends of each strip ($x = 0$ and $x = L$). This corresponds to a specially orthotropic strip that is simply supported out of plane at its longitudinal ends. The u displacement at the longitudinal ends is $\pm\lambda\hat{\epsilon}_{xl}L/2$, which corresponds to uniform end shortening. The v displacement at the longitudinal ends is restricted to $\lambda\hat{\epsilon}_{yl}y$ (uniform expansion/contraction).

In the lateral (y) direction, the displacement fields are modeled using third order polynomials. In general, any desired kinematic boundary condition may be satisfied at the external edges of the structure by specifying the appropriate degrees of freedom in the usual manner. In the present implementation of the finite strip analysis, the following options are provided:

At $y = \pm b/2$:

- v specified **or** $N_y = 0$

- u specified **or** $N_{xy} + N_y \partial u/\partial y = 0$
- w specified **or** $2\partial M_{xy}/\partial x + \partial M_y/\partial y + N_{xy}\partial w/\partial x + N_y \partial w/\partial y = 0$
- $\partial w/\partial y$ specified **or** $M_y = 0$

As is the case in any Rayleigh-Ritz analysis, the kinematic boundary conditions are satisfied exactly, but, in general, the natural boundary conditions are satisfied only approximately.

3.4 Linear (Pre-buckling) Solution

Before the non-linear solution procedure is initiated, a linear pre-buckling analysis of the structure must be performed. The pre-buckling analysis implemented in the present work is essentially the same as that performed by `PASCO` [2]. For the purposes of the linear analysis, it is assumed that only in-plane normal strains and stresses are induced in the structure. As a consequence, there is no deformation out-of-plane and shape imperfections are ignored. All displacements, strains and stresses are proportional to a loading parameter, λ.

The pre-bucking analysis may be initiated by using one of three different options:

1. specify $\hat{N}_x$ and $\hat{N}_y$
2. specify $\hat{N}_x$ and $\hat{\epsilon}_{yL} = 0$
3. specify $\hat{\epsilon}_{xL}$ and $\hat{\epsilon}_{yL}$.

In these options, $\hat{N}_x$ is the mean global axial stress resultant, and is defined as:

$$\hat{N}_x = \frac{1}{B}\sum_{p=1}^{P} N_x^p b^p \tag{3.70}$$

where B is the width of the total structure, P is the number of finite strips in the structure, N_x^p is the axial stress resultant of strip p, and b^p is the width of strip p.

$\hat{N}_y$ is the mean global transverse stress resultant, and is the same for each finite strip comprising the structure's "skin". If the structure does not possess a continuous planar skin, $\hat{N}_y$ should be specified to be zero. Finite strips which are not part of the planar skin (a stiffener, for example) do not carry the $\hat{N}_y$ load. In the present implementation, each finite strip in the global structure has a flag, k_p, which must be set to "1" if the strip is part of the planar skin, and "0" if it is not. For each strip, therefore, the local transverse stress resultant, N_y^p, is defined using the following simple equation:

$$N_y^p = k_p \hat{N}_y. \tag{3.71}$$

$\hat{\epsilon_{xL}}$ is the global axial strain (uniform throughout the structure), and $\hat{\epsilon}_{yL}$ is the mean global transverse strain in the panel skin, defined as

$$\hat{\epsilon}_{yL} = \frac{\Delta v_L}{B}. \tag{3.72}$$

In this equation, Δv_L is the total change in width of the structure, and may be defined as a function of the local transverse strains, $\hat{\epsilon}_{yL}^p$:

$$\Delta v_L = \sum_{p=1}^{P} k_p b_p \hat{\epsilon}_{yL}^p. \tag{3.73}$$

In the following sections, the sequence of equations used for each option are described.

3.4.1 Option (1): specify $\hat{N}_x$ and $\hat{N}_y$

In each strip, the local strain components may be related to the local stress resultants through the constitutive equations (equation 3.33):

$$N_x^p = A_{11}^p \hat{\epsilon_{xL}} + A_{12}^p \hat{\epsilon_{yL}}^p \tag{3.74}$$

$$N_y^p = A_{12}^p \hat{\epsilon_{xL}} + A_{22}^p \hat{\epsilon_{yL}}^p. \quad (3.75)$$

If we substitute the expression for the local transverse stress resultant (3.71) into the second of these equations and solve for $\epsilon_{yL}^{\hat{p}}$, we have:

$$\epsilon_{yL}^{\hat{p}} = \frac{\hat{N}_y k_p - \hat{\epsilon_{xL}} A_{12}^p}{A_{22}^p}. \quad (3.76)$$

We may then obtain an expression for the global transverse strain component, $\hat{\epsilon}_{yL}$, by substituting this equation into the expression for Δv_L (3.73) and making use of equation 3.72:

$$\hat{\epsilon}_{yL} = \frac{1}{B}(\hat{N}_y S_3 - \hat{\epsilon}_{xL} S_4), \quad (3.77)$$

where

$$S_3 = \sum_{p=1}^{P} k_p b_p (\frac{1}{A_{22}^p})_p \quad (3.78)$$

$$S_4 = \sum_{p=1}^{P} k_p b_p (\frac{A_{12}}{A_{22}})_p. \quad (3.79)$$

Finally, we may obtain an expression for $\hat{\epsilon_{xL}}$ by substituting the expression for $\epsilon_{yL}^{\hat{p}}$ (3.76) and the expression for $\hat{N}_x$ (3.70) into the first constitutive equation (3.74). We obtain:

$$\hat{\epsilon_{xL}} = \frac{\hat{N}_x B - \hat{N}_y S_2}{S_1}, \quad (3.80)$$

where

$$S_1 = \sum_{p=1}^{P} b_p (A_{11} - \frac{A_{12}^2}{A_{22}})_p \quad (3.81)$$

$$S_2 = \sum_{p=1}^{P} b_p k_p (\frac{A_{12}}{A_{22}})_p. \quad (3.82)$$

If $\hat{N}_x$ and $\hat{N}_y$ are specified, therefore, equation 3.80 is first used to solve for $\hat{\epsilon_{xL}}$. Once this quantity is known, equation 3.77 may be used to solve for $\hat{\epsilon}_{yL}$.

3.4.2 Option (2): specify $\hat{N}_x$ and $\hat{\epsilon}_{yL} = 0$

If we substitute the expression for the axial strain component $\hat{\epsilon_{xL}}$ (3.80) into the expression for the global transverse strain component $\hat{\epsilon}_{yL}$ (3.77), we may obtain an expression for the mean global transverse stress resultant, $\hat{N}_y$, in terms of $\hat{\epsilon}_{yL}$ and $\hat{N}_x$:

$$\hat{N}_y = (\hat{\epsilon}_{yL} + \hat{N}_x \frac{S_4}{S_1})(\frac{BS_1}{S_1 S_3 + S_2 S_4}). \tag{3.83}$$

Once we utilize this expression to solve for $\hat{N}_y$, we may use equation 3.80 to solve for $\hat{\epsilon}_{xL}$.

3.4.3 Option (3): specify $\hat{\epsilon}_{xL}$ and $\hat{\epsilon}_{yL}$

We may rearrange the expression for the axial strain resultant, $\hat{\epsilon}_{xL}$ (3.80) as follows:

$$\hat{N}_y = \frac{\hat{N}_x B - \hat{\epsilon}_{xL} S_1}{S_2}. \tag{3.84}$$

Equating this expression for $\hat{N}_y$ with that given by equation 3.83, we may obtain the following expression for $\hat{N}_x$:

$$\hat{N}_x = \hat{\epsilon}_{xL}(\frac{S_1 S_3 + S_2 S_4}{BS_3}) + \hat{\epsilon}_{yL} \frac{S_2}{S_3}. \tag{3.85}$$

This equation may be used to solve for $\hat{N}_x$, and equation 3.84 may be used to solve for $\hat{N}_y$.

3.5 Non-linear Solution

For a specific problem, the discretized non-linear equations (3.66) are solved using an incremental/iterative solution scheme modeled on the procedure `NL_STATIC_1` used in [57]. In the implemented method, progress along the load-displacement "path" is achieved in a series of *increments*, or *steps* using a Riks/Crisfield arc-length approach [58]. At a given step, Newton-Raphson *iterations* are used to achieve a converged solution. The present algorithm is capable of traversing limit points in the load-displacement path, but is not capable of finding and following the correct path at pure bifurcation points.

It is necessary to utilize an incremental/iterative solution technique to solve the present class of problems because the Newton-Raphson algorithm will converge only if the "initial guess" is sufficiently near the actual solution. If no steps/increments are used and a solution is sought directly at the final load/displacement increment, the algorithm will likely not converge. If it does converge in such a case, there is no guarantee that will converge on the desired equilibrium path.

The system of equations that is solved at each step consists of the equilibrium equations (3.66) and a single "arc-length" equation, which governs the distance along the load-displacement "path" (the increment) that is traversed during the step. The equilibrium equations are expressed in terms of a residual vector, r_i, which is zero when equilibrium is satisfied:

$$r_i = \lambda q_i + (K_{ij} + \lambda K^*_{ij} + \frac{1}{2}K^1_{ij} + \frac{1}{3}K^2_{ij})x_j = 0. \tag{3.86}$$

The load independent arc-length equation implemented in the present work has the following form:

$$c = \|\Delta x_j\|^2 - \Delta l^2 = 0 \tag{3.87}$$

where Δl is a prescribed arc-length parameter defining the size of the increment, and Δx_j is the incremental solution vector, defined as:

$$\Delta x_j = x^n_j - x^{n-1}_j \tag{3.88}$$

where x_j^n is the solution vector at the current (nth) step, and x_j^{n-1} is the solution vector at the previous step.

In the following, *incremental* changes in the solution vector and loading parameter are denoted as Δx_j and $\Delta\lambda$, respectively, while *iterative* changes are denoted using δx_j and $\delta\lambda$, respectively. In order to apply the Newton-Raphson algorithm, the equations (3.86) and (3.87) must be linearized about a reference state ($\bar{x}_j$,$\bar{\lambda}$):

$$r_i(x_j,\lambda) \approx r_i(\bar{x}_j,\bar{\lambda}) + \frac{\partial r_i}{\partial x_j}(\bar{x}_j,\bar{\lambda})\delta x_j + \frac{\partial r_i}{\partial \lambda}(\bar{x}_j,\bar{\lambda})\delta\lambda = 0 \tag{3.89}$$

$$c(x_j,\lambda) \approx c(\bar{x}_j,\bar{\lambda}) + \frac{\partial c}{\partial x_j}(\bar{x}_j,\bar{\lambda})\delta x_j + \frac{\partial c}{\partial \lambda}(\bar{x}_j,\bar{\lambda})\delta\lambda = 0. \tag{3.90}$$

For the present application, the partial derivatives in these equations are as follows:

$$\frac{\partial r_i}{\partial x_j}(\bar{x}_j,\bar{\lambda}) = -K_{ij}^t \tag{3.91}$$

$$\frac{\partial r_i}{\partial \lambda}(\bar{x}_j,\bar{\lambda}) = q_i + K_{ij}^* x_j = \hat{f}_i \tag{3.92}$$

$$\frac{\partial c}{\partial x_j}(\bar{x}_j,\bar{\lambda}) = 2\Delta\bar{x}_j \tag{3.93}$$

$$\frac{\partial c}{\partial \lambda}(\bar{x}_j,\bar{\lambda}) = 0 \tag{3.94}$$

where K_{ij}^t is the tangent stiffness matrix given by

$$K_{ij}^t = K_{ij} + \lambda K_{ij}^* + K_{ij}^1 + K_{ij}^2. \tag{3.95}$$

If these expressions for the partial derivatives are substituted into equations 3.89 and 3.90, the following simultaneous linear equations are obtained:

$$K_{ij}^t \delta x_j = \bar{r}_i + \hat{f}_i \delta\lambda \tag{3.96}$$

$$2\Delta\bar{x}_j \cdot \delta x_j \quad = \quad \bar{c}. \tag{3.97}$$

The first of these equations may be solved for δx_j:

$$\delta x_j = (K_{ij}^t)^{-1}(\bar{r}_i + \hat{f}_i \delta\lambda) = \delta\bar{x}_j + \delta\hat{x}_j \delta\lambda \tag{3.98}$$

where

$$\delta\bar{x}_j \quad = \quad (K_{ij}^t)^{-1}\bar{r}_i \tag{3.99}$$

$$\delta\hat{x}_j \quad = \quad (K_{ij}^t)^{-1}\hat{f}_i. \tag{3.100}$$

Similarly, we may substitute the expression for δx_j (3.98) into equation 3.97 and solve for $\delta\lambda$:

$$\delta\lambda = \frac{-\bar{c} - 2\Delta\bar{x}_j \cdot \delta\bar{x}_j}{2\Delta\bar{x}_j \cdot \delta\hat{x}_j} = \frac{\Delta l^2 - \|\Delta\bar{x}_j\|^2 - 2\Delta\bar{x}_j \cdot \delta\bar{x}_j}{2\Delta\bar{x}_j \cdot \delta\hat{x}_j}. \tag{3.101}$$

At the n_{th} step, then, the iterations proceed by sequentially solving equation 3.101 and equation 3.98 for $\delta\lambda$ and δx_j, respectively. At the end of the i_{th} iteration, the updated x_j and λ are then obtained as follows:

$$x_j^n(i+1) \quad = \quad x_j^n(i) + \delta x_j \tag{3.102}$$

$$\lambda^n(i+1) \quad = \quad \lambda^n(i) + \delta\lambda. \tag{3.103}$$

The iterations converge when the expression

$$\varepsilon = \sqrt{\frac{\delta x_j \cdot \delta x_j}{x_j \cdot x_j}} \tag{3.104}$$

is less than a user specified error tolerance, $\hat{\varepsilon}$.

After the solution is converged at a given step, a new value for the arc-length parameter, Δl^{n+1}, must be chosen for use during the subsequent step. In the present implementation, the new arc-length parameter is chosen so as to keep the number of iterations at each step nearly constant. The user specifies the number of iterations that are desired at each step, $\bar{m}$. If the actual number of iterations required at a given step, m, is greater than $\bar{m}$, then a smaller arc-length parameter is chosen for the next step. If, on the other hand, the actual number of iterations required at a given step is less than $\bar{m}$, then a larger load increment is taken for the next step:

$$\Delta l^{n+1} = \frac{\bar{\mathrm{m}}}{\mathrm{m}} \Delta l^{n}. \tag{3.105}$$

This scheme allows the solver to take large steps along the load-displacement path when the solution is converging easily, and forces the solver to take smaller steps when convergence is more difficult. The solver is thus able to adapt in a crude manner to the particular problem that is being solved.

Once a value for Δl^{n+1} is determined, the solution algorithm attempts to predict values for x_j and λ^{n+1} at the new arc-length increment. These predicted values are then used as "initial guesses" for the iterations at step $n + 1$. In the present implementation, quadratic Lagrange interpolation functions are fit through the previous three converged steps and used to extrapolate the predictors. If there is not sufficient accumulated data for quadratic extrapolation (for example, at the beginning of the solution procedure), the arc-length constraint equation (3.87) is used to obtain the predictors. Details of both prediction procedures may be obtained in [57].

Both the "full" Newton-Raphson and the "modified" Newton Raphson iterative procedures were implemented in `NLISA`. In the latter procedure, the tangent stiffness matrix (see equation 3.98) is only factored once at the beginning of each step; it is not updated with the new values of the displacement field at the end of each iteration. Using the modified solution procedure, `NLISA` experienced convergence difficulties for several test cases. As a consequence, the full Newton-Raphson solution procedure was used throughout the present work.

3.6 Calculation of Forces and Moments

After a non-linear solution is obtained for a given value of λ, force and moment quantities may be calculated using equations (3.27) through (3.32). In particular, it is useful to calculate the total longitudinal force, $\hat{F}_x$ at a given x location. For a given structure, and at a given x coordinate, this quantity is determined by first integrating N_x over the width of each finite strip comprising the structure. This gives the total longitudinal force acting on the strip. $\hat{F}_x$ may then be obtained by summing the forces acting on each strip:

$$\hat{F}_x = \sum_{i=1}^{N} \int_{-b/2}^{b/2} N_x \, dy. \tag{3.106}$$

In Chapter 4, results generated by the present analysis are compared to those presented in the literature. In some of this literature, the average longitudinal force, $\bar{F}_x$, is calculated. This quantity is obtained by integrating $\hat{F}_x$ over the length of the structure and then dividing the result by this length:

$$\bar{F}_x = \frac{1}{L} \int_0^L \hat{F}_x \, dx = \frac{1}{L} \int_0^L \sum_{i=1}^{N} N_x \, dx \, dy. \tag{3.107}$$

3.7 Reduced Basis Methodology

The general approach used in the present research is based on that described in the paper entitled "Two-Stage Rayleigh-Ritz Technique for Non-linear Analysis of Structures" by A.K. Noor, J.M. Peters, and C.M. Anderson [4]. The purpose of the technique described in this paper was to improve the computational efficiency of the conventional Rayleigh-Ritz method by reducing the number of degrees of freedom in the discretized structure. An outline of the two-stage Rayleigh-Ritz method is given here.

In the first stage of the two-stage Rayleigh-Ritz method, the conventional Rayleigh-Ritz technique is applied to discretize the structure. The s generalized displacements of the structure, ψ_i $(i = 1, s)$ are expressed in terms of a series of known functions as follows:

$$\psi_i = \sum_{k=1}^{m} f^k \zeta_i^k \tag{3.108}$$

where f^k are known functions of the spatial coordinates which satisfy the essential boundary conditions of the problem and ζ_i^k are undetermined coefficients. These expressions for the generalized displacements are then substituted into the expression for the total potential energy, Π. After taking the first variation of Π and setting it equal to zero, a set of non-linear algebraic equations is obtained in terms of the vector of unknown coefficients, ϑ_j, where ϑ_j has dimension $n = ms$ and contains the coefficients ζ_i^k $(i = 1, s)$. In general, the resulting system equations have the following form:

$$K_{ij}\vartheta_j + G_i(\vartheta_j) - qQ_i = 0 \tag{3.109}$$

where K_{ij} is an n by n linear stiffness matrix, G_i is a vector of non-linear terms, Q_i is a vector of external forces, and q is a loading parameter.

In the second stage of Two-Stage Rayleigh Ritz technique, the vector ϑ_j is approximated by a linear combination of r basis vectors as follows:

$$\vartheta_j = \Gamma_{jl}\Delta_l \tag{3.110}$$

where Γ_{jl} is an n by r matrix whose columns are the basis vectors, and Δ_l is a vector of reduced unknowns $(l = 1, r)$. In general, $r \ll n$. The basis vectors used in this case are ϑ_j itself evaluated at a particular value of q, and the successive derivatives of ϑ_j with respect to a path parameter, λ, each evaluated at the same value of q. λ may be identified with q or with a similar displacement parameter. Collectively, these basis vectors are referred to as the "path derivatives" of the response. Γ_{jl} has the following form:

$$\Gamma_{jl} = \left\{ \begin{array}{ccccc} \vartheta_j & \partial\vartheta_j/\partial\lambda & \partial^2\vartheta_j/\partial\lambda^2 & \cdots & \partial^{r-1}\vartheta_j/\partial\lambda^{r-1} \end{array} \right\}. \tag{3.111}$$

The Rayleigh-Ritz technique is then applied a second time to reduce the n equations in equation (3.109) to the following reduced system of r equations:

$$\tilde{K}_{kl}\Delta_l + \tilde{G}_l(\Delta_l) - q\tilde{Q}_l = 0 \tag{3.112}$$

where

$$\tilde{K}_{kl} = \Gamma^T_{ik} K_{ij} \Gamma_{jl} \tag{3.113}$$

$$\tilde{G}_l(\Delta_l) = \Gamma^T_{il} G_i(\Delta_l) \tag{3.114}$$

$$\tilde{Q}_l = \Gamma^T_{il} Q_i. \tag{3.115}$$

$G_i(\Delta_l)$ is obtained from $G_i(\vartheta_j)$ by replacing ϑ_j by its expression in terms of Δ_l, equation (3.110). The range of λ over which these reduced system equations provide an accurate representation of the original discretized equations, equation (3.109), will depend on the non-linearity of the problem.

The authors of [4] present numerical results for several simple non-linear problems of axis-symmetrically loaded clamped isotropic shallow spherical shells. They go on to note, however, that "The full potential of the two-stage Rayleigh-Ritz technique presented herein can best be realized when solving non-linear problems of structures with simple geometry but complex construction (such as stiffened plates and shells)."

In the present research, the two-stage Rayleigh-Ritz technique is applied to the problem of the geometrically non-linear analysis of compressively loaded prismatic composite structures. This includes the non-linear analysis of stiffened aircraft panels and various thin-walled open and closed section columns used in civil engineering applications. Here, the (global) classical Rayleigh-Ritz technique of the first stage is replaced by a piecewise application of the Rayleigh-Ritz technique, the finite strip method. The finite strip analysis developed for this purpose was described in earlier in this chapter. In what follows, the application of the two-stage Rayleigh-Ritz technique to the non-linear finite strip analysis will be described.

3.7.1 Generation of the Path Derivatives

The basis vectors used in the second stage of the two-stage Rayleigh-Ritz technique are the path derivatives of the discretized system equations generated in the first stage. In the present work, the expressions for the path derivatives are obtained by differentiating the discretized equilibrium equations (3.66). The expressions used to calculate the first five path derivatives are as follows (based on [59]):

$$K^t_{ij}x'_j = -(q_i + K^*_{ij}x_j) \tag{3.116}$$

$$K^t_{ij}x''_j = -(\frac{\partial K^1_{ij}}{\partial x_k}x'_k x'_j + \frac{\partial K^2_{ij}}{\partial x_k}x'_k x'_j + K^*_{ij}x'_j) \tag{3.117}$$

$$K^t_{ij}x'''_j = -(\frac{\partial K^1_{ij}}{\partial x_k}(3x'_k x''_j) + \frac{\partial K^2_{ij}}{\partial x_k}(3x'_k x''_j) + \frac{\partial^2 K^2_{ij}}{\partial x_k \partial x_l}x'_l x'_k x'_j + K^*_{ij}x''_j) \tag{3.118}$$

$$\begin{aligned} K^t_{ij}x^{(iv)}_j = & -(\frac{\partial K^1_{ij}}{\partial x_k}(4x'_k x'''_j + 3x''_k x''_j) + \frac{\partial K^2_{ij}}{\partial x_k}(4x'_k x'''_j + 3x''_k x''_j) + \\ & \frac{\partial^2 K^2_{ij}}{\partial x_k \partial x_l}(6x'_l x'_k x''_j) + K^*_{ij}x'''_j) \end{aligned} \tag{3.119}$$

$$\begin{aligned} K^t_{ij}x^{(v)}_j = & -(\frac{\partial K^1_{ij}}{\partial x_k}(5x'_k x^{(iv)}_j + 10x''_k x'''_j) + \frac{\partial K^2_{ij}}{\partial x_k}(5x'_k x^{(iv)}_j + 10x''_k x'''_j) + \\ & \frac{\partial^2 K^2_{ij}}{\partial x_k \partial x_l}(15x'_l x''_k x''_j + 10x'_l x'_k x'''_j) + K^*_{ij}x^{(iv)}_j) \end{aligned} \tag{3.120}$$

where the prime superscripts refer to differentiation with respect to the path parameter, λ. The tangent stiffness matrix K^t_{ij}, which appears on the left hand side of all the above equations, needs to be factored only once independently of the number of path derivatives that are generated. In generating values for terms such as $\frac{\partial \bar{K}^1_{ij}}{\partial x_k} x'_k x'_j$ and $\frac{\partial^2 \bar{K}^2_{ij}}{\partial x_l \partial x_k} x'_l x'_k x'_j$ in the above equations, it is necessary to first compute these terms for each individual finite strip. Note that

$$\frac{\partial \bar{K}^1_{ij}}{\partial x_k} = \bar{A}^1_{ijk} \tag{3.121}$$

$$\frac{\partial \bar{K}^2_{ij}}{\partial x_k} = \bar{A}^2_{ijkl} x_l \tag{3.122}$$

$$\frac{\partial^2 \bar{K}^2_{ij}}{\partial x_l \partial x_k} = \bar{A}^2_{ijkl} \tag{3.123}$$

where $\bar{A}^1_{ijk}$ and $\bar{A}^2_{ijkl}$ are as described by equation (3.61), and the over-bars indicate quantities referring to a single finite strip. The resulting local vectors are then assembled to form the required global quantities.

The present analysis is capable of calculating path derivatives up to the 11th derivative. The accuracy of the code was verified using finite differences in the case of the first and second order derivatives.

3.7.2 Reduced Solution Procedure

The solution procedures used for the reduced problem are described in this section. The general procedure is similar to that described in [4]; a flow chart of the solution procedure is shown in Figure 3.2.

First, r path derivatives are generated for the structure in the unloaded state ($\lambda = 0$). These derivatives are used to form the matrix Γ_{jl} as follows (see equation (3.111)):

$$\Gamma_{jl} = \left\{ \begin{array}{ccccc} x_j & x'_j & x''_j & \cdots & x_j^{(r-1)} \end{array} \right\}. \tag{3.124}$$

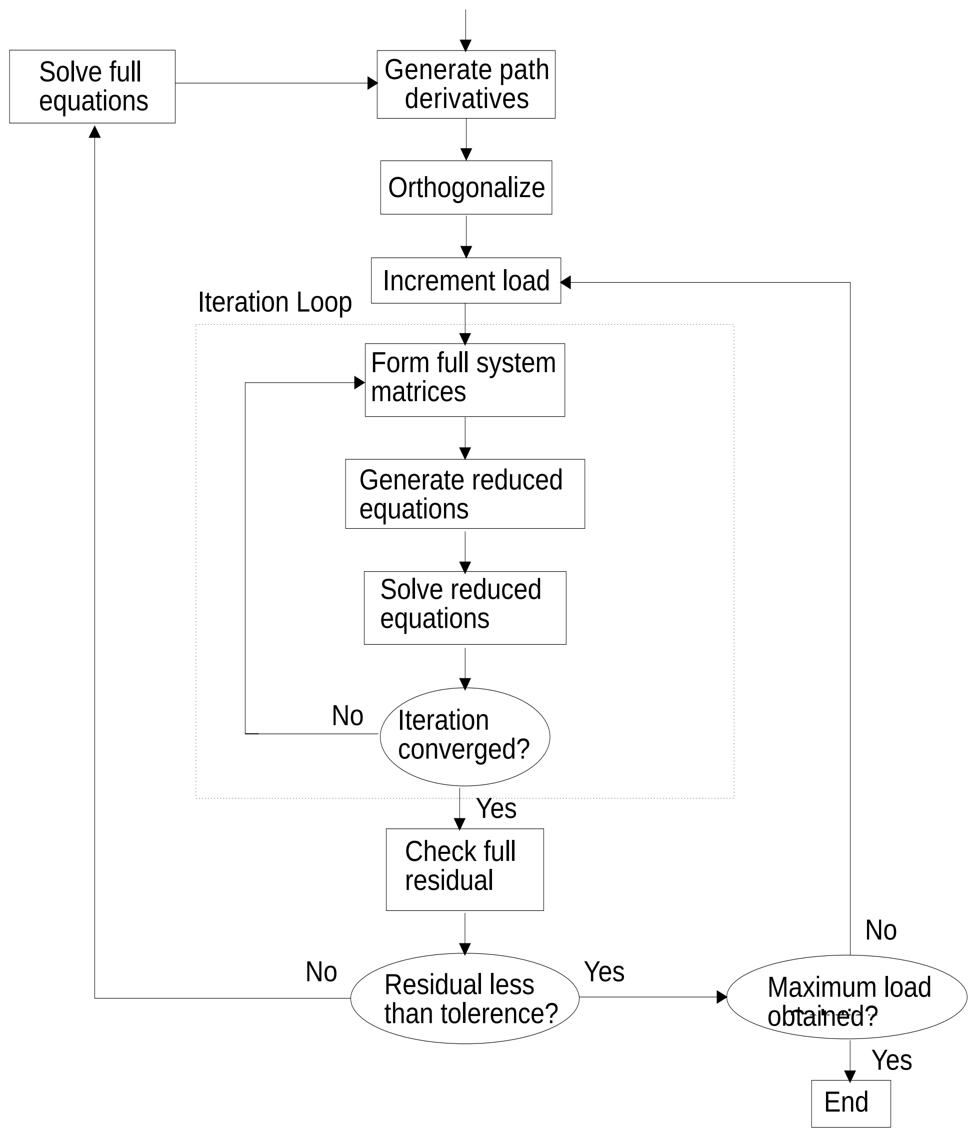

Figure 3.2: Solution procedure

The number of basis vectors generated, r, depends on the condition number, γ, of the resulting Gram matrix:

$$G_{jk} = \Gamma_{jl}\Gamma^T_{kl}. \tag{3.125}$$

After each new path derivative is generated, the condition number of the resulting G_{jk} matrix is estimated. The condition number of this matrix generally grows larger as more path derivatives are added; a large condition number indicates that the basis vectors are becoming linearly dependent. When the condition number exceeds a user-specified tolerance, $\hat{\gamma}$, no additional path derivatives are generated.

During the course of the present work, it was determined that convergence of the reduced problem was facilitated by orthogonalizing the columns of Γ_{jl} before proceeding. This is accomplished using a QR orthogonalization procedure [60]. The resulting orthogonalized matrix is then used to reduce the size of the system equations:

$$\begin{aligned}
\tilde{K}_{kl} &= \Gamma^T_{ik} K_{ij} \Gamma_{jl} && (3.126)\\
\tilde{K}^*_{kl} &= \Gamma^T_{ik} K^*_{ij} \Gamma_{jl} && (3.127)\\
\tilde{K}^1_{kl} &= \Gamma^T_{ik} K^1_{ij} \Gamma_{jl} && (3.128)\\
\tilde{K}^2_{kl} &= \Gamma^T_{ik} K^2_{ij} \Gamma_{jl} && (3.129)\\
\tilde{q}_l &= \tilde{\Gamma}^T_{il} q_i. && (3.130)
\end{aligned}$$

The reduced system equations have the following form:

$$\lambda\tilde{q}_k + (\tilde{K}_{kl} + \lambda\tilde{K}^*_{kl} + \frac{1}{2}\tilde{K}^1_{kl} + \frac{1}{3}\tilde{K}^2_{kl})\tilde{x}_l = 0 \tag{3.131}$$

where the solution vector x_j for the finite strip analysis may be recovered from the reduced solution vector, as follows:

$$x_j = \Gamma_{jl}\tilde{x}_l. \tag{3.132}$$

After incrementing λ, the reduced equations (3.131) are solved using the same Newton-Raphson incremental/iterative arc length technique used to solve the full finite strip equations (section 3.5). It is noted that although the system matrices of the reduced problem have been reduced to dimension r, it is still necessary to form (but not factor) the full system matrices at each Newton iteration. This is because the reduced system matrices are not known explicitly as a function of the reduced solution vector, $\tilde{x}_l$. The reduced system matrices are obtained by first forming the full system matrices and then reducing them using equations (3.126) through (3.130). This operation constitutes the majority of the computational cost of the reduced solution procedure.

At the end of each increment of the reduced solution, the residual vector r_j (3.86) is formed for the "full" finite strip analysis. A weighted norm of this residual, e, is then used to determine whether to generate a new set of basis vectors. This norm is defined as follows:

$$e = \frac{1}{N}\sqrt{\frac{r_j \cdot x_j}{x_j \cdot x_j}} \tag{3.133}$$

where N is the number of degrees of freedom in the full solution vector. If e is less than a user specified tolerance, $\hat{e}$, then no new basis vectors are formed. The loading parameter, λ, is incremented and the reduced solution continues with the current set of basis vectors. If, on the other hand, e is greater than $\hat{e}$, a new set of basis vectors is generated. First, a series of Newton-Raphson iterations are performed using the full system equations at the current value of λ in order to reduce the full residual vector, r_i, to zero. A new set of r basis vectors is then generated and a new set of reduced system equations are formed. The (already calculated) QR factorization is used to provide a least squares estimate of the new reduced solution vector $\tilde{x}_l$, corresponding to the new set of basis vectors. The reduced solution then proceeds with the new set of basis vectors.

As will be discussed in Chapter 4, the error tolerance, e, has a large influence on the robustness and efficiency of the reduced solution procedure. During the implementation of the method, several alternative expressions for the error tolerance, e were investigated. In a limited number of tests, the present expression, equation 3.133, proved to be the most successful.

Chapter 4

Results: Non-linear Finite Strip Analysis

In this chapter, results obtained using the non-linear finite strip analysis in conjunction with the reduced basis solution procedure are presented. Comparisons are made to results presented in the literature, and the accuracy, efficiency, and robustness of both the full and reduced `NLISA` analyses are assessed.

All results presented in this chapter were obtained using the IBM SP2 Scalable Parallel Processor Machine at Virginia Tech. The SP2 is composed of nodes which are POWER2 architecture RS/6000 processors with their own memory and disk drive. The present code does not utilize the parallel capabilities of the machine, however; it currently runs on a single node at a time. This machine was selected because of its availability and because of the robust FORTRAN 90 compiler which is installed.

For each set of results obtained using the reduced solution procedure, the user specified condition number tolerance $\hat{\gamma}$ was set to a value of 1e20. Recall from section 3.7 that this value controls the *number* of basis vectors that are generated at a given solution step (up to a maximum of 11 vectors). The user specified tolerance $\hat{e}$ (which determines whether or not *any* basis vectors are generated at a given solution step) varied to some degree from problem to problem, and is reported separately for each problem.

4.1 Selection of Longitudinal Terms

As will be demonstrated, the number of longitudinal terms included in a given analysis influences both the accuracy and the computational cost of both the full and reduced solution procedures. If large numbers of longitudinal terms are included in the analysis, the accuracy of the solution will usually be high, as will the computational cost. If a small number of longitudinal terms are used, the accuracy of the solution may be degraded (depending on the problem and the terms used), but the computational cost will be reduced.

The selection of which terms to include in a given analysis is not necessarily straightforward, and will be governed by the nature of the problem and the analyst's judgment. If the number of half-waves into which the structure will buckle is known ahead of time (from a bifurcation buckling analysis, for example), this fact can be used as a guide to selecting the appropriate terms. For example, the analyst has prior knowledge that the structure will initially buckle in five half-waves in the longitudinal direction, the analyst can make sure that the corresponding five half-wave terms are included in the analysis. Usually it will be necessary to include additional higher order terms as well in order to capture the subtleties of the postbuckling displacement field. In general, caution should be exercised when excluding longitudinal terms from the solution procedure, especially at higher load levels when the displacement field may differ from the initial buckling mode shape.

In the following example problems, longitudinal terms were selected based on the known structural response and, in some cases, using trial and error. At present, the `NLISA` code does not allow the analyst to arbitrarily select longitudinal terms to be included in the analysis – the user must select ordered sequences such as terms 1 to 15 in steps of 3, or terms 2 to 10 in steps of 4, for example.

4.2 Postbuckling of Unstiffened Panels

The first set of example problems are isotropic and composite flat plates with various side edge boundary conditions. Although the full analysis is capable of solving these problems very efficiently (there is usually no need to use the reduced solution technique), these problems were used to test and debug both analysis methods. In each case, the plates are loaded via end shortening at the longitudinal ends, which are simply supported in the out-of-plane direction and are assumed to behave orthotropically in bending. Because of the assumed displacement field for the v displacement component (see Chapter 3), the v displacement is constrained to be zero at the at the loaded edges.

4.2.1 Example 1 – S-S Square Isotropic Plate (v free)

The first example (Figure 4.1) is an isotropic square plate with the transverse ends simply supported in the out-of-plane direction and the v displacement component un-restrained along the transverse ends. The ratio of the plate length, L, to the plate thickness, H, is 120, and ν=1/3.

Results were obtained using a (symmetric) four strip model representing half of the total plate width. The v and w displacement components were each represented using the first three odd longitudinal series terms, $sin(\pi x/L)$, $sin(3\pi x/L)$, and $sin(5\pi x/L)$ ($m = 1, 3, 5$ and $n = 1, 3, 5$). The u displacement component was represented using the first two even longitudinal series terms, $sin(2\pi x/L)$ and $sin(4\pi x/L)$ ($k = 2, 4$). A w imperfection field in the shape of a half sine wave in both the longitudinal and lateral directions was assumed to be present. The maximum amplitude of this imperfection was taken to be 0.1% of the plate thickness.

In Figure 4.2, the load factor F is plotted against the loading parameter λ. In this plot, $\lambda = 1.0$ corresponds to the critical end-shortening strain.

In Figure 4.3, the central displacement of the plate normalized by the plate thickness is plotted against a load factor, F, where

$$F = \frac{\bar{F}_x L}{\pi^2 E H^3}. \tag{4.1}$$

In this expression, E is the elastic modulus and $\bar{F}_x$ is the average longitudinal force as defined in Chapter 3:

$$\bar{F}_x = \frac{1}{L} \sum_{i=1}^{N} \int_{-b/2}^{b/2} \int_0^L N_x \, dx \, dy. \tag{4.2}$$

In both figures, the "plus" shaped markers represent data points obtained using the full solution procedure, and the circular markers represent data obtained using the reduced solution procedure. The reduced solution procedure required only one set of basis vectors in order to obtain excellent agreement with the full solution. This set of basis vectors was generated at the beginning of the solution procedure; this was the only time that it was necessary to factor the full system equations. Recall from Chapter 3 that the reduced solution procedure generates a new set of basis vectors whenever the residual error, e, exceeds a user specified error tolerance, $\hat{e}$. The error tolerance for this problem (which was not exceeded), was set to a relatively large value of 0.25.

Also in Figures 4.3 and 4.2, the reduced solution is compared to analytical results presented in a paper by Azizian and Dawe [3]. Azizian and Dawe's analysis is a non-linear finite strip analysis essentially the same as the full analysis developed in the present work. As such, agreement between the two sets of results should be very close. The primary difference between the two analyses concerns the modeling of the displacement fields in the lateral (y) direction. Azizian and Dawe approximate the membrane displacement components using quadratic polynomials and the out of plane displacement components using cubic polynomials (in comparison, the present analysis uses cubic polynomials to approximate all of the displacement components). In the longitudinal direction, Azizian and Dawe use the first three even trigonometric terms (2,4,6) to approximate the u displacement component, the

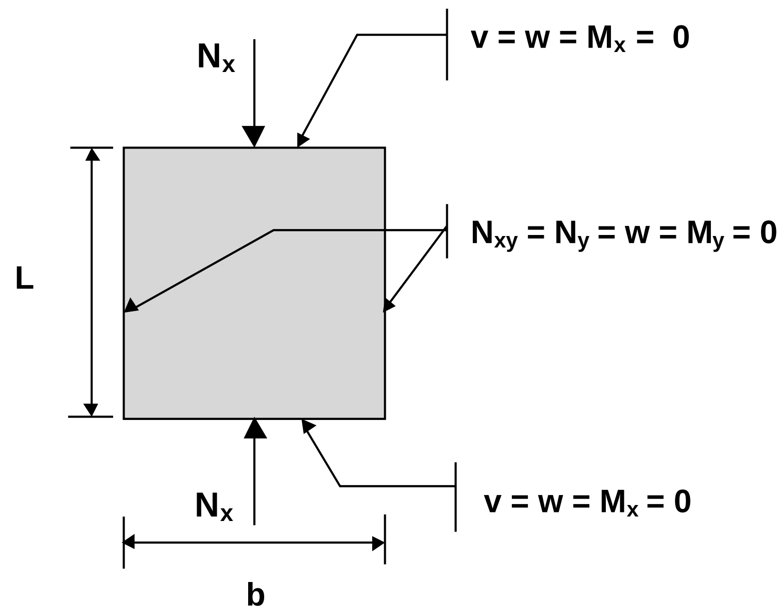

Figure 4.1: Example 1 – simple-simple (v free)

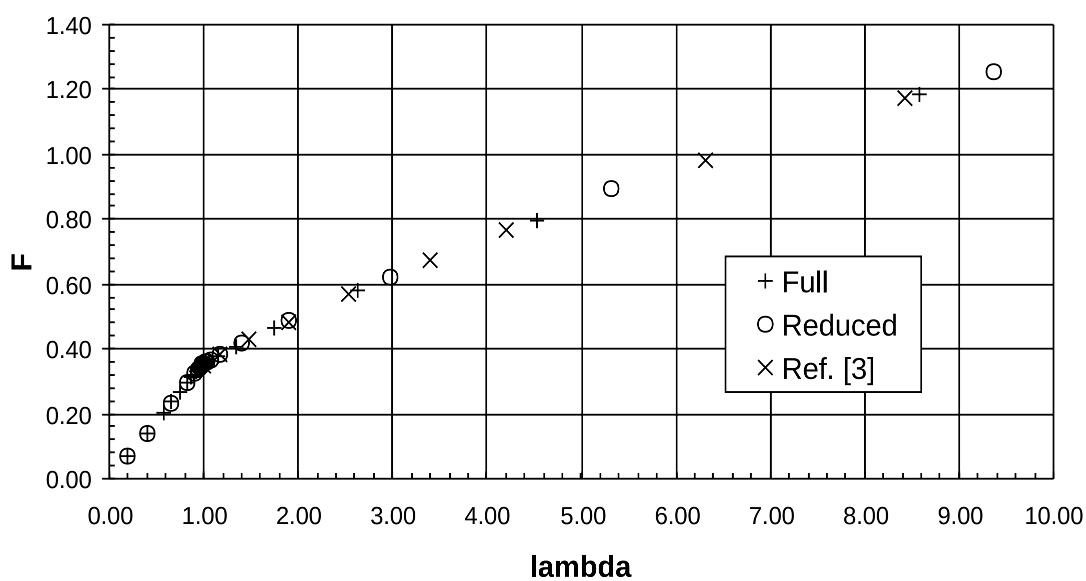

Figure 4.2: Example 1 – F vs. λ
symmetric model – 4 strips; $k = 2, 4$; $m = 1, 3, 5$; $n = 1, 3, 5$

first four odd terms (1,3,5,7) to approximate the v displacement component, and the first two odd terms (1,3) to approximate the w and displacement component. As in the present analysis, Azizian and Dawe used four finite strips to model the half-plate. As expected, agreement between Azizian and Dawe's solution and the present solution is excellent.

As a qualitative demonstration of the ability of the `NLISA` analyses to generate results corresponding to different imperfection amplitudes, additional solutions for this problem were obtained with maximum imperfection amplitudes of 1.0% and 10.0% of the plate thickness. As before, the imperfection shape is a half sine wave in both the longitudinal and lateral directions. Plots of the total normalized displacement (including the imperfection contribution) vs. the load factor, F, are shown in Figure 4.4. The varying imperfection amplitudes do not significantly affect the solution in the more advanced postbuckling regime, but below $w/H = 1$, the effects of the imperfection are evident. As expected, the plot corresponding to the 0.1% imperfection amplitude exhibits a sharp break near the theoretical buckling load, whereas the plot corresponding to the 10.0% imperfection amplitude curves continuously from the onset of loading.

4.2.2 Example 2 – S-S Square Isotropic Plate (v restrained)

The second example (Figure 4.5) is identical to example 1, except that the v displacement component is now completely restrained along the transverse ends. As before, the ratio of the plate length, L, to the plate thickness, H, is 120, and ν=1/3.

As with Example 1, results were obtained using a (symmetric) four strip model representing half of the total plate width. The v and w displacement components were each represented using the first three odd longitudinal series terms ($m = n = 1, 3, 5$) and the u displacement component was represented using the first two even longitudinal series terms ($k = 2, 4$). A w imperfection field in the shape of a half sine wave in both the longitudinal and lateral directions was assumed to be present. The maximum amplitude of this imperfection was again taken to be 0.1% of the plate thickness.

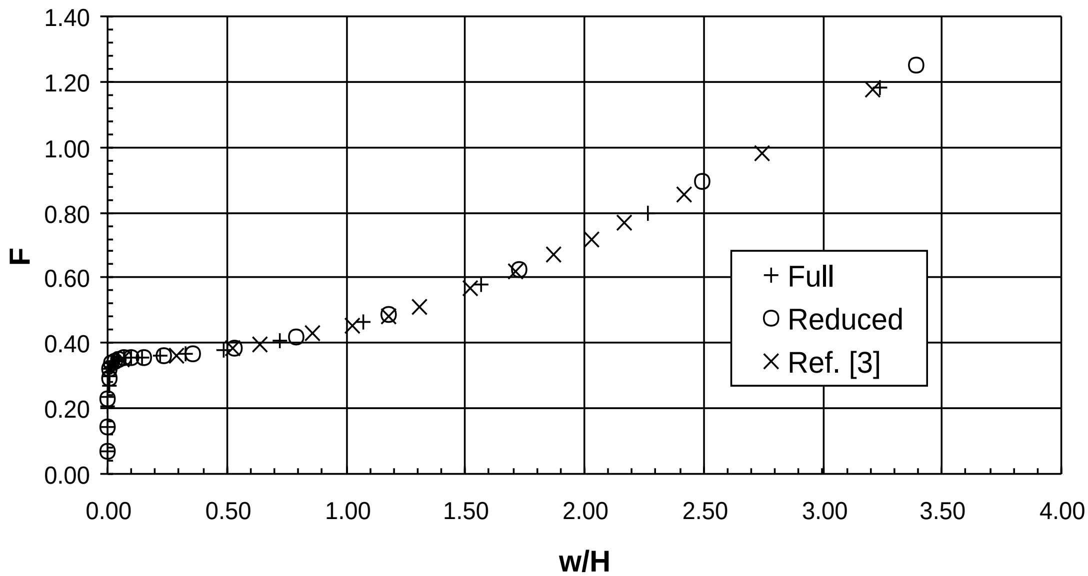

Figure 4.3: Example 1 – F vs. w/H
symmetric model – 4 strips; $k = 2, 4$; $m = 1, 3, 5$; $n = 1, 3, 5$

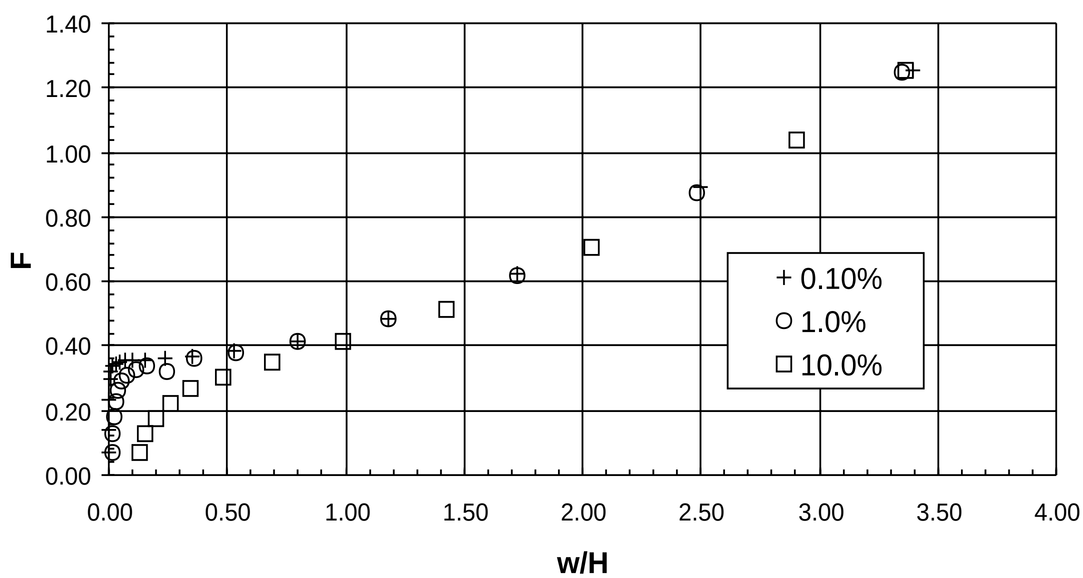

Figure 4.4: Example 1 – F vs. w/H
various imperfection amplitudes

Both the full and reduced solutions are plotted in Figures 4.6 and 4.7. In Figure 4.6, F is plotted against λ, where $\lambda = 1.0$ corresponds to the critical end-shortening strain, and in Figure 4.7, F is plotted against the normalized w displacement at the center of the plate. In order to obtain an accurate reduced solution in this case, it was necessary to specify a residual error tolerance, $\hat{e}$, of 0.05. This tolerance was exceeded at $\lambda \approx 1.15$, and $\lambda \approx 8.00$, and a new set of basis vectors was generated in each case (these points are marked by filled circles in Figure 4.6). The numbers in square brackets indicate the number of basis vectors generated in each case. Error tolerances greater than 0.05 resulted in reduced solutions which began to diverge from the full solution at these points.

Comparisons between the reduced solution and reference [3] are also presented in Figures 4.6 and 4.7. Azizian and Dawe's analysis is the same as that described for Example 1. Agreement between their results and the present results is excellent.

4.2.3 Examples 3, 4 and 5 – Various Side Edge Boundary Conditions

In order to test the capability of the present procedure to obtain solutions for a variety of side edge boundary conditions, three additional isotropic square plate problems were solved. These problems correspond to side edge boundary conditions of clamped-clamped (Figure 4.8), free-free (Figure 4.9), and simple-free (Figure 4.10). The boundary conditions for the simply supported edges are the same as those used for Example 1 (v displacement unrestrained).

For Example 3 (clamped-clamped) and Example 4 (free-free), a half-model consisting of four finite strips was used to obtain the results. For Example 5, a full model consisting of eight finite strips (four finite strips in each half) was used. In all three examples, the first three odd longitudinal series terms were used to represent the v and w displacement components ($m = n = 1, 3, 5$), and the first two even longitudinal series terms ($k = 2, 4$) were used to represent the u displacement component.

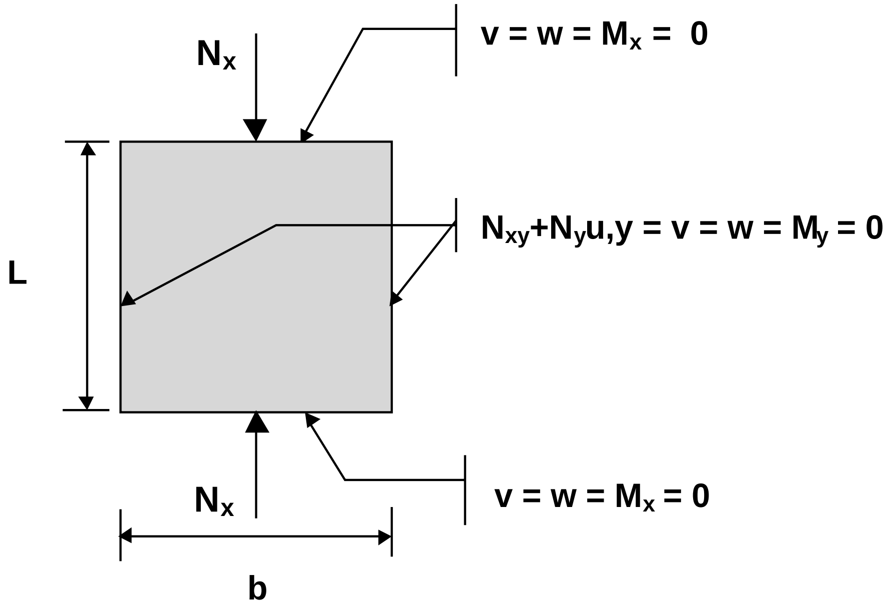

Figure 4.5: Example 2 – simple-simple (v restrained)

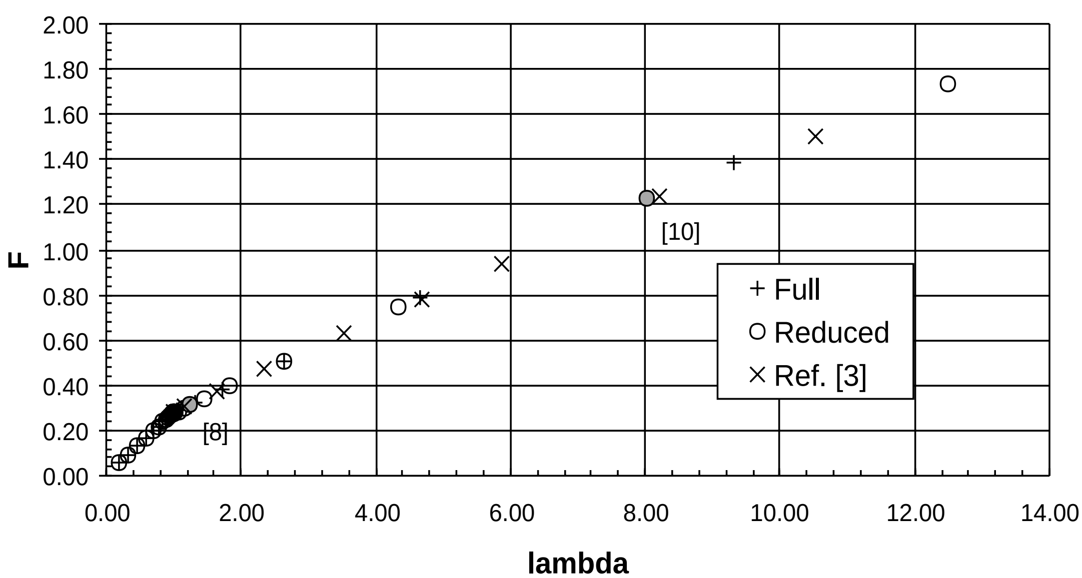

Figure 4.6: Example 2 – F vs. λ
symmetric model – 4 strips; $k = 2, 4$; $m = 1, 3, 5$; $n = 1, 3, 5$

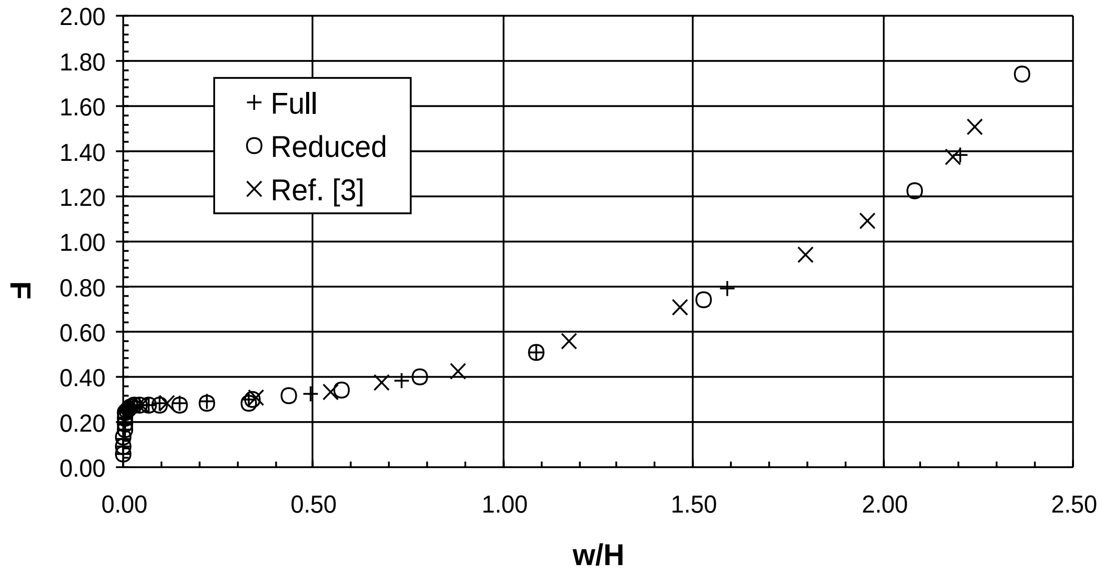

Figure 4.7: Example 2 – F vs. w/H
symmetric model – 4 strips; $k = 2, 4$; $m = 1, 3, 5$; $n = 1, 3, 5$

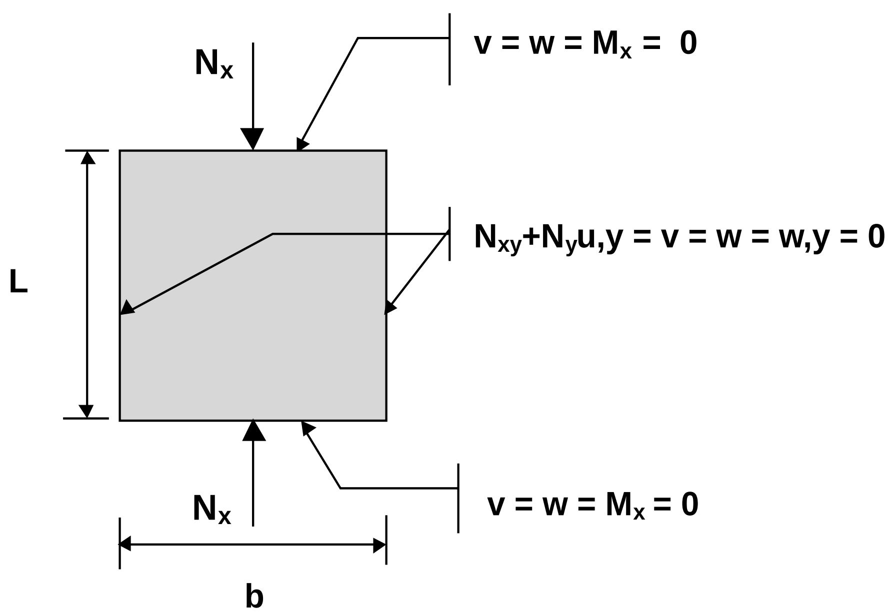

Figure 4.8: Example 3 – clamped-clamped

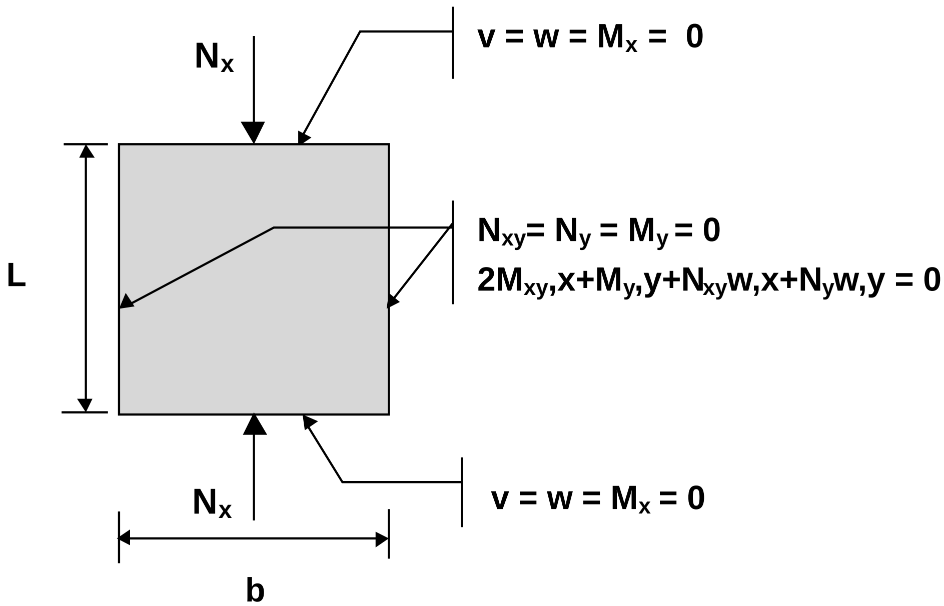

Figure 4.9: Example 4 – free-free

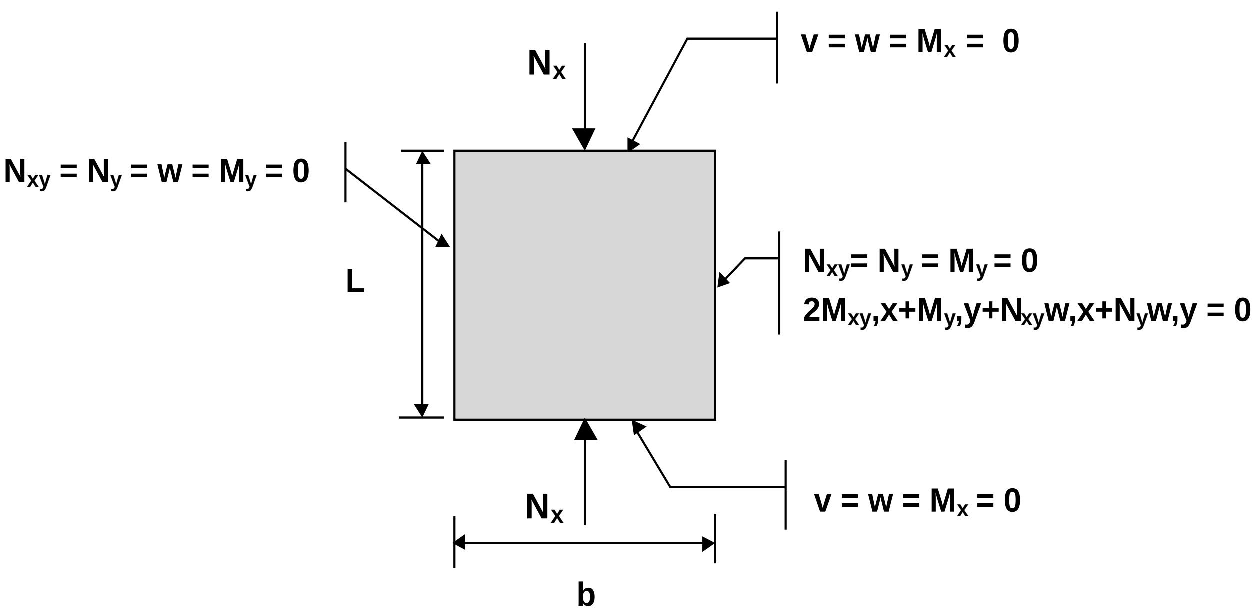

Figure 4.10: Example 5 – simple-free

Results obtained with the reduced solution procedure are plotted in Figures 4.11 and 4.12. In Figure 4.11, the load factor, F, is plotted against the normalized central plate displacement, w/H, and in Figure 4.12, F is plotted against λ. In the clamped-clamped and free-free cases, agreement with the full solution (not shown) was obtained with the residual error tolerance, $\hat{e}$ set to 0.075. Basis vectors were re-calculated three times during the clamped-clamped solution procedure; it was not necessary to re-calculate basis vectors in the free-free case. Note that the free-free plate has no postbuckling strength. In the simple-free case, it was necessary to reduce $\hat{e}$ to 0.050 in order to obtain agreement with the full solution over the full loading range. Basis vectors were re-calculated once in this case. The points at which basis vectors were re-calculated are shaded gray in Figure 4.11. In Figure 4.12, $\lambda = 1.0$ corresponds to the critical strain for Example 1.

4.2.4 Example 6 – S-S Square Graphite-Epoxy Plate (v restrained)

Results are presented in this section for a square graphite-epoxy plate. The transverse ends of the plate are simply supported, and the v displacement component is completely restrained. These are the same boundary conditions as were used in Example 2 (Figure 4.5. The length and width of the plate are each 20 in, and the laminate has a total thickness, H, of 0.12 in. The stacking sequence is $(\pm 30)_{ns}$, where n is sufficiently large so that the the assumption of zero D_{16} and D_{26} laminate constants is valid. The material properties for each lamina are E_1=19.01e6 psi, E_2=1.89e6 psi, G_{12}=0.93e6 psi, and ν_{12}=0.38.

The results of `NLISA` analyses are compared to analytical results obtained by Shin [61]. Shin's analysis is an adaptation of the method of the Marguerre energy method [62] to orthotropic plates. The out-of-plane displacement component, w, is expressed using a sin series in both the longitudinal and lateral directions and the potential energy is written in terms of this displacement field and the stress function, Φ. The resulting system of nonlinear algebraic equations is solved to obtain the structural response. In obtaining his results, Shin used terms corresponding to w_{11}, w_{31}, w_{13}, w_{33}, w_{15}, and w_{51}.

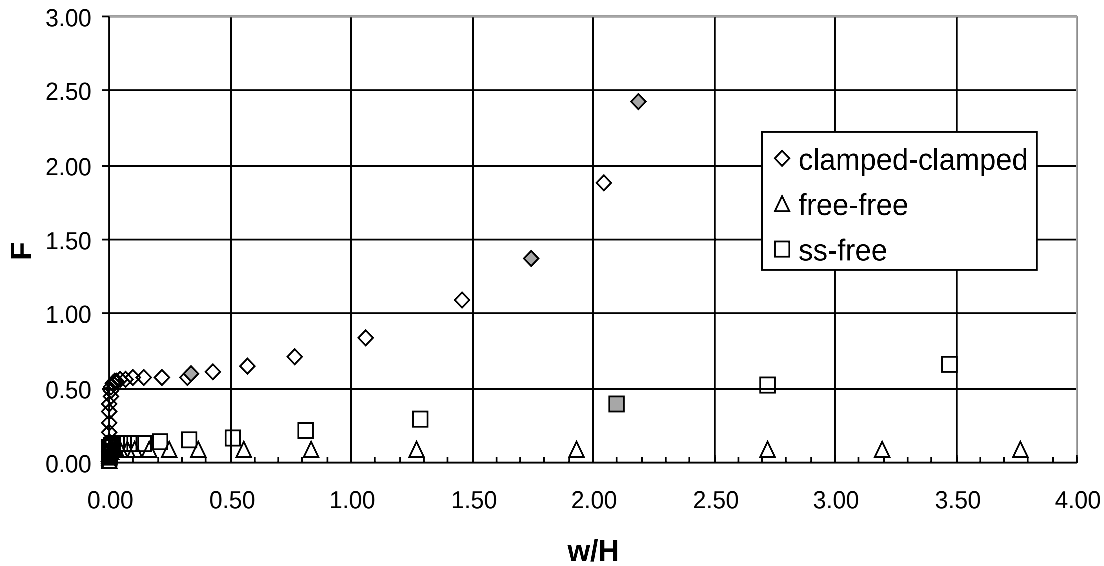

Figure 4.11: Examples 3, 4, 5 – F vs. w/H
$k = 2, 4$; $m = 1, 3, 5$; $n = 1, 3, 5$

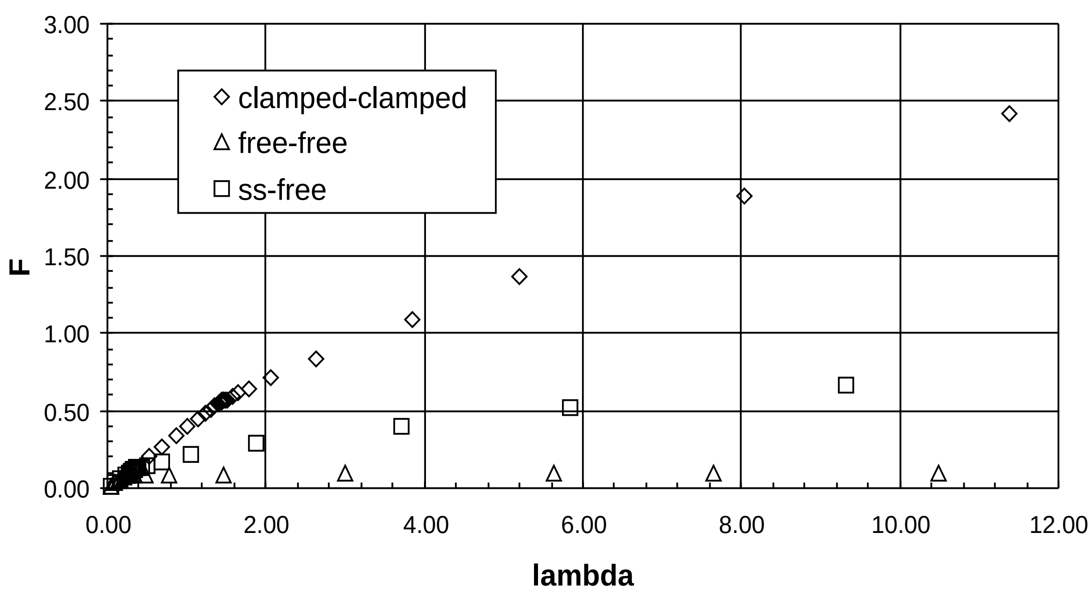

Figure 4.12: Examples 3, 4, 5 – F vs. λ
$k = 2, 4$; $m = 1, 3, 5$; $n = 1, 3, 5$

A comparison between the present results and Shin's results is presented in Figure 4.13. The normalized end shortening, λ, is plotted against the normalized central displacement, w/H. The `NLISA` results were obtained with a symmetric half-model with eight finite strips in the half-plate. The first five even longitudinal terms ($k = 2, 4, 6, ..., 10$) were used for the u displacement component, and the first five odd longitudinal terms ($m = n = 1, 3, 5, ..., 9$) were used for the v and w displacement components. Agreement between the two sets of results is generally good, with the present analysis slightly under-predicting the central displacement compared to Shin's analysis above $\lambda \approx 6.0$. The reduced solution was obtained no re-computations of the basis vectors ($\hat{e}$=0.050). Both full and reduced solutions were obtained in approximately 30s using an IBM RS/6000 model 390 computer.

4.2.5 Example 7 – Rectangular Graphite-Epoxy Plate

In this section, the postbuckling behavior of a flat, rectangular, graphite-epoxy plate is investigated. This panel was examined as part of an experimental study performed in [63], where it was loaded in axial compression. The panel was also analyzed in [64] using the finite element method, where comparisons between the analytical and experimental results were presented. The panel, (referred to as panel C4 in [63] and [64]) is a 24 ply orthotropic laminate with a $(\pm 45/0_2/\pm 45/0_2/\pm 45/0/90)_s$ stacking sequence and is 20.0 *in* long and 7.0 *in* wide. Material properties are given as E_1=19.0E6 *psi*, E_2=1.89E6 *psi*, G_{12}=0.93E6 *psi*, and ν_{12}=0.38. The lamina thickness is 0.0055 *in*. The loaded ends of the panel were clamped during testing, and the unloaded ends were simply supported using knife edge restraints. The panel was observed to buckle into two half-waves in the longitudinal (loading) direction, and one half-wave in the transverse direction.

Although `NLISA` is not capable of modeling clamped ends at the loaded edges, it was felt that the panel's aspect ratio was sufficiently large ($\approx$ 2.86) so as to allow `NLISA` to make a reasonable approximation to the panel response. Using `NLISA`, the plate was modeled using a symmetric four strip model; simple supports were assumed at both the loaded and unloaded edges. Along the unloaded edges, the transverse displacement (v) was un-restrained. The first eight longitudinal terms were used to approximate the u, v, and w displacement fields ($k = m = n = 1, 2, 3, ..., 8$), and an imperfection field in the general shape of the critical buckling mode with a maximum amplitude of 2.5% of the panel thickness was assumed to be present.

In Figures 4.14 through 4.16, the normalized `NLISA` results are compared to the normalized experimental results reported in [64]. The `NLISA` data is normalized by the critical buckling load, strain, and displacement values estimated using the `NLISA` results. The experimental results (which are taken from [64]) were normalized by the critical buckling load, strain, and displacement values obtained from the finite element analysis described in [64]. The critical buckling load predicted by the `NLISA` analysis is $P_{cr} \approx 9500$ lb, and the critical buckling load obtained from the finite element analysis is $P_{cr} \approx 10{,}100$ lb. The difference between the finite element and `NLISA` buckling load predictions ($\approx$ 6%) is caused by the boundary conditions at the longitudinal ends of the panel. In Figures 4.15 and 4.16, displacement and strain data obtained at the points of maximum displacement are plotted. The points of maximum displacement for the `NLISA` results are located at the 1/4 and 3/4 points along the panel length. The location of the points of maximum displacement for the experimental results is not stated in [63], but are likely displaced slightly towards the center of the panel (again, because of the longitudinal boundary conditions).

Despite the difference in longitudinal boundary conditions, both the full and reduced `NLISA` analyses appear to yield a good approximation to the panel's response. Both the normalized load-end shortening response (Figure 4.14) and the normalized maximum displacement plot (Figure 4.15) are in excellent agreement with the normalized experimental results. The predicted strains on the tensile side of the panel agree well with the normalized experimental results over the entire loading range. On the compressive side of the panel, the axial strain results agree well with the normalized experimental results up to P/P_{cr}=1.5, at which point the predicted strains diverge from the experimental strains (the magnitudes of the `NLISA` strains are too low). The disagreement on the compressive side of the panel may be a result of shear deformation effects – the NLISA analyses utilize classical plate theory and do not account for transverse shear deformation.

Both the full and reduced NLISA results were obtained in approximately 10s using an IBM RS/6000 model 390 computer. The reduced solution was obtained with two re-computations of the basis vectors ($\hat{e}$=0.060); this occurred at P/P_{cr}=1.05, and P/P_{cr}=1.65, and these points are marked with a filled circle in Figure 4.14 The numbers in square brackets indicate the number of basis vectors generated at each of these points.

4.3 Blade Stiffened Panel

In this section, results for a three-bay blade stiffened panel are presented. A sketch of the panel is shown in Figure 4.17. The panel is 30.0 in long and 24.0 in wide, with four evenly spaced blade stiffeners, each of which are almost three times the thickness of the skin. Material properties are those of aluminum: E=10e7 lb/in^2 and ν=0.30.

The panel was analyzed using the STAGSC-1 finite element computer code [65, 66] in [67], where it was assumed to be clamped at the loaded edges and simply-supported at the side edges. Uniform end-shortening was imposed. As reported in [67], the panel skin initially buckles into five half-waves in the longitudinal direction, and maintains this overall deformation pattern up to approximately five times the critical buckling load. Beyond this point, the number of axial waves in the panel does not change, but the magnitude of the inward and outward wavelength displacements becomes non-uniform.

The analysis (and eventually the design) of this type of structure was the primary motivation for developing the present capability. As such, this problem is the primary testbed for assessing the relative computational efficiencies of the full and reduced solution methods. In the following sections, both full and reduced NLISA results are compared to these STAGSC-1 results. Although the NLISA analyses assume that the longitudinal ends of each strip are simply supported, the boundary conditions modeled at the longitudinal ends of the assem-

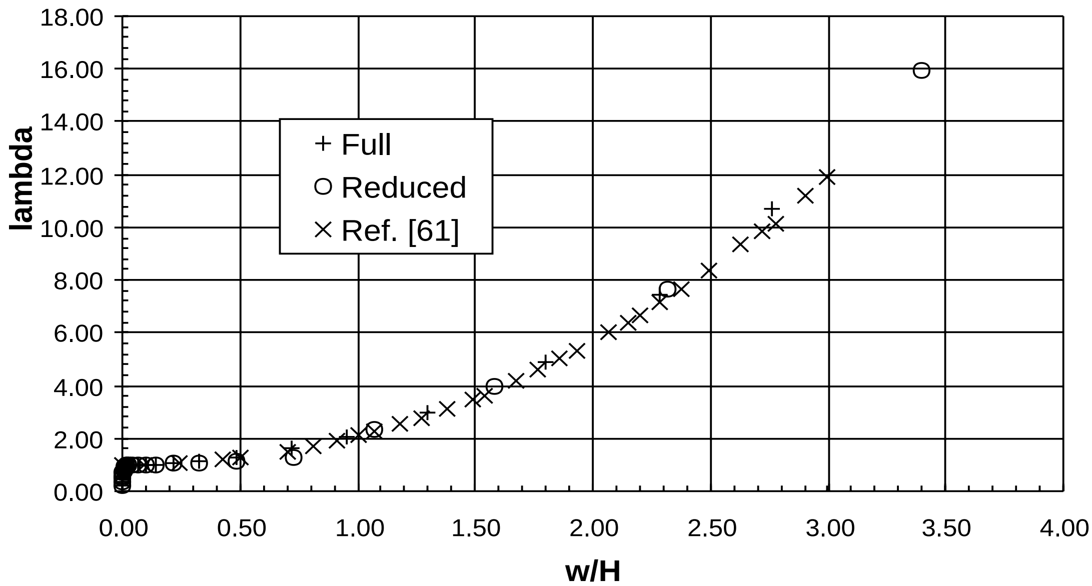

Figure 4.13: Example 6 – w/H vs. end shortening
8 strips; $k = 2, 4, 6, ..., 10$; $m = n = 1, 3, 5, ..., 9$

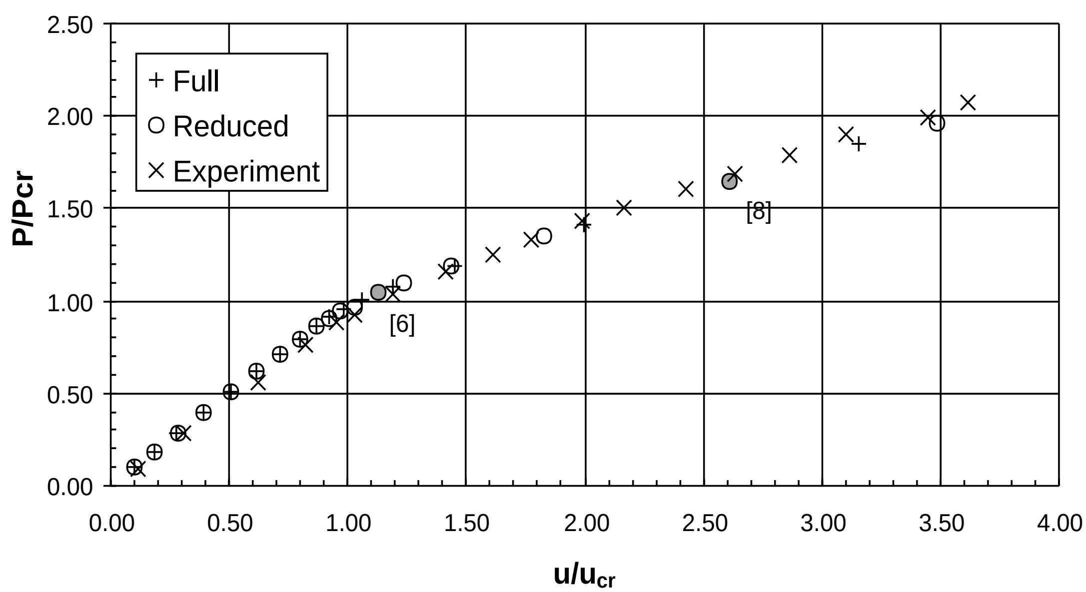

Figure 4.14: Example 7 – P/P_{cr} vs. end shortening
4 strips; $k = m = n = 1, 2, 3, ..., 8$

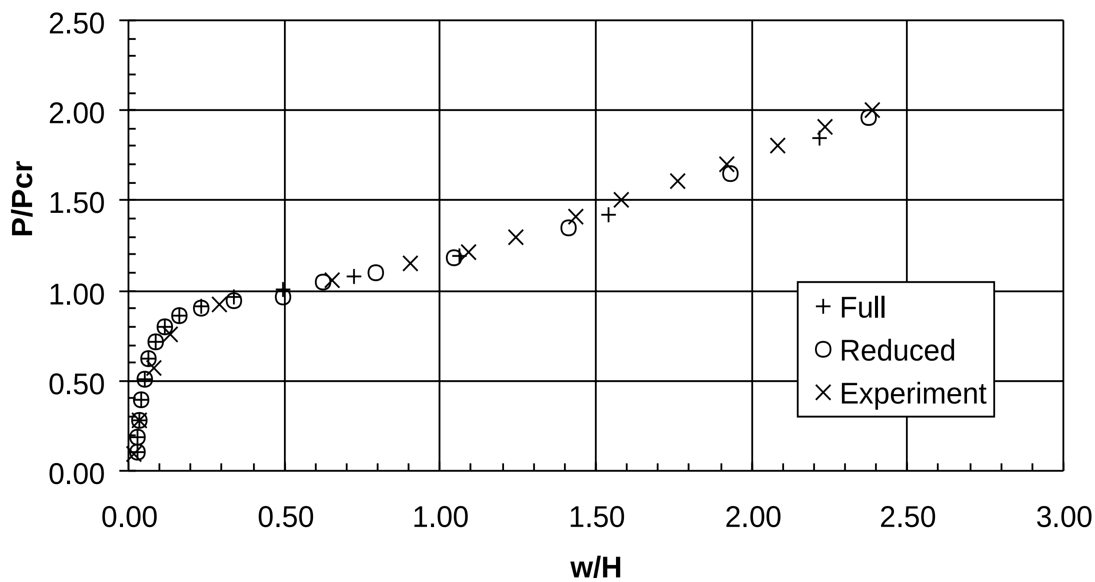

Figure 4.15: Example 7 – P/P_{cr} vs. w/H at point of max deflection
4 strips; $k = m = n = 1, 2, 3, ..., 8$

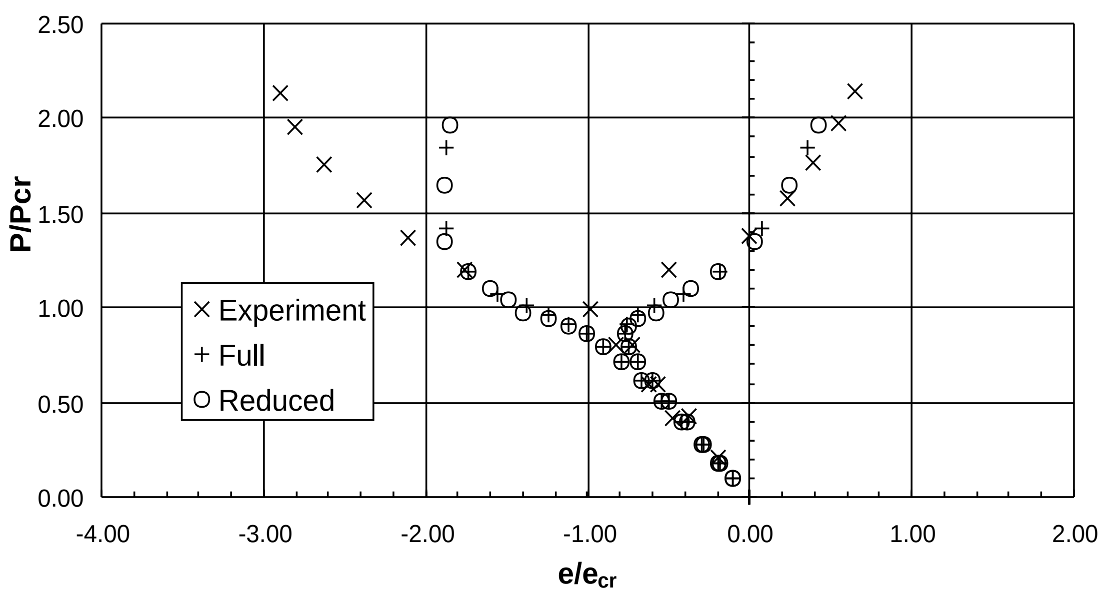

Figure 4.16: Example 7 – P/P_{cr} vs. axial strain at point of max deflection
4 strips; $k = m = n = 1, 2, 3, ..., 8$

bled structure in this case are essentially clamped boundary conditions (the same boundary conditions used in the finite element analysis). This is because the u displacement along the edge of each stiffener at the longitudinal ends is restrained to be a constant value (the value of the end-shortening). Thus, no rotation of the stiffener in the x-z plane is permitted at the loaded ends.

4.3.1 Symmetric Panel Representation

Results obtained using a half-panel (symmetric) representation of the panel are presented in this section. The boundary conditions at the transverse ends of the panel are free:

$$N_{xy} = N_y = 2\frac{\partial M_{xy}}{\partial y} + \frac{\partial M_y}{\partial y} = M_y = 0 \tag{4.3}$$

and symmetry conditions are imposed at the mid-line:

$$N_{xy} + N_y\frac{\partial u}{\partial y} = v = 2\frac{\partial M_{xy}}{\partial y} + \frac{\partial M_y}{\partial y} + N_{xy}\frac{\partial w}{\partial x} + N_y\frac{\partial w}{\partial y} = \frac{\partial w}{\partial y} = 0. \tag{4.4}$$

Model 1

The first set of results was obtained with a fourteen strip model in which the panel skin is modeled using twelve finite strips, and each of the two blade stiffeners is modeled using a single strip. In agreement with the `STAGSC-1` analysis, the `NLISA` analyses predict buckling near 336 *lb/in* in five half-waves in the longitudinal direction, and in a single transverse half-wave in each bay (see Figure 4.18). The results shown in Figures 4.19 through 4.22 were obtained using the first eleven even longitudinal series terms for the u displacement component ($k = 2, 4, 6, ..., 22$), and the first eleven odd longitudinal series terms for the v and w displacement components ($m = n = 1, 3, 5, ..., 21$). An imperfection field $sin(5\pi x/L)$ with a maximum amplitude of 0.0001 *in* (0.167% of the skin thickness) was included in the analysis. In the figures, the plus shaped markers represent the full `NLISA` results, the circular markers represent the reduced `NLISA` results, and the "x" shaped markers represent the STAGSC-1 results. In each plot, the end load was normalized by the critical end load reported in [67], P_{cr}=336.0 lb/in.

In these figures, results are presented up to an end load corresponding to 5.0 times P_{cr}. As reported in [67], STAGS1-C has difficulty converging at an axial load slightly higher than this, and further progress can only be made with the use of the "Thurston Processor" [68]. The Thurston Processor is an algorithm built into STAGSC-1 which mitigates difficulties encountered when attempting to obtain non-linear solutions in the vicinity of bifurcation points. As this capability is not built into the NLISA solver, accurate results beyond P/P_{cr}=5.0 cannot be reliably obtained with NLISA.

The end load vs. end shortening behavior of the structure is plotted in Figure 4.19. Agreement between the NLISA predictions and the STAGSC-1 analysis is satisfactory, with the NLISA analyses slightly under predicting the panel stiffness at higher load levels. The w displacement and axial strain at the center of the panel (point "1" in Figure 4.17) are plotted against the normalized end load, P/P_{cr}, in Figures 4.20 and 4.21, respectively. The w displacement is in good agreement with the finite element results, while the axial strains are somewhat under predicted (especially on the tensile side of the panel, where the deviation is as much as 35%). In Figure 4.22, the transverse (ϵ_y) surface strains adjacent to a stiffener (point "2" in Figure 4.17) are plotted against the normalized end load. The NLISA transverse strain predictions are generally in good agreement with the STAGSC-1 results; above $P/P_{cr} = 2.5$, there is a deviation on the compressive side of the panel.

During the execution of this problem, it was discovered that the relative computational efficiencies of the full and reduced solution methods were hardware dependent. For this example and those to follow, therefore, NLISA results were obtained using two different SP2 nodes (computers). The first node (hereafter referred to as NODE1) is an IBM RS/6000 model 590 computer with 512MB of RAM. The second node (hereafter referred to as NODE2) is an IBM RS/6000 model 390 computer with 256MB of RAM. For the present problem, the full NLISA solution was obtained in 1228s on NODE1 and in 2572s on NODE2. With the

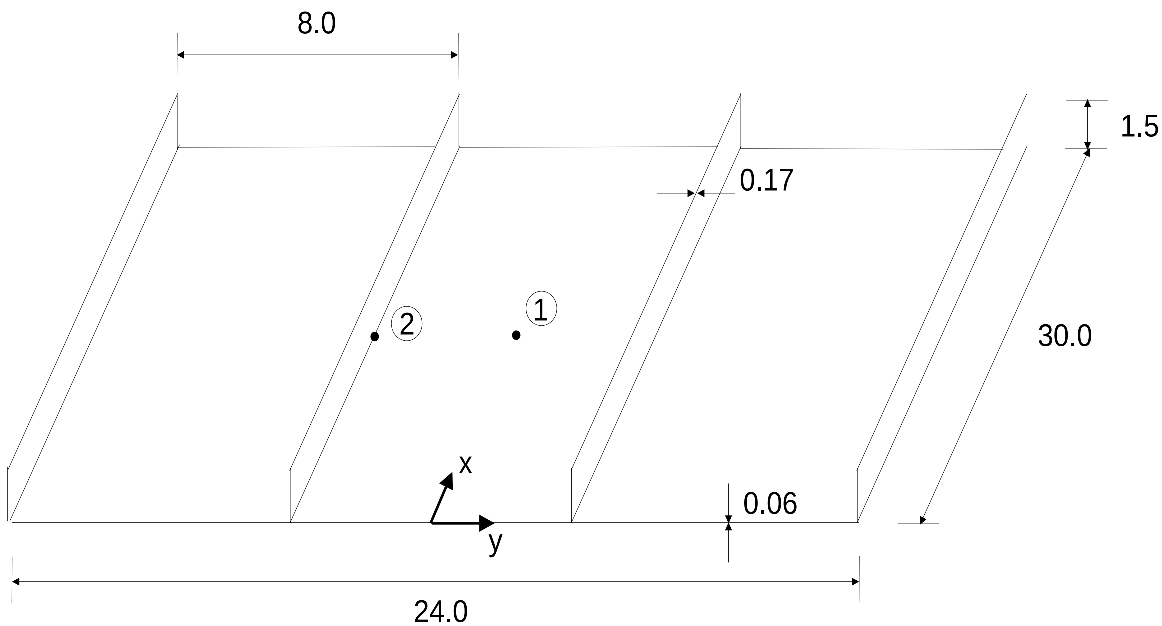

Figure 4.17: Blade Stiffened Panel

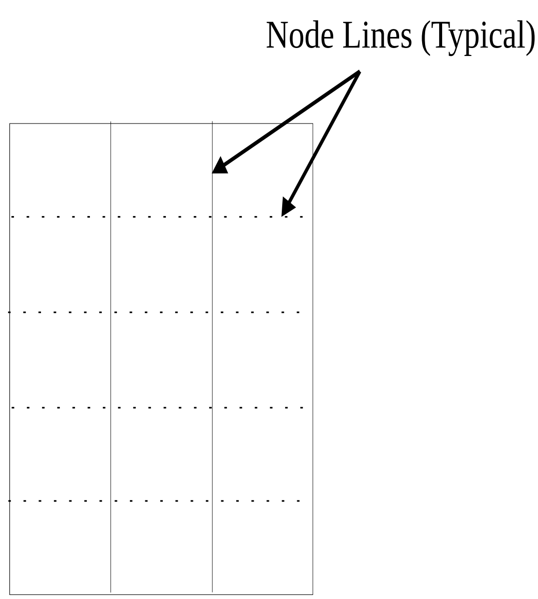

Figure 4.18: Buckling Mode Shape (planform view)

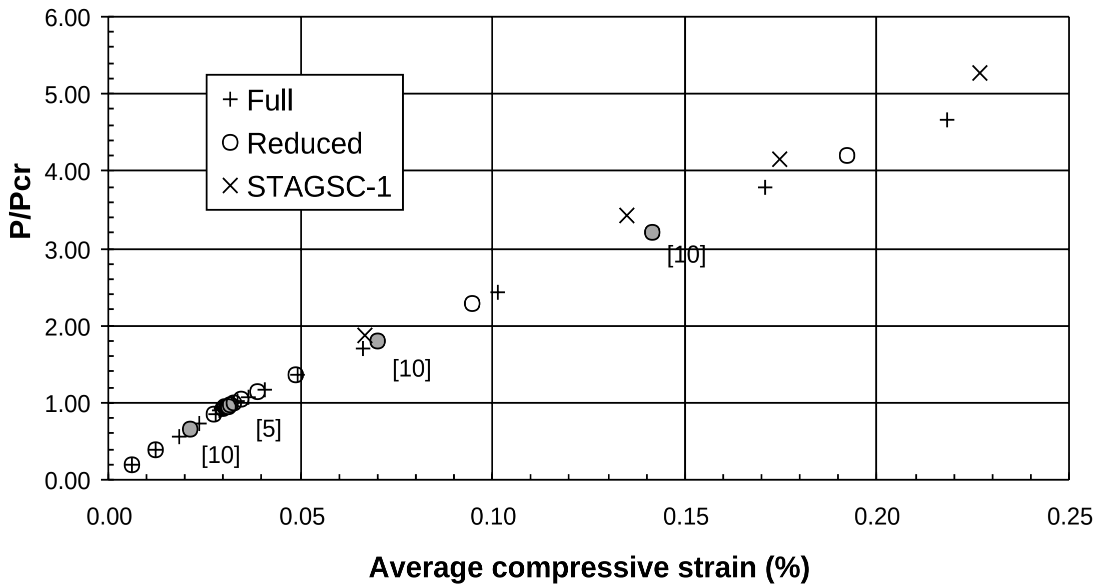

Figure 4.19: Symmetric Model 1 – P/P_{cr} vs. Average Compressive Strain (%)
14 strips; $k = 2, 4, 6, ..., 22$; $m = n = 1, 3, 5, ..., 21$

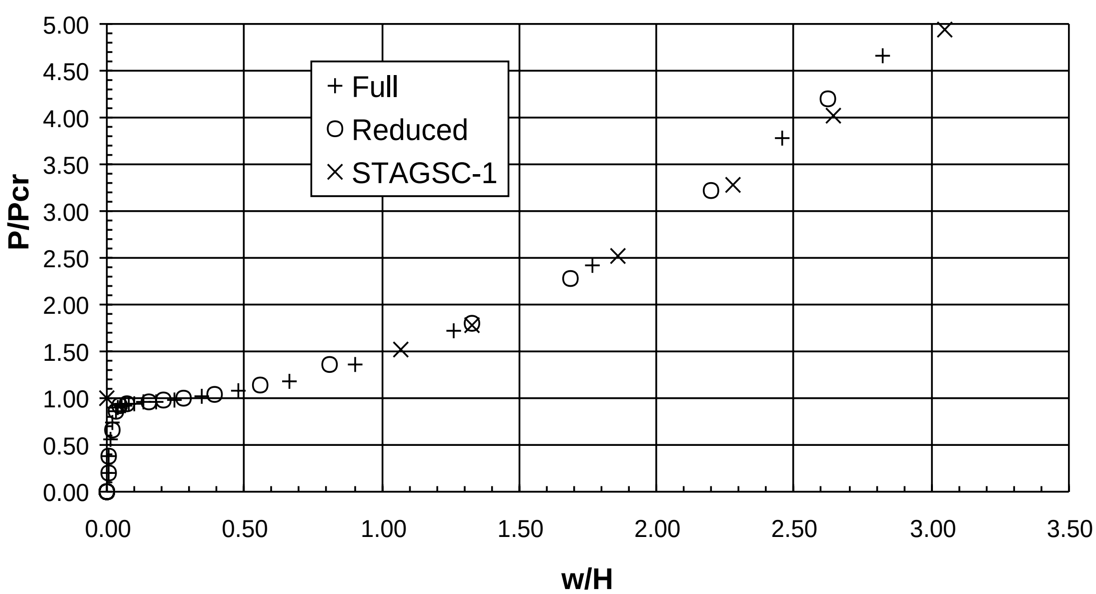

Figure 4.20: Symmetric Model 1 – P/P_{cr} vs. w/H at location (1)
14 strips; $k = 2, 4, 6, ..., 22$; $m = n = 1, 3, 5, ..., 21$

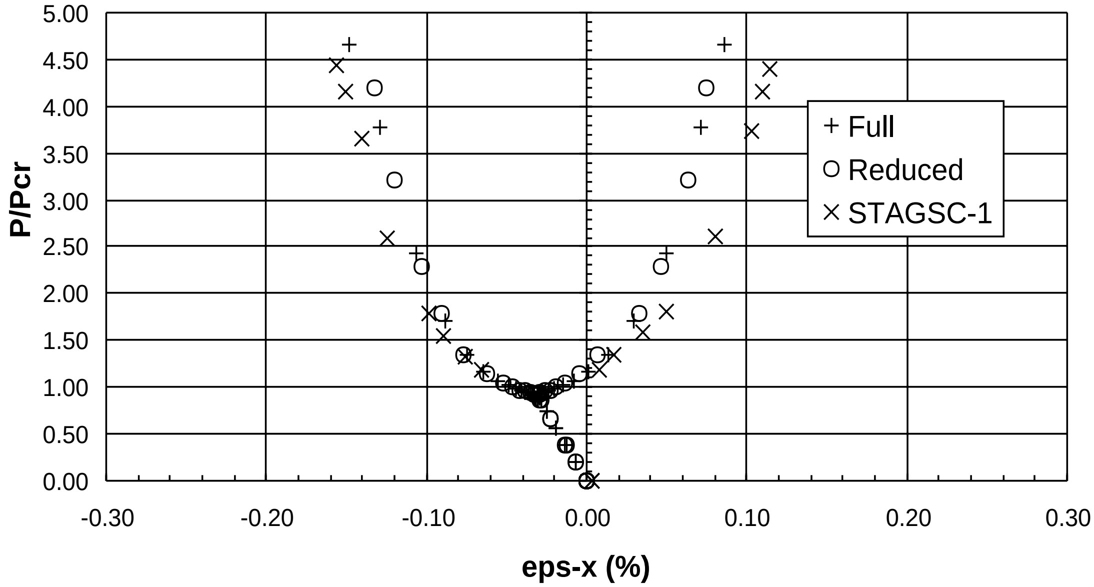

Figure 4.21: Symmetric Model 1 – P/P_{cr} vs. ϵ_x at location (1)
14 strips $k = 2, 4, 6, ..., 22$; $m = n = 1, 3, 5, ..., 21$

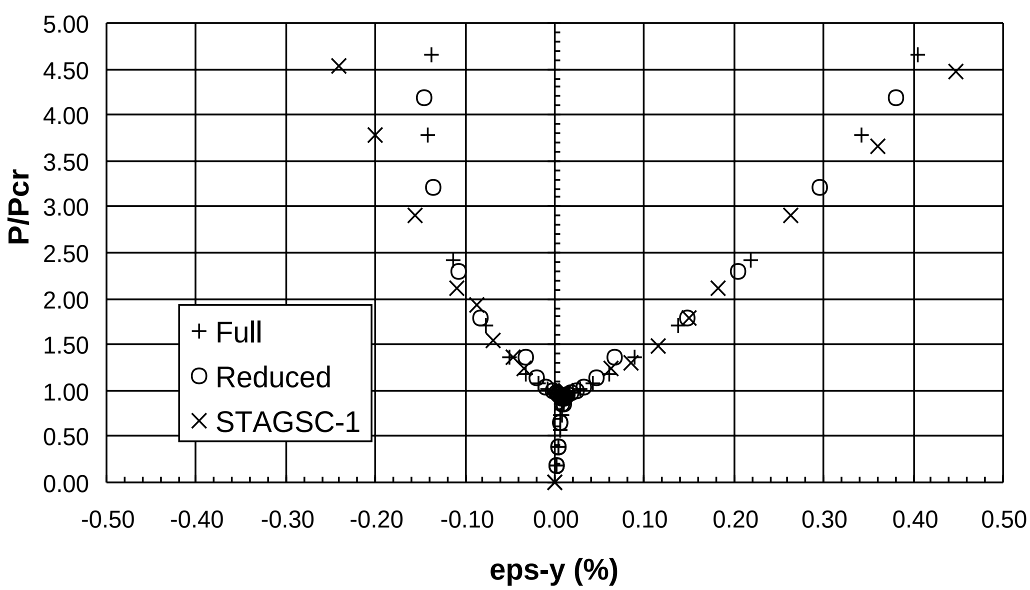

Figure 4.22: Symmetric Model 1 – P/P_{cr} vs. ϵ_y at location (2)
14 strips; $k = 2, 4, 6, ..., 22$; $m = n = 1, 3, 5, ..., 21$

user specified error tolerance, $\hat{e}$ set to a value of 0.010, the reduced solution was obtained in 960s on NODE1 (22% reduction in computational cost) and in 1615s on NODE2 (37% reduction in computational cost). During the reduced solution procedure, new sets of basis vectors were computed a total of four times (points at which new basis vectors were computed are marked with filled circles in Figure 4.19). The numbers in square brackets indicate the number of basis vectors generated at each of these points.

Model 2

The computational cost of both the full and reduced `NLISA` analyses can be significantly lowered by reducing the number of longitudinal terms used to represent the non-linear displacement fields. For example, the results shown in Figure 4.23 through 4.26 were obtained using roughly half the terms as were used in the previous solution. Longitudinal series terms corresponding to $(k = 2, 6, 10, 14, 18, 22)$ were used for the u displacement component and longitudinal series terms corresponding to $(m = n = 1, 5, 9, 13, 17, 21)$ were used for the v and w displacement components.

As with model 1, agreement with the `STAGSC-1` results is generally good. The w displacement results (Figure 4.24) are degraded at higher load levels, but the strain results (Figures 4.25 and 4.26) are actually improved. There is no obvious reason why the strain results should improve with the removal of longitudinal terms, and this result is likely a coincidence of canceling errors.

The reduction in longitudinal terms reduced the computational cost of both methods by approximately 85%. On NODE1, the full solution was obtained in 177s, and the reduced solution was obtained in 128s (a computational savings of 28%). On NODE2, the full solution was obtained in 364s, and the reduced solution was obtained in 194s, (a computational savings of 46%). During the reduced solution procedure, new sets of basis vectors were re-generated three times (these points are marked as filled circles in Figure 4.23) when the error tolerance, $\hat{e}$ was set to a value of 0.018.

Model 3

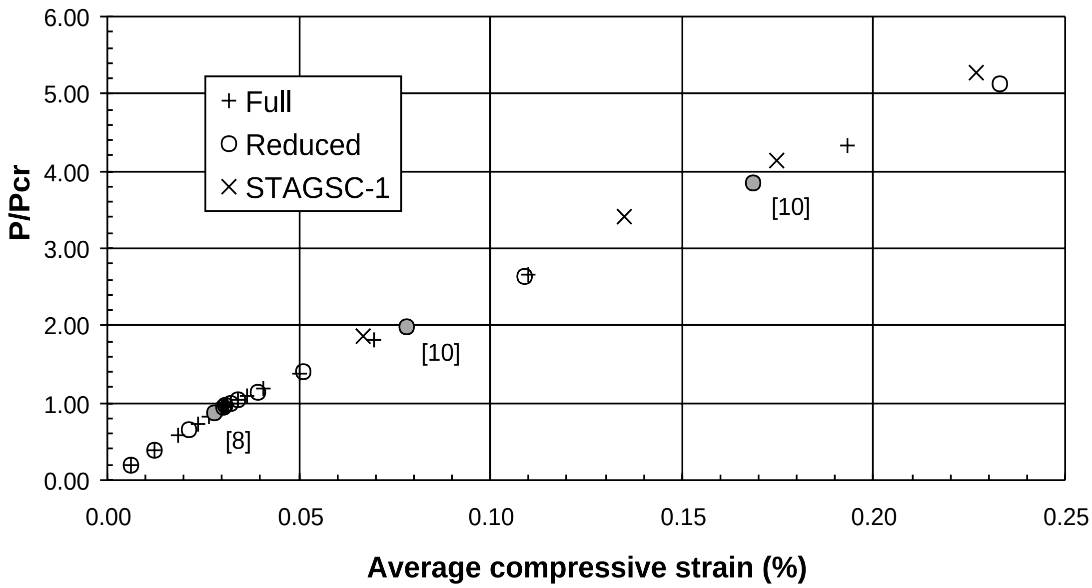

Figure 4.23: Symmetric Model 2 – P/P_{cr} vs. Average Compressive Load (%)
14 strips; $k = 2, 6, 10, 14, 18, 22$; $m = n = 1, 5, 9, 13, 17, 21$

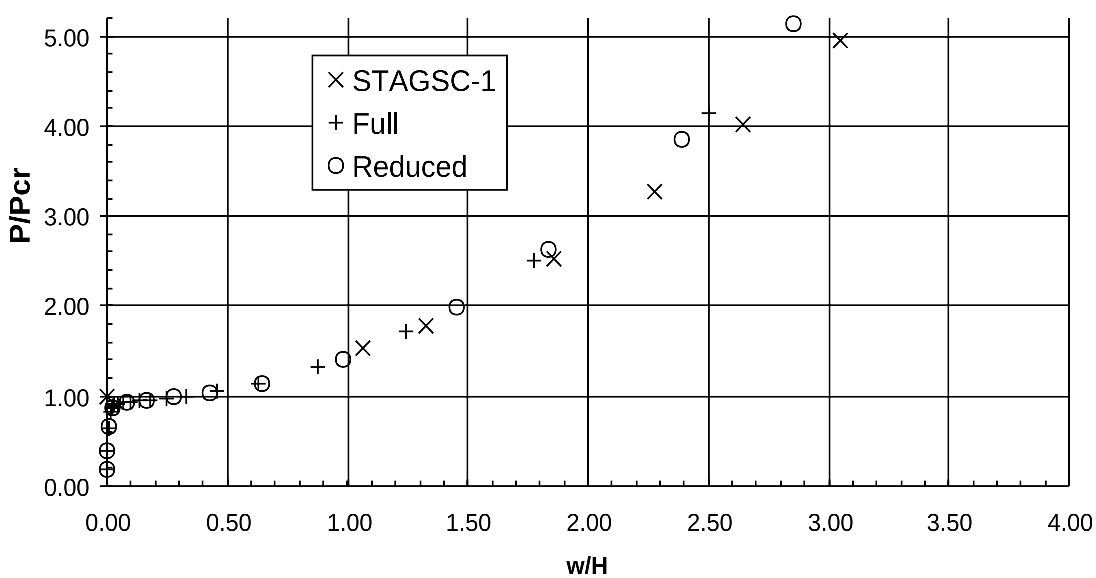

Figure 4.24: Symmetric Model 2 – P/P_{cr} vs. w/H at location (1)
14 strips; $k = 2, 6, 10, 14, 18, 22$; $m = n = 1, 5, 9, 13, 17, 21$

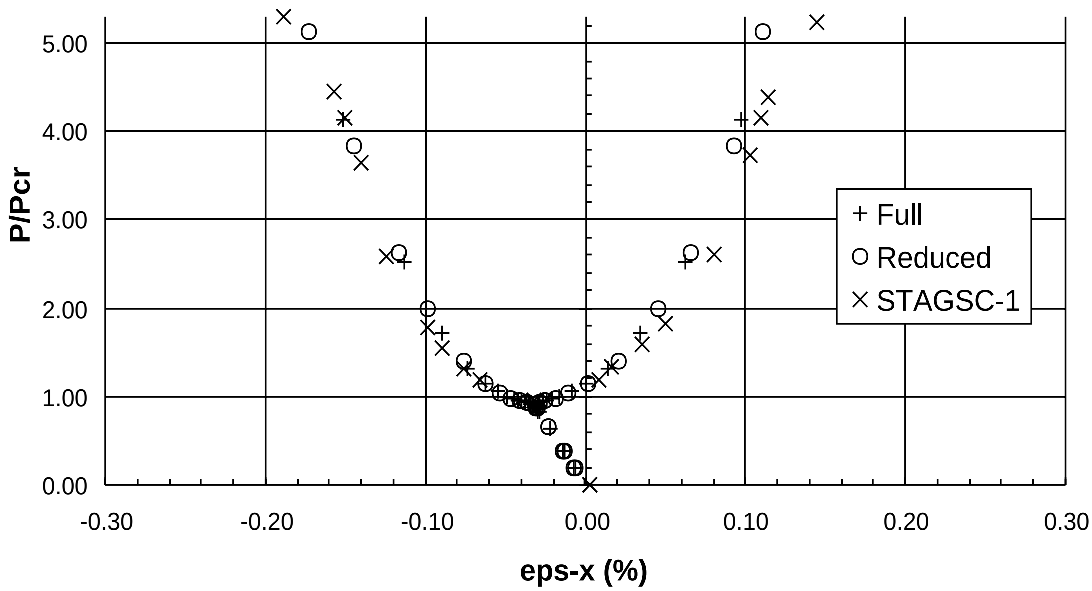

Figure 4.25: Symmetric Model 2 – P/P_{cr} vs. ϵ_x at location (1)
14 strips; $k = 2, 6, 10, 14, 18, 22$; $m = n = 1, 5, 9, 13, 17, 21$

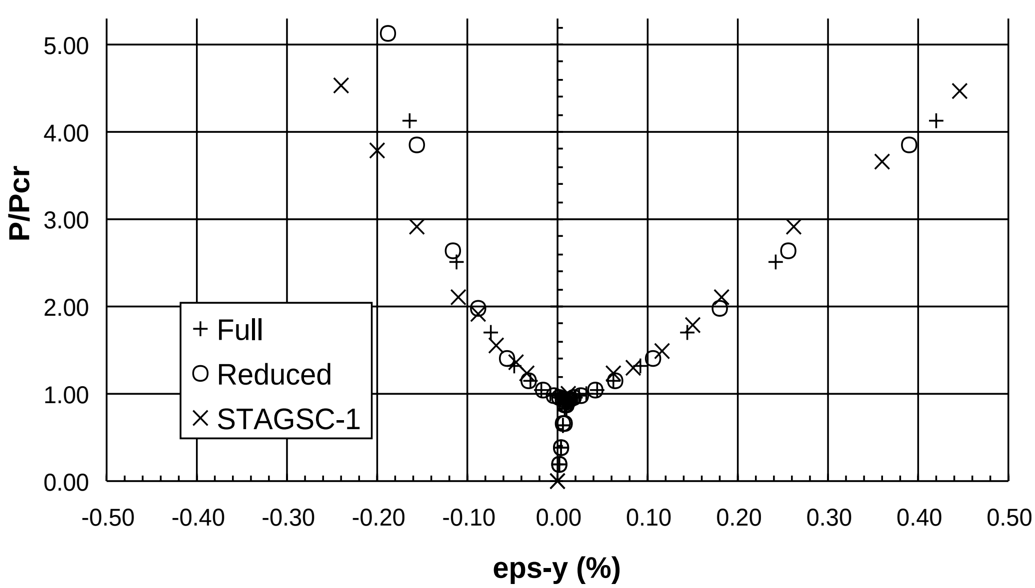

Figure 4.26: Symmetric Model 2 – P/P_{cr} vs. ϵ_y at location (2)
14 strips; $k = 2, 6, 10, 14, 18, 22$; $m = n = 1, 5, 9, 13, 17, 21$

In order to document the effects of further increasing the number of finite strips on the accuracy and efficiency of the `NLISA` solution procedures, an additional analysis using the symmetric panel representation was performed. Here, a model comprised of 26 finite strips was used (this corresponds to twice the level of discretization in the panel skin that was used in the previous analyses). The results shown in Figure 4.27 through 4.30 were obtained using the same smaller set of longitudinal series terms that were used for model 2. Overall, the results agree favorably with `STAGSC-1`, and are slightly improved (Figures 4.28 and 4.30) compared to those obtained with model 2.

On NODE1, the full solution was obtained in $652s$, and the reduced solution was obtained in $340s$ (a difference of 48%). On NODE2, the full solution was obtained in $1487s$, and the reduced solution was obtained in $621s$, (a difference of 58%). The reduced solution was obtained using an error tolerance of 0.010, and was obtained with two re-computations of the basis vectors. Further discussion of the relative efficiencies of the full and reduced solution procedures may be found in section 4.4.

4.3.2 Stiffener-Unit Representation

In this section, `NLISA` results obtained using a "stiffener-unit" representation of the panel are presented. The panel is modeled using a single repeating element of the structure, comprised of a single stiffener and the adjacent skin. The stiffener unit is illustrated in Figure 4.31. The stiffener-unit representation for the panel allows the structure to be modeled (approximately) with a minimum number of finite strips, and will result in computational savings as compared to a full panel representation (see section 4.3.1). Because of its computational efficiency, future design studies may initially employ a configuration of this type. The `NLISA` model consists of nine finite strips; eight strips make up the skin, and one strip represents the blade stiffener. This is the same level of discretization as was used for models 1 and 2 above. The following boundary conditions were imposed at both side edges:

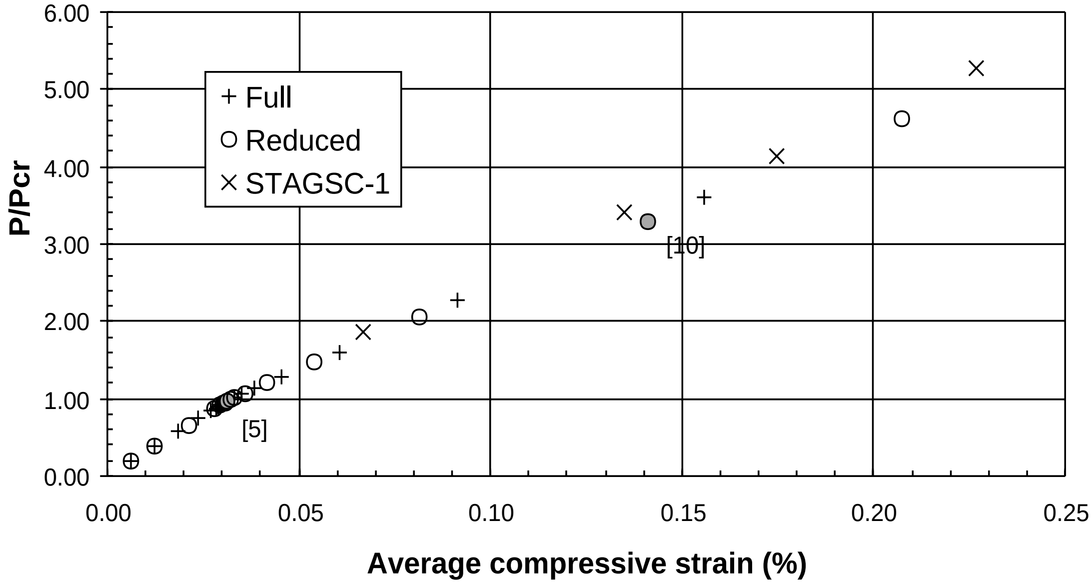

Figure 4.27: Symmetric Model 3 – P/P_{cr} vs. Average Compressive Load (%)
28 strips; $k = 2, 6, 10, 14, 18, 22$; $m = n = 1, 5, 9, 13, 17, 21$

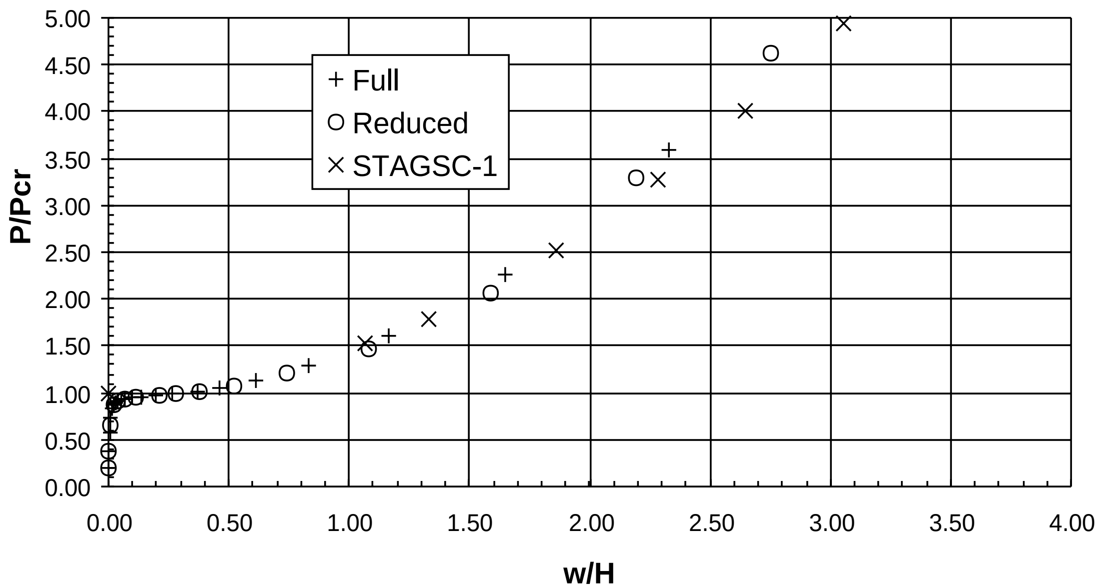

Figure 4.28: Symmetric Model 3 – P/P_{cr} vs. w/H at location (1)
28 strips; $k = 2, 6, 10, 14, 18, 22$; $m = n = 1, 5, 9, 13, 17, 21$

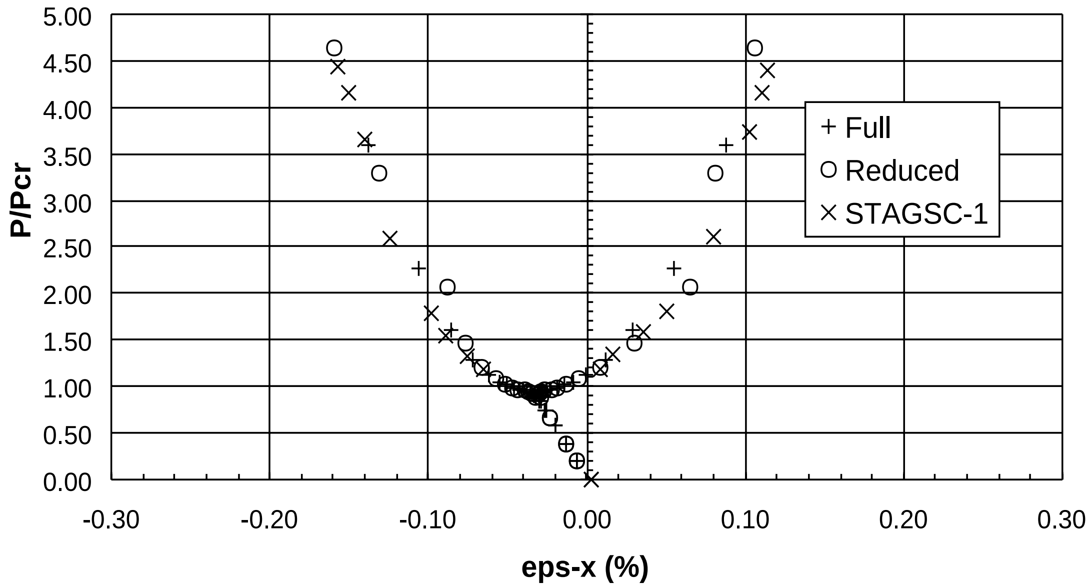

Figure 4.29: Symmetric Model 3 – P/P_{cr} vs. ϵ_x at location (1)
28 strips; $k = 2, 6, 10, 14, 18, 22$; $m = n = 1, 5, 9, 13, 17, 21$

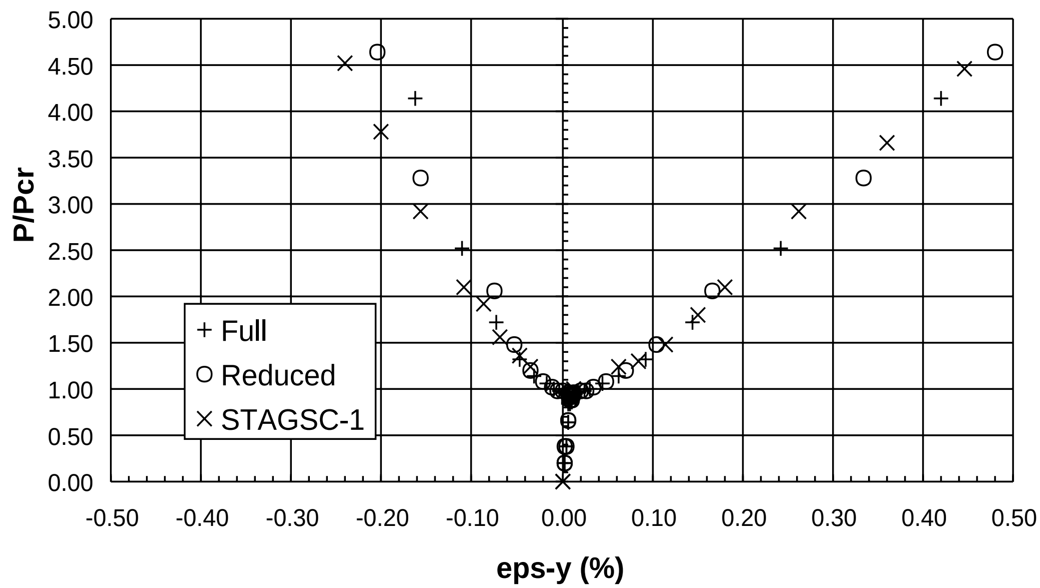

Figure 4.30: Symmetric Model 3 – P/P_{cr} vs. ϵ_y at location (2)
28 strips; $k = 2, 6, 10, 14, 18, 22$; $m = n = 1, 5, 9, 13, 17, 21$

$$N_{xy} = N_y = 2\frac{\partial M_{xy}}{\partial y} + \frac{\partial M_y}{\partial y} = \frac{\partial w}{\partial y} = 0. \tag{4.5}$$

and uniform end shortening was imposed at the longitudinal edges. Except for the v displacement component, which was left free to expand in-plane, these boundary conditions correspond to the symmetry condition.

The end load, P, for an `NLISA` stiffener unit is defined as the total load carried by the stiffener unit divided by its width (8.0 *in*). In order to accurately compare the stiffener unit results to those obtained with the complete panel, this end load must be area-adjusted. Although three stiffener units, when placed side by side, have the same total width as the complete panel, the total cross-sectional area is different. This is because three adjacent stiffener units have a total of three stiffeners, whereas the complete panel contains four stiffeners. The area-adjusted end load for the stiffener unit is defined as follows:

$$P^* = \frac{A_{tot}}{3A_u}P = 1.116P \tag{4.6}$$

where A_{tot} is the total cross-sectional area of the complete panel and A_u is the area of a stiffener unit.

Model 4

The results shown in Figure 4.32 through 4.35 were obtained using the first seven even longitudinal series terms for the u displacement component $(2, 4, 6, ..., 14)$ and the first eight odd longitudinal series terms for the v and w displacement components $(m = n = 1, 3, 5, ..., 15)$. An imperfection field $(sin(5\pi x/L))$ with a maximum amplitude of 0.0001 *in* (0.167% of the skin thickness) was included in the analysis. The plus shaped markers represent the full `NLISA` results, the circular markers represent the reduced `NLISA` results, and the "x" shaped markers represent the `STAGSC-1` results. In each case, the area adjusted end load was normalized by the critical end load reported in [67], P_{cr}=336.0 *lb/in*.

Overall, agreement between the `NLISA` stiffener-unit predictions and the `STAGSC-1` results is

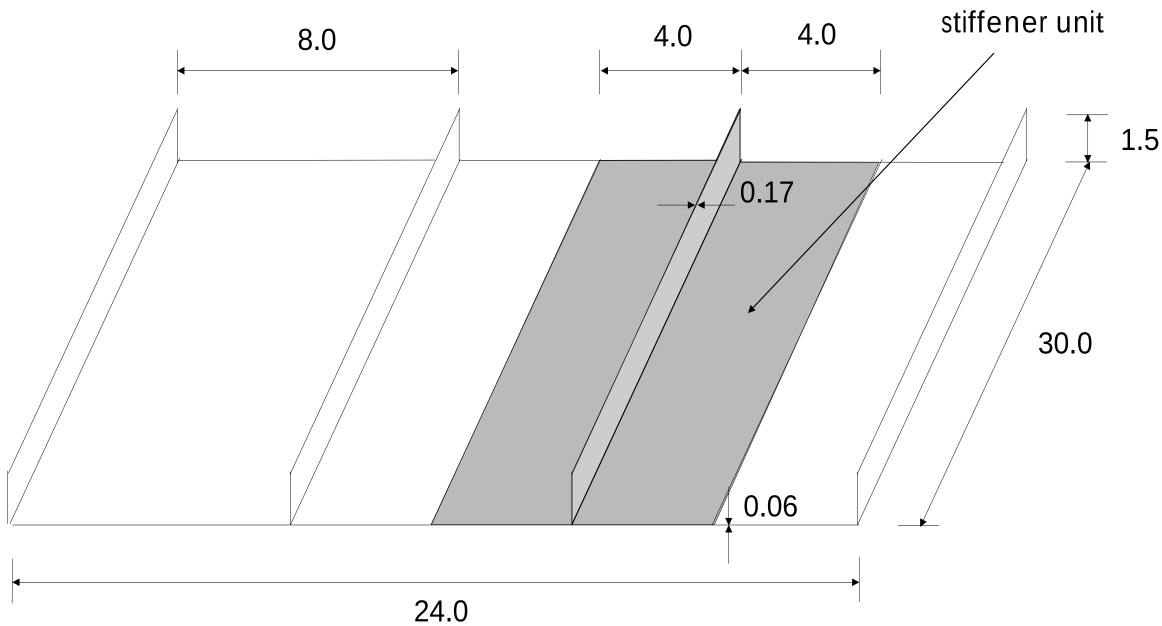

Figure 4.31: Stiffener-Unit Representation

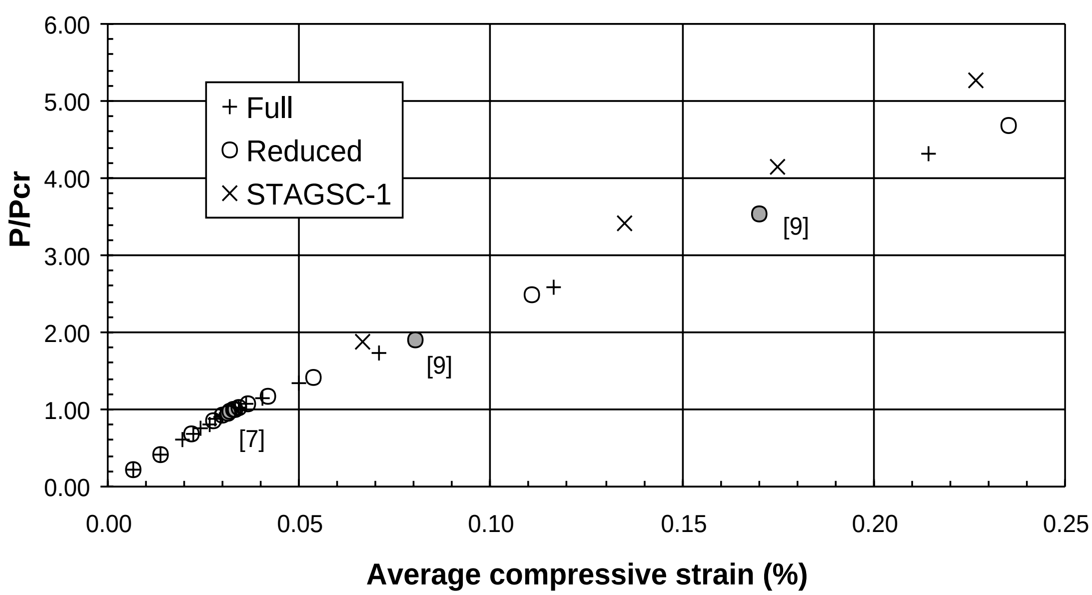

Figure 4.32: Stiffener Unit Model 1 – P^*/P_{cr} vs. Average Compressive Strain (%)
$k = 2, 4, 6, 8, 10, 12, 14$; $m = n = 1, 3, 5, 7, 9, 11, 13, 15$

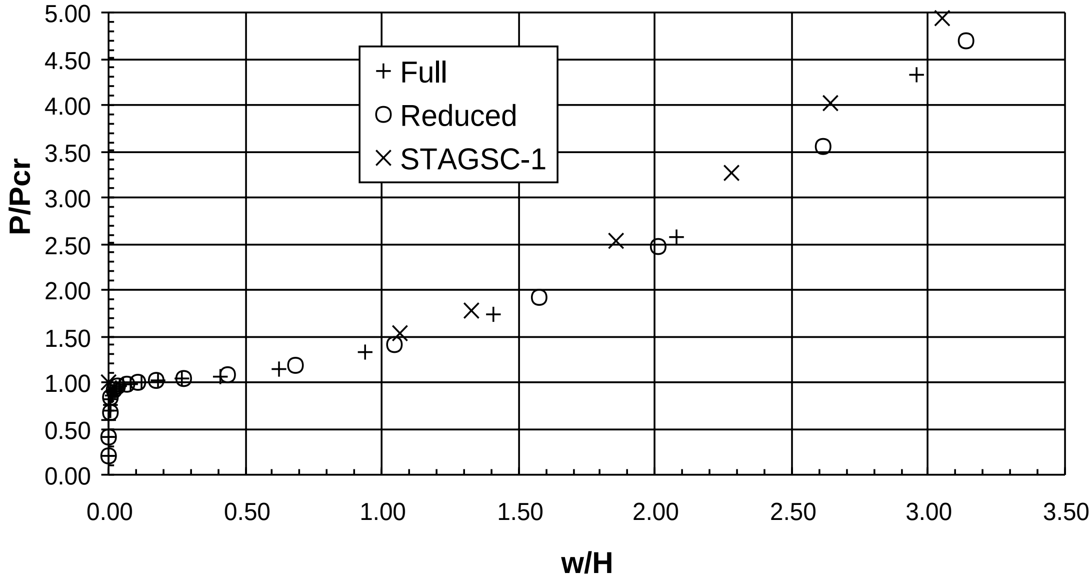

Figure 4.33: Stiffener Unit Model 1 – P^*/P_{cr} vs. w/H at location (1)
$k = 2, 4, 6, 8, 10, 12, 14$; $m = n = 1, 3, 5, 7, 9, 11, 13, 15$

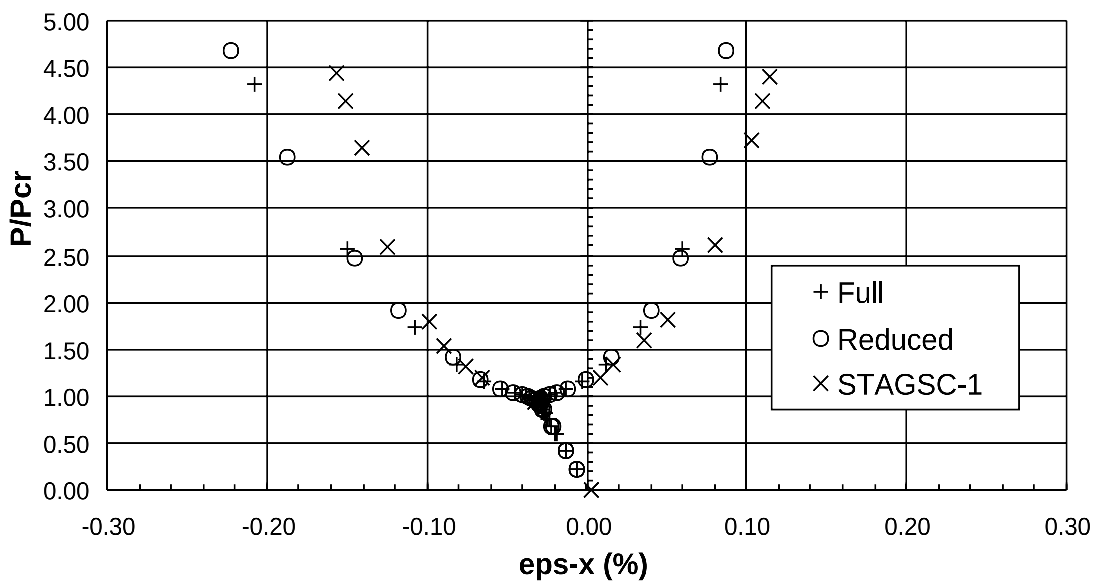

Figure 4.34: Stiffener Unit Model 1 – P^*/P_{cr} vs. ϵ_x at location (1)
$k = 2, 4, 6, 8, 10, 12, 14$; $m = n = 1, 3, 5, 7, 9, 11, 13, 15$

acceptable, although degraded in comparison with the symmetric model results. The end load vs. end shortening behavior of the structure is plotted in Figure 4.32. At higher load levels (above $P/P_{cr} \approx 2.0$, the NLISA analyses predict higher compressive strains compared to the finite element results (a softer overall response). In Figure 4.33, the normalized end load, P/P_{cr}, is plotted against the normalized w displacement at the center of the skin (point "1" in Figure 4.31). The NLISA analyses predict a slightly higher out-of-plane displacement compared to both the STAGSC-1 and half model results at this point. This is consistent with the overall softer response shown in the end-shortening plot. In Figure 4.34, the axial (ϵ_x) strain at the center of the panel skin is plotted against the normalized critical load. NLISA under predicts the surface strain on the tensile side of the panel, and over predicts the surface strain on the compressive side of the panel over most of the loading range. In Figure 4.35, the transverse (ϵ_y) strain adjacent to a stiffener (point "2" in Figure 4.31) is plotted against the normalized end load. Agreement between in NLISA and STAGSC-11 results is excellent for this quantity.

The reduced solution method has no efficiency advantage over the full solution method for the blade stiffener representation. In fact, on NODE1, the reduced solution method is actually less efficient than the full solution method: the full solution was obtained in $145s$, and the reduced solution was obtained in $165s$. On NODE2, the full solution was obtained in $245s$, and the reduced solution was obtained in $223s$. The reduced solutions were obtained with the user specified error tolerance, $\hat{e}$, set to a value of 0.024, in which case basis vectors were re-computed three times. Points at which new sets of basis vectors were computed are indicated using filled circular markers in Figure 4.32, and the numbers in square brackets indicate the number of basis vectors generated in each case.

Model 5

As with the symmetric models, stiffener unit solutions were also obtained with different numbers and combinations of longitudinal terms. In Figures 4.36 through 4.39, results that were obtained using a reduced set of longitudinal terms are presented. In this case, the u

displacement field was represented using longitudinal series terms corresponding to k=2,6, and 10, while the v and w displacement fields were represented using longitudinal series terms corresponding to m=n=1,5,9, and 13. The reduced solution was obtained with an error tolerance, $\hat{e}$, of 0.050, and new sets of basis vectors were generated twice.

As with the symmetric models, the reduction in the number of longitudinal series terms dramatically reduced the computational expense of both the full and reduced solution methods; both solutions were obtained in approximately 22s on NODE1 and 30s on NODE2. The accuracy of the displacement and end-shortening results (Figures 4.36 and 4.37) was degraded only marginally compared to model 4, and agreement with the `STAGSC-1` strain results (Figures 4.38 and 4.39) was actually improved. As was the case with models 1 and 2, there is no obvious reason why the accuracy of the strain quantities should increase as longitudinal terms are removed from the analysis. This result is most likely a coincidence of canceling errors.

4.3.3 Effects of Imperfection Shape

The results presented for both the symmetric and the stiffener unit model were obtained with an imperfection field in the shape of five half-waves in the longitudinal direction – the general shape of the critical buckling mode. If the shape of the imperfection field is modified (to correspond to a single half-wave in the longitudinal direction, for example) the results obtained with the `NLISA` analyses remain essentially unchanged. The full solution procedure encounters no difficulty in making the transition from the pre-buckled single half-wave shape to the post-buckled five half-wave shape. The reduced solution procedure, on the other hand, sometimes had difficulty in making this transition. In order to assure that the reduced solution procedure makes a smooth transition between the pre-buckled shape to the post-buckled shape, a new set of basis vectors must be generated in the vicinity of the critical buckling load. An option was added to the `NLISA` solution procedure which allows the user to trigger the generation of new basis vectors at any specified value of the loading

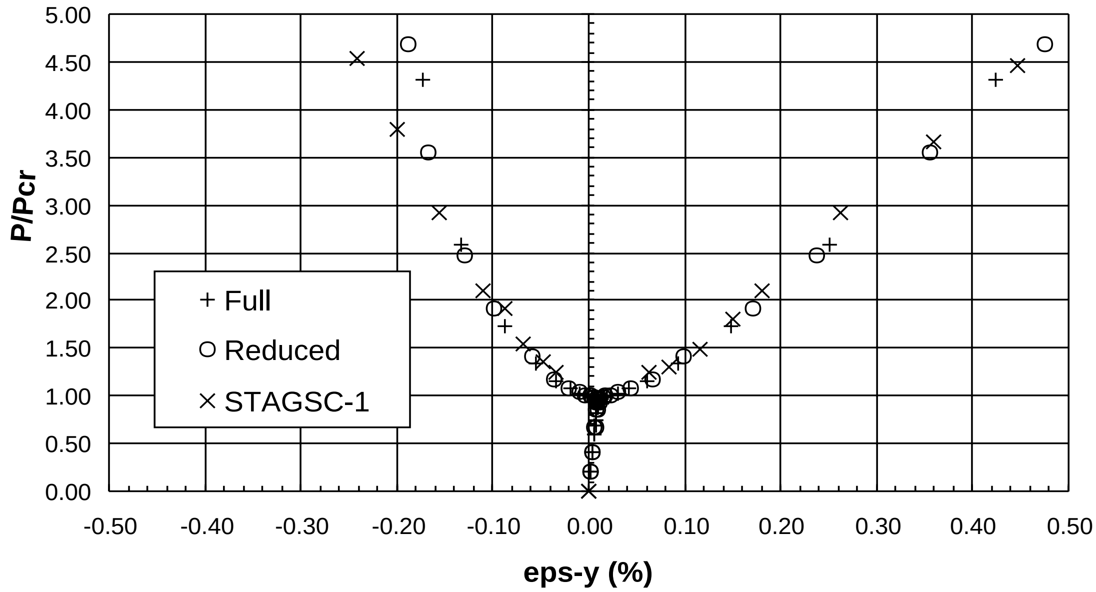

Figure 4.35: Stiffener Unit Model 1 – P^*/P_{cr} vs. ϵ_y at location (2)
$k = 2, 4, 6, 8, 10, 12, 14$; $m = n = 1, 3, 5, 7, 9, 11, 13, 15$

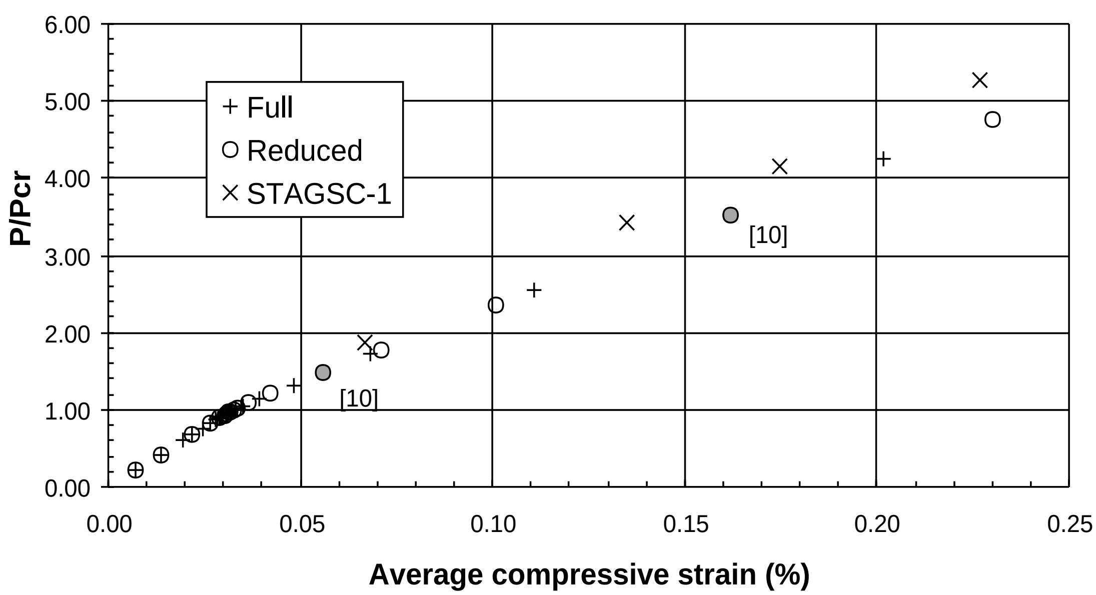

Figure 4.36: Stiffener Unit Model 2 – P^*/P_{cr} vs. Average Compressive Strain (%)
$k = 2, 6, 10$; $m = n = 1, 5, 9, 13$

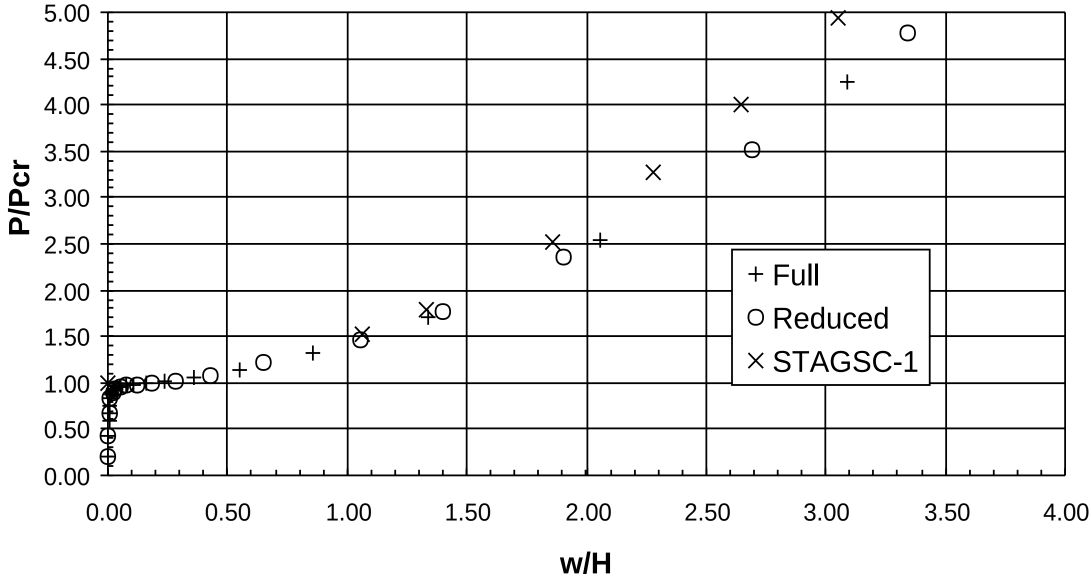

Figure 4.37: Stiffener Unit Model 2 – P^*/P_{cr} vs. w/H at location (1)
$k = 2, 6, 10$; $m = n = 1, 5, 9, 13$

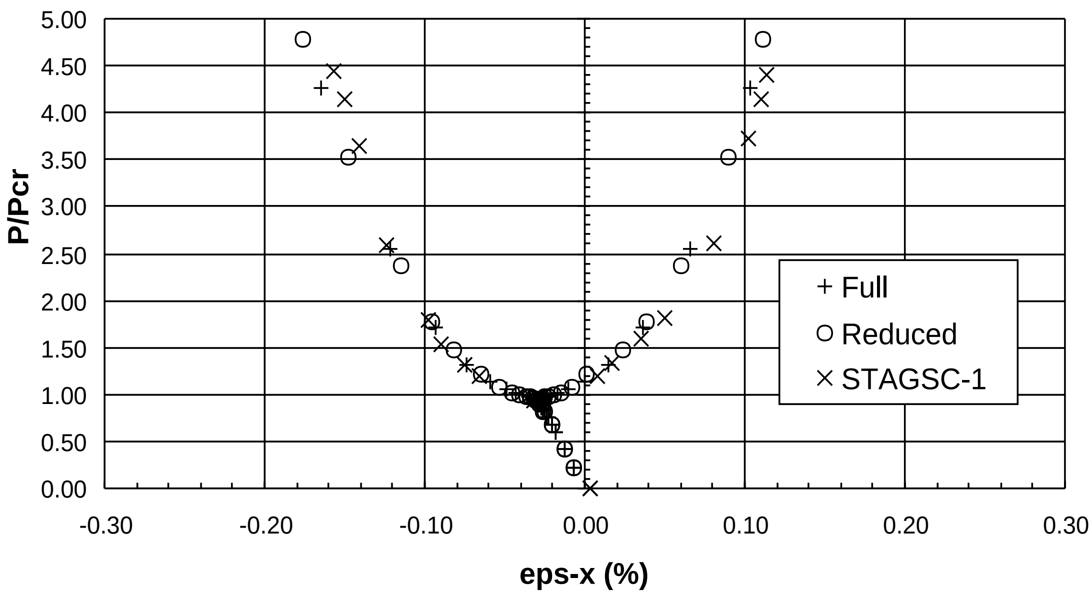

Figure 4.38: Stiffener Unit Model 2 – P^*/P_{cr} vs. ϵ_x at location (1)
$k = 2, 6, 10$; $m = n = 1, 5, 9, 13$

parameter. If the approximate critical buckling load is known, this option can be used to assure that the reduced solution procedure makes the transition into the post-buckled regime more smoothly.

4.4 Computational Efficiency

As previously discussed, the primary motivation behind the present research was to develop and investigate a cost-effective analysis method for evaluating the geometrically non-linear response of structures such as the blade stiffened panel discussed above. In this section, the relative efficiencies of the full and reduced solution procedures are discussed and evaluated in the context of the blade stiffened panel examples. As discussed, results for each case were obtained using two different nodes (computers): NODE1 is an IBM RS/6000 model 590 computer with 512MB of RAM, and NODE2 is an IBM RS/6000 model 390 computer with 256MB of RAM. The `NLISA` computer code, which is written in FORTRAN 90, was compiled with level three (`-O3`) compiler optimization options turned on. During the last year of the present research, considerable effort was expended (code re-write, etc.) in an attempt to make the code run as efficiently as possible.

For any given analysis performed with the full solution method, there are two tasks which take up most of the CPU time: (1) the factorization of the assembled system matrices and (2) the formation of the strip level non-linear stiffness matrices. The reduced solution method can significantly reduce the number of times that the (full) system matrices must be factored, but has no effect on the number of times in which the local stiffness matrices are formed (see Chapter 3). In addition to the above two tasks, the reduced solution method must also periodically generate a new set of basis vectors; this is a smaller but not insignificant computational cost (most of this cost arises from additional forming operations).

As a consequence, the reduced method is most effective in reducing the computational cost of the full method when the most significant portion of the cost of the original (full) problem is matrix factorization. In particular, the ratio, C_f, of the cost of matrix factorization to the cost of matrix formation is a rough indicator of the potential effectiveness of the reduced solution procedure. If this ratio (for the full problem) is large (> 1), the reduction in the cost of factorization will offset the costs of generating basis vectors, and the reduced solution procedure will be effective in reducing the overall computational cost. In general, a larger C_f will lead to larger computational savings. If, on the other hand, C_f (for the full problem) is small (≤ 1), the reduction in factorization costs will be offset by the costs of generating basis vectors, and the reduced method will be as costly (or more costly) compared to the full solution method.

In general, then, we should expect the reduced solution method to be most effective for more complex problems with large numbers of finite strips. As the number of finite strips is increased, the cost of forming the local stiffness matrices increases (roughly) linearly, while the factorization cost of the global stiffness matrix increases at a greater rate. For a given number of finite strips, the addition of more longitudinal terms increases both the cost of global matrix factorization and local matrix formation, and there is no significant effect on C_f. In Table 4.1, the CPU times corresponding to each of the blade stiffened cases is summarized. For each full solution, an approximate value for C_f is indicated; these values were obtained using the IBM AIX profiler utility `gprof`. As noted, C_f stays relatively constant as the number of longitudinal terms are increased, but increases with the number of finite strips.

For a given problem, the relative efficiencies of the full and reduced solution methods depends on the underlying computer hardware. The faster CPU in NODE1 is evidently more effective in reducing the costs of global matrix factorization than it is in reducing the costs of local matrix formation. This is reflected in the lower C_f values in Table 4.1; for a given problem, the NODE1 C_f is roughly half that of the NODE2 C_f. Qualitatively, this makes some sense, as the factorization task is primarily a numerically intensive operation (requiring a large number of floating point operations), while the formation task is more dependent on data manipulation and memory access.

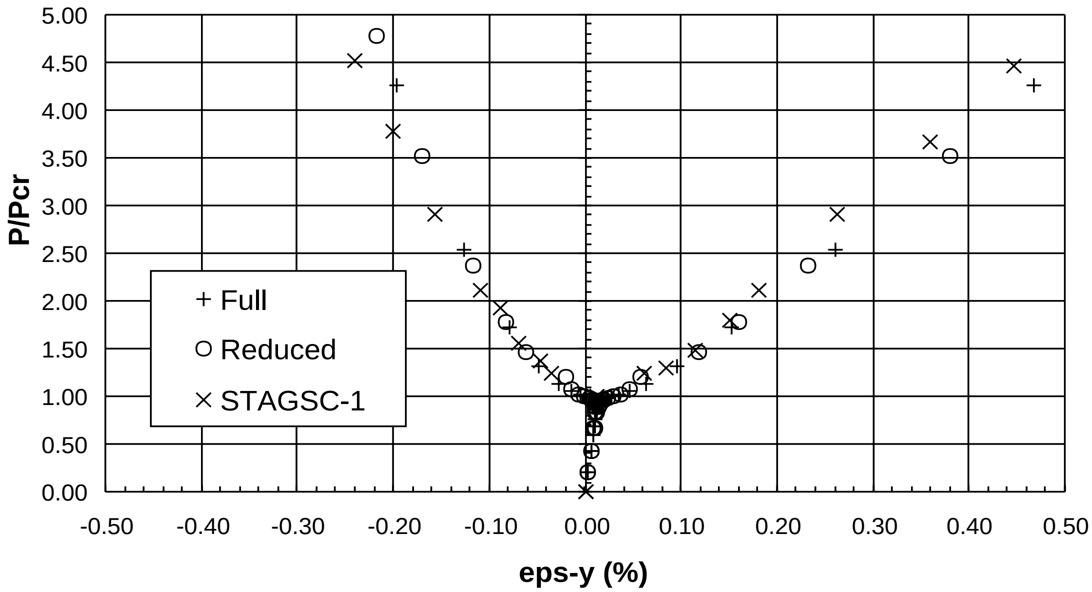

Figure 4.39: Stiffener Unit Model 2 – P^*/P_{cr} vs. ϵ_y at location (2)
$k = 2, 6, 10$; $m = n = 1, 5, 9, 13$

Table 4.1: Summary of CPU Times for Blade Stiffened Panel Example

Model Type	# Strips	Longitudinal Terms	NODE1		NODE2	
			Full	Reduced	Full	Reduced
half panel	14	$k = 2, 4, 6, ..., 22$; $m = n = 1, 3, 5, ..., 21$	$1228s$ $C_f = 1.7$	$960s$ (-22%)	$2572s$ $C_f = 4.0$	$1615s$ (-37%)
half panel	14	$k = 2, 6, 10, ..., 22$; $m = n = 1, 5, 9, ..., 21$	$177s$ $C_f = 1.7$	$128s$ (-28%)	$364s$ $C_f = 3.6$	$198s$ (-46%)
half panel	28	$k = 2, 6, 10, ..., 22$; $m = n = 1, 5, 9, ..., 21$	$652s$ $C_f = 4.9$	$340s$ (-48%)	$1487s$ $C_f = 9.8$	$621s$ (-58%)
blade unit	9	$k = 2, 4, 6, ..., 14$; $m = n = 1, 3, 5, ..., 15$	$145s$ $C_f = 0.7$	$165s$ (+14%)	$245s$ $C_f = 1.5$	$223s$ (-9%)
blade unit	9	$k = 2, 6, 10$; $m = n = 1, 5, 9, 13$	$21s$ $C_f = 0.6$	$22s$ (+5%)	$32s$ $C_f = 1.1$	$28s$ (-13%)

NODE1: IBM RS/6000 model 590 with 512MB RAM
NODE2: IBM RS/6000 model 390 with 256MB RAM

Another factor which affects the relative effectiveness of the reduced solution procedure is the selection of the error tolerance, $\hat{e}$. At the end of each step of the reduced solution procedure, the normalized error tolerance, e, is computed and compared to $\hat{e}$. If e is greater than $\hat{e}$, a new set of basis vectors is generated before proceeding with the solution. If $\hat{e}$ is too large, new sets of basis vectors are not generated when they are needed and the solution procedure either diverges or generates erroneous results. If $\hat{e}$ is too small, new sets of basis vectors are generated more often than they are needed, and the computational cost of the solution procedure increases.

Unfortunately, there is no fixed value for $\hat{e}$ that can be recommended for all problems. For the five blade stiffened panel examples, for instance, the "best" $\hat{e}$ value varied from 0.010 to 0.050. In the case of a small model and/or a relatively simple response, it may not be particularly important to select the "best" $\hat{e}$ (computational costs will be low anyway), but if the problem is large and/or has a complex non-linear response, the choice of $\hat{e}$ can significantly affect the final computational costs of the reduced method.

For example, for the first stiffener unit example discussed above (model 4) the reduced solution was obtained in $165s$ on NODE1 and $223s$ on NODE2 with $\hat{e} = 0.024$ (basis vectors were re-computed three times). If $\hat{e}$ is reduced to 0.010, the computational costs of the reduced solution procedure rise significantly: $226s$ (+37%) on NODE1 and $318s$ (+43%) on NODE2 (basis vectors are re-computed five times in this case). For the second symmetric model discussed above (model 2), the reduced solution was obtained in $128s$ on NODE1 and $198s$ on NODE2 when $\hat{e}$ was 0.018 (basis vectors were re-computed three times). If $\hat{e}$ is reduced to 0.010, the reduced solution is obtained in $184s$ (+30%) on NODE1 and $284s$ (+30%) on NODE2 (basis vectors are re-computed five times).

Finally, the effectiveness of both solution procedures is influenced to a small extent by the step size parameter, $\bar{m}$. This parameter helps to control the arc-length step size used by the incremental/iterative solution procedure (see section 3.5). A large $\bar{m}$ value will generally result in larger step sizes (and fewer total steps). This translates into improved computational efficiency. If $\bar{m}$ is too large, however, the solution will diverge. For all of the examples presented in this chapter, $\bar{m}$ was in the range 6-8.

Chapter 5

Global/Local Interface

In this chapter, the proposed global/local design procedure and details concerning its implementation in the `ADOP` design environment are described. Results obtained using a simple isotropic global wing model are presented in Chapter 6.

5.1 Design Procedure

The first step in the proposed global/local design procedure is to define one or more design regions or "panels" at the global level. These panels will represent those portions of the global structure that will be designed in detail by the local design code. The overall dimensions of these global panels are used to create detailed local design models. In general, it will be necessary to create a local model corresponding to each global panel, although in many cases it will prove possible to represent several global panels with a single local model. During the construction and definition of the local models, local design variables and local design constraints are specified. In the case of a stiffened panel, local design variables are usually skin and stiffener ply thicknesses and orientations as well as stiffener cross-sectional dimensions. A variety of local failure constraints, such as buckling, strength, damage tolerance, and manufacturing and cost constraints may conceivably be imposed.

For each of the global design regions, it is necessary to estimate the ranges over which the in-plane loads and in-plane stiffnesses will vary during the global design optimization process. These estimates take the form of upper and lower bounds on the in-plane loads N_x, N_y, and N_{xy}, as well as upper and lower bounds on the average in-plane stiffness parameters $\bar{A}_{11}$, $\bar{A}_{22}$, and $\bar{A}_{66}$. These bounds will serve as limits on each of the local panel optimizations.

Once each local model has been constructed and the load and stiffness bounds have been estimated, the local design code is used to generate a series of optimal (minimum weight) designs for each panel. Each optimal design is generated as a function of the parameters N_x, N_y, N_{xy}, $\bar{A}_{11}$, $\bar{A}_{22}$, and $\bar{A}_{66}$, selected from within their respective bounds. Each of these designs is generated such that it does not violate any of the local design constraints when subjected to the loads N_x, N_y, and N_{xy}. In addition, each design is further constrained to match the specified $\bar{A}_{11}$, $\bar{A}_{22}$, and $\bar{A}_{66}$ values.

This series of optimal designs is then used to generate a response surface approximation of the optimal panel weight as a function of N_x, N_y, N_{xy}, $\bar{A}_{11}$, $\bar{A}_{22}$, and $\bar{A}_{66}$. Within the specified load and stiffness ranges, each response surface approximates the optimal (minimum) weight of a panel that satisfies all the local failure constraints and matches the given stiffness parameters. Depending on the comparative dimensions and load/stiffness ranges for each of the global panels, it may be possible to construct a single response surface that is valid for several different design regions. Care should be taken, however, as the accuracy of the response surface will generally decrease as the load and stiffness ranges get larger. A more detailed discussion of the response surface construction and response surface modeling in general is presented below in section 5.2.

The response surfaces are then used to establish a common interface between the global and local design codes. During the global design iterations, the local code is replaced by the response surface(s). There are several advantages to this approach. Because the response surfaces are generated before the global/local iterations begin, the designers may take whatever time is necessary to ensure that each of the local optimal designs (and therefore each response surface) is accurate. For example, the designers will be able to take the time to ensure that each of the local optimal designs is a global optimum (as opposed to a local optimum). The response surface approach also allows for a more compartmentalized approach to the global/local design process, such as might be found in large organizations. Designers and analysts who specialize in detailed design may direct the construction of the response surfaces and then pass the resulting data to those designers who work with the global model.

In addition to the built-in flexibility of the proposed method, it should prove to be more efficient than current design methods. As compared to conventional global/local design methodology, the primary computational expense of the proposed method occurs before the global iterations actually begin, during the generation of the response surface models. Once accurate response surfaces are obtained, the designer may access the local design information over and over again at very little additional expense. This will be true as long as changes are not made to the global model which result in significant load or stiffness re-distributions. The computational expense incurred in generating the response surfaces will depend on the efficiency of the chosen local design code and upon the judgment of the designer. If the designer makes inaccurate initial choices when selecting the initial load and stiffness bounds for a given response surface, it may be necessary to go back and generate additional local designs before a satisfactory response surface can be obtained.

In the proposed scheme, the global optimizer interacts with the response surface through a "weight margin" or "weight constraint". This interaction is illustrated in Figure 5.1. For each global panel, and at each design iteration, the global optimizer passes values of the current in-plane loads N_x, N_y, and N_{xy} as well as the current in-plane stiffness values $\bar{A}_{11}$, $\bar{A}_{22}$, and $\bar{A}_{66}$ to the response surface model. The response surface then returns the minimum weight of a local panel that does not violate any local constraints when subjected to the given in-plane loads and that has in-plane stiffness parameters equal to the given stiffness parameters. By keeping the in-plane stiffness parameters constant at the local level, no

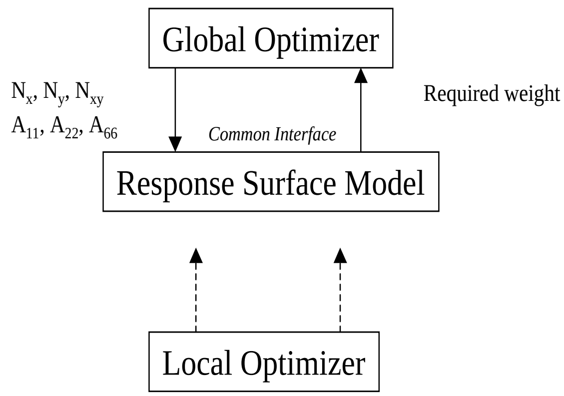

Figure 5.1: Proposed Global/Local Interface

load redistribution occurs at the global level because of local design changes. This prevents the local optimizer from inadvertently violating global constraints that depend on the panel stiffness.

The global optimizer then compares this optimal local panel weight with the global panel weight (calculated using the global design variables) and a "weight constraint" is calculated. This single constraint includes the effects of all of the constraints imposed on the local model. This local panel constraint is formulated as follows:

$$g_l = 1.0 - \frac{w_g}{w_l} \leq 0.0 \tag{5.1}$$

where w_g is the weight of the global panel (calculated by the global design code) and w_l is the optimal weight of the local panel (obtained from the response surface model). The exact relationship between the global panel weight computation and the local panel weight computation will, of course, depend on the procedure used by the local optimizer to calculate the local stiffnesses.

If w_l is less than w_g, the weight constraint is inactive. This means that, for the given load and stiffness requirements, the local design code is capable of generating a panel design which weighs less than the current global panel and which satisfies all of the local constraints. In this case, the global design has a positive weight margin with respect to g_l and the global optimizer may try to further reduce the global panel weight or redistribute the global loads in future iterations. If w_l is greater than w_g, the constraint is violated. This implies that, for the given load and stiffness requirements, the local design code is unable to generate a design which satisfies the local panel constraints without increasing the local panel weight beyond that of the global panel. In this case, the global design has a weight deficiency with respect to g_l, and the global optimizer must manipulate the global design variables in future iterations in order to satisfy this constraint. If w_l equals w_g (the global panel weight equals the optimal local panel weight), the constraint is active.

5.2 Response Surface Approximation

Response surface methodology consists of a group of statistical techniques used for empirical model building. In general, the methodology is used to approximate the complex relationship between a set of *input* variables and an output, or *response* variable using a relatively simple functional relationship or model. Because the actual relationship between the input variables and the response variable is complex (or unknown), the response surface approximation is valid only for a finite and restricted range of the input variables.

The first step in constructing a response surface approximation is to determine the ranges of the input variables over which the approximation will be constructed. Care should be taken so as not to select too large a range for the approximation; in general, the accuracy of the approximation will decrease as the variable ranges increase. Once the ranges have been established, the response variable is evaluated at a number of discrete "design points", or combinations of the input variables. A number of different schemes or "designs" have been devised for selecting appropriate sets of design points; these include the various factorial designs and "alphabetic" optimal designs [69]. After the response variable has been evaluated at each design point, the resulting data can be fit to an appropriate model. Often this model is a low order polynomial, in which case the coefficients of the polynomial are determined using a least-squares fit. Once the model is constructed, its accuracy is evaluated and improved as required. The accuracy of a given model may be improved by scaling the input and/or output variables or by eliminating unnecessary input variables, for example. If the model's accuracy is still not adequate, it may be necessary to either resort to a higher order model or to further restrict the range of the input variables.

In the context of the present work, we wish to construct a response surface approximation to the optimal local panel weight as a function of the in-plane load and stiffness parameters. The first step is to determine the range of the input variables over which we wish to make the approximation. As stated, it is necessary to estimate upper and lower bounds on the in-plane loads N_x, N_y, and N_{xy}, as well as upper and lower bounds on the in-plane stiffness parameters $\bar{A}_{11}$, $\bar{A}_{22}$, and $\bar{A}_{66}$. These bounds will be the maximum and minimum values that each of these parameters is expected to take on during the global optimization process. If these bounds are not known with any degree of accuracy, it may be easiest to first obtain average values for each of these parameters and then estimate the bounds using these average values. For example, the lower bound might be obtained by reducing the average value by 50%, and the upper bound might be obtained by increasing the average value by 50%.

After the bounds are established, the local design code is used to generate a series of optimal (minimum weight) designs for each panel. A design is generated at each design point, where a design point is defined as a specified combination of N_x, N_y, N_{xy}, $\bar{A}_{11}$, $\bar{A}_{22}$, and $\bar{A}_{66}$, each of which is chosen from within the specified bounds. As noted, there are several criteria that may be used to select a set of design points for a given problem, but all are complicated by the fact that not all design points are necessarily physically realizable for the present problem. For example, a design point with a high axial load (N_x) and a low axial stiffness ($\bar{A}_{11}$) may lie outside the feasible domain of the local design code. One method of working with these infeasible design points is to assign them an artificially high weight (a penalty term). This will prevent the global optimizer from moving into these design regions (for an example of this approach, see Chapter 6).

Once the optimal panel weights are generated using the local design code, a response surface model is fit through the resulting data. In the present work, least squares techniques are used to fit a low order polynomial. For example, a response surface generated using a second order polynomial in six dimensions has the following general form:

$$\begin{aligned} w_{rsm} \quad = \quad & (c_0 + c_1\bar{A}_{11} + c_2\bar{A}_{22} + c_3\bar{A}_{66} + c_4N_x + c_5N_y + c_6N_{xy} + \\ & c_{11}\bar{A}_{11}\bar{A}_{11} + c_{22}\bar{A}_{22}\bar{A}_{22} + c_{33}\bar{A}_{66}\bar{A}_{66} + c_{44}N_xN_x + c_{55}N_yN_y + \\ & c_{66}N_{xy}N_{xy} + c_{12}\bar{A}_{11}\bar{A}_{22} + c_{13}\bar{A}_{11}\bar{A}_{66} + c_{14}\bar{A}_{11}N_x + c_{15}\bar{A}_{11}N_y + \\ & c_{16}\bar{A}_{11}N_{xy} + c_{23}\bar{A}_{22}\bar{A}_{66} + c_{24}\bar{A}_{22}N_x + c_{25}\bar{A}_{22}N_y + c_{26}\bar{A}_{22}N_{xy} + \\ & c_{34}\bar{A}_{66}N_x + c_{35}\bar{A}_{66}N_y + c_{36}\bar{A}_{66}N_{xy} + c_{45}N_xN_y + c_{46}N_xN_{xy} + \\ & c56N_yN_{xy})^{(\frac{1}{\alpha})} \end{aligned} \tag{5.2}$$

where w_{rsm} is the optimal panel weight, the 28 coefficients c_0 through c_{46} are the coefficients obtained from the least squares analysis, and α is an optional scaling parameter. In this equation, N_x, N_y, N_{xy}, $\bar{A}_{11}$, $\bar{A}_{22}$, and $\bar{A}_{66}$ are usually scaled so that they each range from $(-1, 1)$. A response surface generated using a 3rd order polynomial will, of course, have a similar form; 84 coefficients are used instead of 28 coefficients.

5.3 Implementation in the `ADOP` Design Environment

In the present work, the finite element based design code `ADOP` [1] was used as the global design code. In order to implement the global/local methodology in the `ADOP` design environment, it was necessary to program the proposed "weight constraint" and response surface interface at the global level. The inputs to the response surface from the global design code are the global panel in-plane loads N_x, N_y, and N_{xy} and the average in-plane stiffnesses $\bar{A}_{11}$, $\bar{A}_{22}$, and $\bar{A}_{66}$. Because a global panel is, in general, comprised of a group of several finite elements, it is necessary for the global design code to calculate average load and stiffness values for each global panel.

In the following two sections, the methods programmed in `ADOP` to calculate the average loads and stiffnesses in the case of an isotropic structure are detailed. In the final section, the procedure for calculating constraint derivatives using finite differences is outlined.

5.3.1 Average Panel Loads

In a typical `ADOP` finite element wing model, the wing skin is modeled using membrane elements, and the stiffeners are modeled using rod elements. The following procedure was programmed in `ADOP` to calculate the average panel loads in this case:

First, the average loads in the membrane elements are calculated. These loads represent that portion of the total panel load that is carried in the panel skin. Each `ADOP` membrane element has four gauss points, and associated with each gauss point is a value of N_x^{ele}, a value of N_y^{ele}, and a value of N_{xy}^{ele}, each in the element coordinate system and in units of (lb/in). These loads are first converted to the panel coordinate system using user supplied direction cosines. In the panel coordinate system, the x-direction is parallel to the stringers, and the y-direction is in the plane of the skin. After these element loads have been converted to the panel coordinate system, `ADOP` searches for the maximum load components in each element. These maximum values are assumed to act over the entire element. The total loads on the panel skin are then obtained by averaging these maximum element loads over the total number of membrane elements in the panel. The resulting N_y^{sk} and N_{xy}^{sk} are equal to the final load values used for the panel, N_y^{tot} and N_{xy}^{tot}. The resulting N_x^{sk} value must be combined with the total force in the rod (stringer) elements in order to obtain the total force in the x-direction.

The force in the stringers is obtained from the rod elements. Each rod element has an F_x^{ele} value (lb) associated with it. The total stringer force is then obtained by summing the forces from each rod element in the panel. This value, F_x^{st}, must then be combined with the N_x^{sk} value obtained from the membrane elements. First, the membrane N_x^{sk} value is converted to a force by multiplying by the total width of the panel. This skin force may then be added to the stringer force F_x^{st} to obtain a total panel force, F_x^{tot}. This force is then converted into N_x^{tot} by dividing by the total panel width. This final value of N_x^{tot}, along with N_y^{tot} and N_{xy}^{tot} obtained above, are passed to the response surface model.

It should be noted that the number of stringers present in the global model for a given panel may differ from the number of stringers present in the local analysis model for that same panel. This will be the case when several local stringers are lumped into a single global stringer for modeling efficiency reasons. The above calculations take into account this possibility.

5.3.2 Average Panel Stiffness

The following procedure was programmed in `ADOP` to calculate the average panel stiffnesses. For each membrane element, $\bar{A}_{11}^{ele}$, $\bar{A}_{22}^{ele}$, and $\bar{A}_{66}^{ele}$ are calculated using the following formulas:

$$\bar{A}_{11}^{ele} = Et_b \tag{5.3}$$

$$\bar{A}_{22}^{ele} = Et_b \tag{5.4}$$

$$\bar{A}_{66}^{ele} = Gt_b \tag{5.5}$$

where t_b is the thickness of the membrane. These element membrane stiffnesses are averaged over all the membrane elements in the panel to arrive at the average membrane stiffnesses $\bar{A}_{11}^{sk}$, $\bar{A}_{22}^{sk}$, and $\bar{A}_{66}^{sk}$. The skin in each repeating element of the panel will be assumed to have these average stiffness values. Because the stringers are assumed to have no contribution to the shear or transverse stiffnesses, $\bar{A}_{66}^{sk}$ will be equal to the total panel shear stiffness, $\bar{A}_{66}^{tot}$, and $\bar{A}_{22}^{sk}$ will be equal to the total panel transverse stiffness, $\bar{A}_{22}^{tot}$. The stringer axial stiffness must be added to $\bar{A}_{11}^{sk}$ in order to obtain the total axial stiffness.

The stringer axial stiffness, $\bar{A}_{11}^{st}$, is computed using the rod elements. For each rod element, the axial stiffness is calculated using the following formula:

$$(EA)^{ele} = ES \tag{5.6}$$

where S is the area of the rod element. The average element axial stiffness, $(EA)^{avg}$, is obtained by averaging $(EA)^{ele}$ over the total number of rod elements in the panel. Each stringer in the global panel is assumed to have this average axial stiffness. The total stringer axial stiffness for the panel is obtained by multiplying this average stringer stiffness, $(EA)^{avg}$, by the total number of global stringers in the panel. This total axial stiffness is then divided by the number of stringers in the local model and the stringer spacing in the local model to obtain the $\bar{A}_{11}^{st}$ value for a single local stringer.

The final $\bar{A}_{11}^{tot}$ value for the panel is obtained as follows:

$$\bar{A}_{11}^{tot} = \bar{A}_{11}^{sk} + \bar{A}_{11}^{st} = \bar{A}_{11}^{sk} + (EA)^{avg}(\frac{n_r}{n_l b_b}) \tag{5.7}$$

where b_b is the local panel stringer spacing, n_r is the number of stringers in the global panel, and n_l is the number of stringers in the local panel. $\bar{A}_{11}^{tot}$, $\bar{A}_{22}^{tot}$, and $\bar{A}_{66}^{tot}$ are passed to the response surface model.

A variety of different methods for obtaining the average panel forces and stiffnesses from the global finite element model may be envisioned. Alternative methods may be easily incorporated into `ADOP` if desired.

5.3.3 Constraint Derivatives

In order to arrive at an optimal solution, the global design code needs to be able to calculate derivatives of the local panel constraint with respect to each of the global design variables. The derivative of the local panel constraint with respect to the ith design variable, $\frac{\partial g_l}{\partial D_i}$, is calculated using finite differences.

The following procedure is followed for each design variable. First, a perturbed value of the design variable, D_i', is obtained by incrementing the ith design variable by a small number, ΔD_i:

$$D_i' = D_i + \Delta D_i \tag{5.8}$$

`ADOP` then internally calculates the derivatives of the internal loads with respect to the ith design variable, $\frac{\partial f_{int}}{\partial D_i}$. These derivatives are calculated using many of the same subroutines already used to calculate stress derivatives in `ADOP`. These internal force derivatives are multiplied by ΔD_i in order to obtain the increment in the internal force vector. The updated internal force vector, f_{int}', is then obtained as follows:

$$f_{int}' = f_{int} + \frac{\partial f_{int}}{\partial D_i} \Delta D_i \tag{5.9}$$

The updated load parameters N_x', N_y', and N_{xy}' may be extracted from this vector. The updated stiffness parameters $\bar{A}_{11}'$ and $\bar{A}_{66}'$ as well as the updated global panel weight, w_g', are easily obtained in `ADOP` by calling the original stiffness and weight routines with the perturbed value of the design variable, D_i'.

Next, the updated load and stiffness parameters N_x', N_y', N_{xy}', $\bar{A}_{11}'$, and $\bar{A}_{66}'$ are passed to the response surface model and the updated local panel weight, w_l', is returned. The updated constraint value, g_l', can then be calculated using equation 5.1. Finally, the desired constraint derivative may be calculated as follows:

$$\frac{\partial g_l}{\partial D_i} = \frac{g_l' - g_l}{\Delta D_i}. \tag{5.10}$$

Chapter 6

Results: Global/Local Interface

In this chapter, results obtained with the proposed global/local design procedure are presented. The proposed global/local methodology was implemented using the McDonnell Douglas Aeroelastic Design Optimization Program, `ADOP` [1]. The purpose of the initial studies presented in this chapter was to validate the proposed global/local methodology, and several simplifications in the general procedure were made accordingly. First, the initial studies were restricted to the design of isotropic structures. This restriction reduced the number of design variables in the problem and simplified both the global and local design tasks. Secondly, we limited ourselves to a single local design code, `PASCO` [2]. This code is widely available and reasonably robust.

The `ADOP` global wing model is described in section 6.1, and the local `PASCO` model and the generation of the corresponding response surface model is outlined in section 6.2. In section 6.3, results are presented that were obtained in conjunction with global stress constraints, and in section 6.4, results are presented that were obtained in conjunction with both global stress constraints and a global displacement constraint.

6.1 Global Wing Model

Validation of the proposed global/local design procedure was performed using a simple global wing model illustrated in Figure 6.1. This un-tapered wing has a 350 *in* span and a 30° sweep angle. In the global model, the spar and rib panels were modeled using membrane elements, and the skin panels are modeled using membrane elements and rod elements. The (isotropic) material properties were assumed to be E=10.7E6 *psi* and ν=0.3.

Four of the upper cover panels (marked "PANEL 1" through "PANEL 4" in the figure) were designed using the proposed global/local procedure. Global design variables included the thicknesses of membrane elements and the areas of rod elements. In most cases, a single global design variable controlled the sizing of several related finite elements; for example, the thickness of each rib panel was controlled by a single design variable. The skin elements in panel 1 were controlled by one design variable, and the rod elements in panel 1 were controlled by a separate design variable. The same scheme was followed for panels 2 through 4. The portion of the upper skin inboard of panel 1 was constrained to have the same membrane thickness and rod area as panel 1. Likewise, the portion of the upper skin outboard of panel 4 was constrained to have the same membrane thickness and rod area as panel 4. There were 33 global design variables: 23 thickness design variables and 10 area design variables.

6.2 Generation of the Response Surface Model

In order to generate response surface models for the wing panels, it was necessary to create a detailed `PASCO` models of the panel cross sections. A typical `PASCO` repeating element is illustrated in Figure 6.2. Six design variables were used for the detailed local panel design: the thickness of the skin, the thicknesses of the upper and lower flanges, the thickness and length of the web, and the length of the outer flange.

Panels 1 through 4 have the same overall dimensions: a width of 64.95 *in*, and a length of

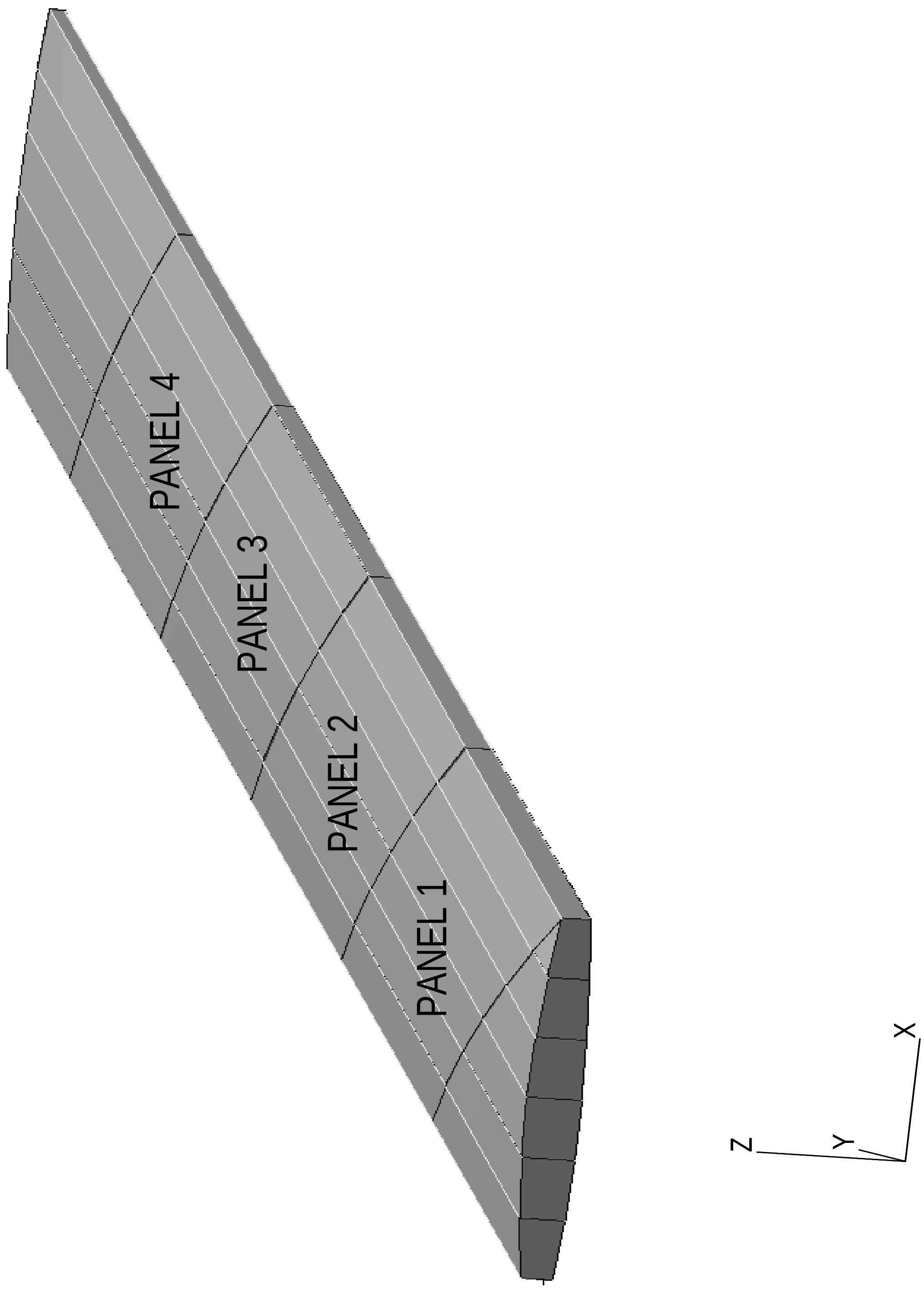

Figure 6.1: `ADOP` global wing model

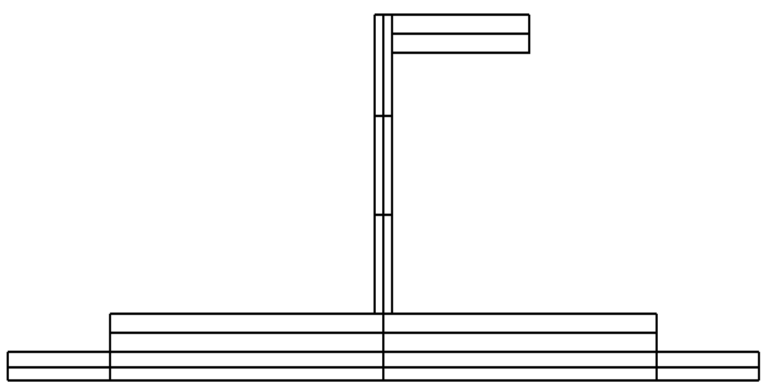

Figure 6.2: Typical PASCO repeating element

80.82 *in*. A stringer spacing of 5.413 *in* was assumed for all three panels (this translates to 12 stringers per panel). The PASCO models were generated assuming that the lateral edges of the panels (at the skin/spar interface) were simply supported. It should be noted that PASCO has a limited capability to impose stiffness constraints on the designs that it generates. First, it only allows stiffness constraints to be imposed on $\bar{A}_{11}$ and $\bar{A}_{66}$ but not on $\bar{A}_{22}$. This means that, at present, there is no way to constrain the local PASCO designs to a given $\bar{A}_{22}$. In the development to follow, then, the response surfaces are generated as a function of N_x, N_y, N_{xy}, $\bar{A}_{11}$, and $\bar{A}_{66}$ only ($\bar{A}_{22}$ is omitted). Secondly, the stiffness constraints that may be imposed on

A single response surface was generated for all four panels. The following load and stiffness ranges were used (*lb/in*):

$$
\begin{aligned}
-9000 \leq \quad & N_x & \leq 0 \\
-450 \leq \quad & N_y & \leq 0 \\
0 \leq \quad & N_{xy} & \leq 300 \\
1.5\text{E}6 \leq \quad & \bar{A}_{11} & \leq 4.0\text{E}6 \\
0.15\text{E}6 \leq \quad & \bar{A}_{66} & \leq 1.0\text{E}6
\end{aligned}
\tag{6.1}
$$

An initial set of 42 design points was selected for generating the response surface model (this number is somewhat arbitrary; it corresponds to twice the number of points required to fit a second order polynomial in five dimensions). The design points were selected using the D-Optimality Criterion [69]. This criterion states that design points should be selected in order to maximize:

$$|Z^T Z| \tag{6.2}$$

where Z is the least squares matrix containing the scaled coordinates of the design points and their products. In the present application, a genetic algorithm was used to maximize $|Z^T Z|$ and thereby select the design points. This procedure was similar to that described in [70]. In the present work, each of the five load and stiffness parameters was scaled to vary between -1.0 and 1.0 in discrete increments of 0.02. Although there is no guarantee that a genetic algorithm will converge to the globally optimum set of design points, it will usually produce a family of optimal or near optimal designs. The genetic algorithm used for this study has been shown to converge to the known global optimum set of points for several two parameter test cases.

Once the 42 design points were selected using the genetric algorithm, `PASCO` was run at each point. Each local design was generated subject to constraints on material strength and panel buckling. Because `PASCO` is not capable of imposing equality constraints on the stiffness parameters (only upper and lower bound constraints may be imposed), it was necessary to run `PASCO` up to four times for each design point, each run corresponding to different combinations of the upper and lower bounds on $\bar{A}_{11}$ and $\bar{A}_{66}$. The result of this procedure was the generation of up to four candidate `PASCO` designs corresponding to each attempt to match each of the original design points. In some cases, one of these candidate designs matched the corresponding original design point. If, however, `PASCO` was unable to generate a candidate design matching the original design point, the original design point was marked as infeasible and discarded. Regardless of whether or not a given design point was matched by `PASCO` or not, all unique designs that were generated in this process were retained and used to generate the response surface model. The total number of design points obtained in this manner was approximately 100. Using this data, a response surface was generated using least squares techniques and scaling to fit a second order polynomial.

When the resulting response surface was interfaced with the global design code and tested, difficulties were encountered. During the global iterations, `ADOP` tended to advance the local panel designs into infeasible portions of the design space. This occurred because the response surface was incomplete; no information corresponding to the infeasible local design points was included in the response surface model. The design regions bordering the infeasible regions were often those with low structural weights, and because the response surface contained no contrary information, this trend was continued into the infeasible region.

In an attempt to correct this problem, new response surfaces were constructed using data that included penalty terms for those original design points for which PASCO could not generate a feasible design. The general procedure was the same as that outlined above. This time, however, all of the original design points were retained. The weight used for the infeasible original design points was that of one of the alternate design points plus a penalty term (described below). When these additional terms were included, it was necessary to use a 3rd order to polynomial to obtain an accurate fit to the data.

6.2.1 Calculation of Penalty Terms

When PASCO was unable to converge to a feasible design at or near one of the original design points, the infeasible design point was still retained for use in generating the response surface model. The panel weight used for the infeasible design point was that of an alternate feasible point plus a variable penalty term. The alternate feasible point was chosen from the data that PASCO had generated in the attempt to match the original design point, and was chosen to be as near to the original design point as possible. A "nearby" point was defined as a design point that had the same values for the three load parameters as did the original design point, and with values for the two stiffness parameters as close as possible to those of the original design point. Typically, the chosen alternate points matched one of the stiffness parameters from the original design point, but not both.

Given the fact that the weight corresponding to the infeasible original design point was not allowed to drop below that of the alternate design point (the penalty term was not allowed to be less than zero), an optimization problem was set up to determine the values for the penalty terms. The objective was to minimize the root mean square error of the resulting response surface fit to the complete set of data. The design variables were the penalty terms, and except for the requirement that they remain positive, there were no additional constraints imposed on the problem. The task was accomplished using the multi-purpose optimization code, ADS [71]. In retrospect, this particular scheme for selecting the design points seems overly complex; other simpler schemes for determining the penalty terms may be devised as well.

6.2.2 Accuracy Assessment

One criterion that was used to assess the quality of fit is a biased measure of the root mean square error (e_{RMS}) defined as follows:

$$e_{RMS} = \sqrt{\frac{1}{(N-\beta)} \sum_{i=1}^{N} (w - \hat{w})^2} \tag{6.3}$$

where N is the total number of points considered, β the number of coefficients in the polynomial (in this case 56), w is the exact value of the weight function (determined from `PASCO`), and $\hat{w}$ is the approximate value of the weight function. The present response surface was created using 104 design points and had an e_{RMS}=2.2 *lb*. This value may be compared to typical panel weights that range from 80 *lb* to 200 *lb*. Another measure of the quality of fit is the R^2 statistic, which represents the fraction of the variation about the mean that is explained by the fitted model [69]. It has a maximum value of 1.0, with values of R^2 near 1.0 indicating a good fit. R^2 for the present response surface model was calcluated to be .9993. The R^2 statistic may be adjusted to take into account the number of coefficients in the response surface model; in this form, denoted as R_a^2, the statistic gives an improved indication of the predictive capabilities of the approximation. For the present model, R_a^2=.9986.

6.3 Example 1: Global stress constraints

In this first test case, global stress constraints were imposed on all elements in the model. In addition, response surface or "local panel constraints" were imposed on panels 1 through 4. The membrane stress constraints were based on the Von Mises failure criterion with a shear allowable of ±37,155 *psi*. The rod stress constraints were based on the maximum stress criterion, with a stress allowable in tension and compression of ±55,000 *psi*. A lower bound of .0125 *in* was imposed on all thickness design variables, and a lower bound of .05 in^2 was imposed on all area design variables. The global design was generated using a single load case, consisting of a 3600 *lb* upward load applied at the wing tip.

When extracting internal panel loads from the global model during the global/local iterations, the load on each panel was assumed to be 5% of the corresponding (compressive) load. This was done because the loads that were obtained directly from the global model varied wildly in both magnitude and sign from panel to panel due to the coarseness of the global finite element mesh.

After convergence of the global design problem, all four local panel constraints were active along with 19 global stress constraints. The final weights of panels 1 through 4 were 143.2 *lb*, 125.4 *lb*, 104.4 *lb*, and 80.5 *lb*, respectively. The final load and stiffness parameters for each are presented in Table 6.1.

In order to obtain the final local details for each of these panels, a final `PASCO` optimization must be performed for each. This final optimization also allows the accuracy of the response surface(s) to be assessed. The results of these final `PASCO` runs are presented in Table 6.2. Note that for panel 2, `PASCO` was able to generate a design that exactly matched the final global load and stiffness parameters. For panels 1, 3 and 4, `PASCO` was unable to exactly match the stiffness parameters, although it was able to generate designs that were quite close to the desired values. For panel 3, two `PASCO` designs are presented: panel 3A and panel 3B. Both designs have the same weight, but one of them has an $\bar{A}_{66}$ slightly larger than required,

Table 6.1: Example 1 – Final ADOP global load and stiffness parameters

Panel	A_{11}	A_{66}	N_x	N_y	N_{xy}	w
1	2.91E6 lb/in	0.72E6 lb/in	-6455 lb/in	-323 lb/in	83 lb/in	143.2 lb
2	2.54E6 lb/in	0.64E6 lb/in	-4952 lb/in	-248 lb/in	99 lb/in	125.4 lb
3	2.12E6 lb/in	0.55E6 lb/in	-3455 lb/in	-173 lb/in	73 lb/in	104.4 lb
4	1.63E6 lb/in	0.42E6 lb/in	-2056 lb/in	-103 lb/in	69 lb/in	80.5 lb

Table 6.2: Example 1 – Final PASCO load and stiffness parameters

Panel	A_{11}	A_{66}	N_x	N_y	N_{xy}	w_{pas}
1	2.91E6 lb/in	0.75E6 lb/in	-6455 lb/in	-323 lb/in	83 lb/in	142.5 lb
2	2.54E6 lb/in	0.64E6 lb/in	-4952 lb/in	-248 lb/in	99 lb/in	124.8 lb
3A	2.12E6 lb/in	0.55E6 lb/in	-3455 lb/in	-173 lb/in	73 lb/in	104.0 lb
3B	2.12E6 lb/in	0.53E6 lb/in	-3455 lb/in	-173 lb/in	73 lb/in	104.0 lb
4	1.67E6 lb/in	0.45E6 lb/in	-2056 lb/in	-103 lb/in	69 lb/in	82.1 lb

and one of them has an $\bar{A}_{66}$ slightly smaller than required. Panel 3A was obtained using a lower bound on the required $\bar{A}_{66}$ and panel 3B was obtained by imposing an upper bound on $\bar{A}_{66}$. If PASCO were capable of imposing equality constraints on the stiffness parameters, an exact match would have been found in this case.

In order to assess the effect of the stiffness deviations in panels 1,3, and 4 on the stress distribution in the global model, the global model was modified to reflect the final PASCO designs in Table 6.2 and a single analysis was performed. When panel 3A was included, no global stress constraints were violated. When panel 3B was included, there was a 0.6% violation of

Table 6.3: Example 1 – Final PASCO designs

Panel	t_{sk}	t_{fl}	t_{wb}	l_{wb}	t_{fu}	l_{fu}	w_{rsm}	w_{pas}
1	.149 *in*	.049 *in*	.077 *in*	3.97 *in*	.184 *in*	.890 *in*	143.2 *lb*	142.5 *lb*
2	.132 *in*	.035 *in*	.064 *in*	3.63 *in*	.249 *in*	.811 *in*	125.4 *lb*	124.8 *lb*
3A	.111 *in*	.035 *in*	.062 *in*	3.77 *in*	.129 *in*	.759 *in*	104.3 *lb*	104.0 *lb*
3B	.105 *in*	.035 *in*	.064 *in*	3.69 *in*	.192 *in*	.684 *in*	104.3 *lb*	104.0 *lb*
4	.089 *in*	.028 *in*	.047 *in*	3.39 *in*	.175 *in*	.523 *in*	80.6 *lb*	82.1 *lb*

one of the global stress constraints. In both cases, the resulting load re-distribution in the four upper panels was small compared to the values given in Table 6.1.

The details of the final PASCO designs are presented in Table 6.3 and a graphical representation of a repeating element of each of the final panel designs are presented in Figures 6.3 through 6.7. In Table 6.3, t_{sk} is the thickness of the skin, t_{fl} is the thickness of the lower flange, t_{wb} and l_{wb} are the thickness and length of the web, and t_{fu} and l_{fu} are the thickness and length of the upper flange. w_{rsm} is the weight that was predicted by the response surface, and w_{pas} (repeated from Table 6.2) is the weight predicted by a single PASCO optimization run.

Agreement between the predicted response surface weight and the actual PASCO weight is good in all four cases. All four panels appear to have realistic configurations, although it may be desirable to impose some type of manufacturability constraints on future designs. Compared to Panel 3A, Panel 3B appears to better follow the general design trends set by the other three panels. Each of the PASCO designs was buckling critical. The critical compressive axial stress for panel 1 was approximately 24,100 *psi*, the critical compressive axial stress for panel 2 was approximately 21,100 *psi*, the critical compressive axial stress for panel 3A and panel 3B was approximately 17,700 *psi*, and the critical compressive stress for panel 4

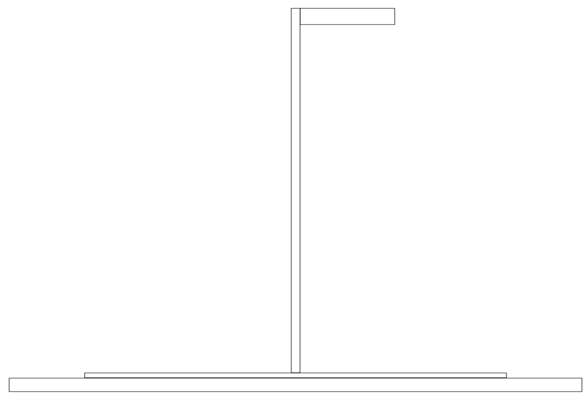

Figure 6.3: Example 1 – Panel 1 final design

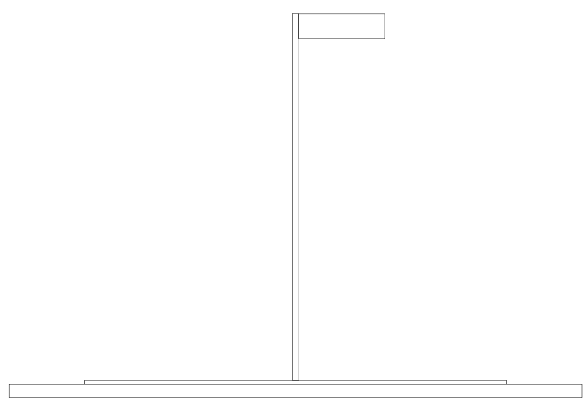

Figure 6.4: Example 1 – Panel 2 final design

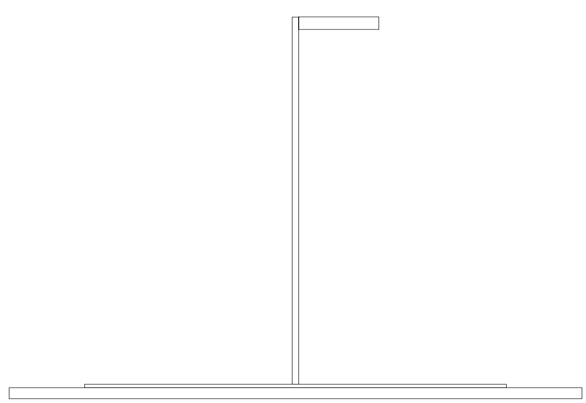

Figure 6.5: Example 1 – Panel 3A final design

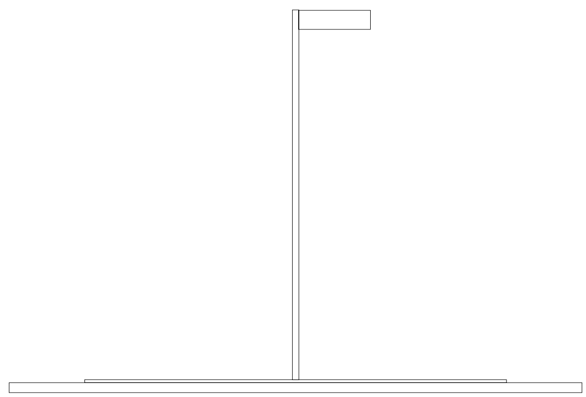

Figure 6.6: Example 1 – Panel 3B final design

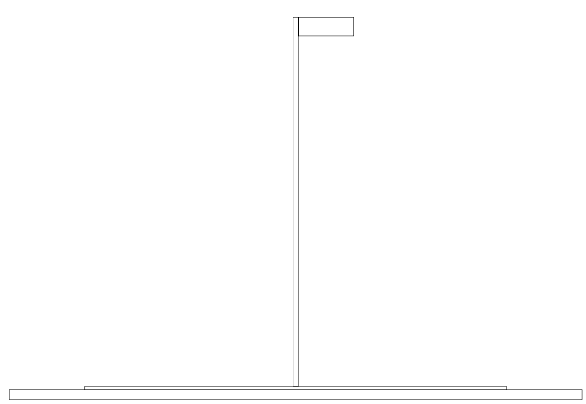

Figure 6.7: Example 1 – Panel 4 final design

was approximately 13,300 *psi*. These stresses are considerably below the maximum axial stress allowables for these elements (±55,000 *psi* in tension/compression). It is noted that the assumption of simply supported edges at the skin-spar interface may cause the PASCO buckling analyses to be overly conservative.

6.4 Example 2: Global Stress and Displacement Constraints

The results presented in this section were obtained in the same manner and with the same global model as those presented in section 6.3. In addition to the global stress constraints that were imposed in the previous example, an additional constraint is imposed on the deflection of the wingtip. This displacement constraint is concerned with the response of the wing structure as a whole, and as such, will affect the local designs previously obtained for panels 1-4. Although displacement constraints are not generally used in the design of real wing structures, other more complicated constraints on the global wing response (such as aeroelastic constraints) are often critical. The displacement constraint is a step towards the imposition of these more complicated constraints. In the present example, the wingtip is restricted to a vertical displacement of 30 *in*. In comparison, the vertical wingtip deflection for the design obtained in section 6.3 was 55.9 *in*.

When the present example was first executed, a problem with the response surface model was discovered. During the course of the global design iterations, intermediate (feasible) designs were sometimes obtained where the predicted weight for panel 4 was in the range of 20-30 *lb*. When this occured, the global design procedure failed to converge. When these lightweight panel 4 designs were examined, it was found that there was a discrepancy between the predictions of the response surface model and PASCO for these designs. PASCO was able to generate a feasible design matching the required load and stiffness parameters,

Table 6.4: Comparison – corrected vs. original RSM results for Example 1

Panel	w_{orig} (lb)	w_{corr} (lb)
1	143.2	142.6
2	125.4	125.6
3	104.4	106.4
4	80.6	84.2

but the resulting design was considerably heavier than that predicted by the response surface model. This discrepancy between the response surface model and `PASCO` in this case was resolved by taking these `PASCO` designs and adding them to the dataset that was originally used to generate the response surface model. A new "corrected" response surface model was generated using this new dataset. This corrected response surface model had the following characteristics:

$$\begin{aligned} e_{RMS} &= 2.4lb \\ R^2 &= 0.9993 \\ R_a^2 &= 0.9986 \end{aligned} \tag{6.4}$$

As compared to the original (un-corrected) response surface, this model has a slightly higher e_{RMS} (2.4 lb vs. 2.2 lb), but identical values of R^2 and R_a^2. In Table 6.4, the predictions of the corrected response surface model are compared to the predictions of the original response surface model for the four final panel designs presented in section 6.3. The largest discrepancy occurs for panel 4, where there is a 4.4% difference. Compared to the actual `PASCO` result (Table 6.3), however, there is only a 2.6% difference.

Using the corrected response surface model, two different global designs were successfully

Table 6.5: Example 2A – Final ADOP global load and stiffness parameters

Panel	A_{11}	A_{66}	N_x	N_y	N_{xy}	w
1	3.21E6 *lb/in*	0.93E6 *lb/in*	-6200 *lb/in*	-310 *lb/in*	91 *lb/in*	158.3 *lb*
2	2.63E6 *lb/in*	0.76E6 *lb/in*	-4754 *lb/in*	-238 *lb/in*	106 *lb/in*	129.5 *lb*
3	2.16E6 *lb/in*	0.60E6 *lb/in*	-3275 *lb/in*	-164 *lb/in*	71 *lb/in*	106.5 *lb*
4	1.73E6 *lb/in*	0.46E6 *lb/in*	-1883 *lb/in*	-94 *lb/in*	70 *lb/in*	85.1 *lb*

obtained. Both of these designs had essentially the same values for the global wing weight (which was 41% heavier than the Example 1 design), but differed primarily in the distribution of material in the lower wing surface. The first design, Example 2A, had relatively thinner skin elements and larger stiffener elements on the lower surface compared to the second design, Example 2B. Both Example 2 designs showed a marked increase in the spar and lower skin thicknesses compared to the Example 1 design. For both Example 2A and Example 2B, five global constraints were active at the end of the optimization process. These constraints were the displacement constraint, and the global/local "weight" constraint imposed on each of panels 1-4.

The Example 2A and Example 2B upper skin panel designs, which were obtained using the proposed global/local approach, were essentially the same. The final load and stiffness values for each are presented in Table 6.5 and Table 6.6, respectively. The PASCO load and stiffness parameters that were obtained for each of panels 1-4 are presented in Table 6.7, and the corresponding detailed PASCO designs are presented in Table 6.8.

Agreement between the predicted response surface weight and the actual PASCO weight is excellent for each panel. As with Example 1, each of the PASCO local panel designs was buckling critical. The critical compressive axial stresses for Panels 1-4 were 20,800 *psi*, 19,300 *psi*, 16,400 *psi*, and 11,800 *psi*, respectively. Again, these stresses are considerably below the

Table 6.6: Example 2B – Final ADOP global load and stiffness parameters

Panel	A_{11}	A_{66}	N_x	N_y	N_{xy}	w
1	3.22E6 lb/in	0.92E6 lb/in	-6169 lb/in	-309 lb/in	89 lb/in	158.2 lb
2	2.65E6 lb/in	0.77E6 lb/in	-4754 lb/in	-238 lb/in	106 lb/in	130.7 lb
3	2.17E6 lb/in	0.60E6 lb/in	-3264 lb/in	-163 lb/in	72 lb/in	106.5 lb
4	1.70E6 lb/in	0.44E6 lb/in	-1885 lb/in	-94 lb/in	66 lb/in	83.9 lb

Table 6.7: Example 2 – Final PASCO load and stiffness parameters

Panel	A_{11}	A_{66}	N_x	N_y	N_{xy}	w_{pas}
1	3.21E6 lb/in	0.94E6 lb/in	-6200 lb/in	-310 lb/in	91 lb/in	157.4 lb
2	2.66E6 lb/in	0.76E6 lb/in	-4754 lb/in	-238 lb/in	106 lb/in	130.5 lb
3A	2.16E6 lb/in	0.60E6 lb/in	-3275 lb/in	-164 lb/in	71 lb/in	106.0 lb
4	1.73E6 lb/in	0.49E6 lb/in	-1883 lb/in	-94 lb/in	70 lb/in	84.7 lb

Table 6.8: Example 2 – Final PASCO designs

Panel	t_{sk}	t_{fl}	t_{wb}	l_{wb}	t_{fu}	l_{fu}	w_{rsm}	w_{pas}
1	.204 in	.035 in	.072 in	4.01 in	.114 in	.803 in	158.2 lb	157.4 lb
2	.160 in	.034 in	.066 in	3.86 in	.120 in	.742 in	129.5 lb	130.5 lb
3A	.122 in	.035 in	.058 in	3.68 in	.117 in	.689 in	106.5 lb	106.0 lb
4	.101 in	.027 in	.041 in	3.07 in	.192 in	.488 in	85.1 lb	84.7 lb

maximum axial stress allowables for these elements ($\pm$55,000 *psi* in tension/compression).

Figures 6.8 through 6.11 are representations of the final `PASCO` designs presented in Table 6.8. These designs appear to be realistic given the assumptions of the problem. The primary difference between these designs and those obtained for Example 1 (with global stress constraints only) is that these designs have thicker skin elements.

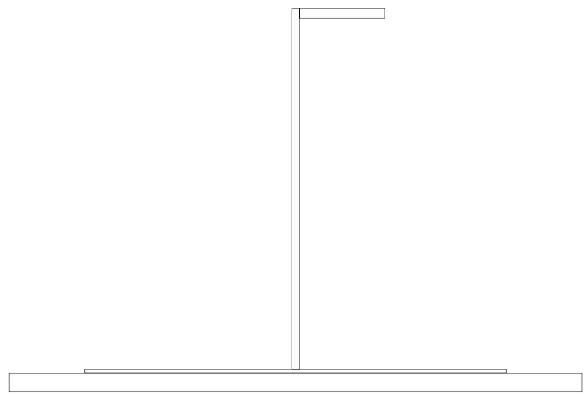

Figure 6.8: Example 2 – Panel 1 final design

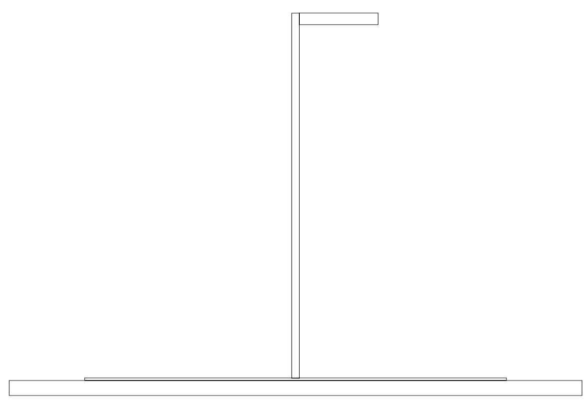

Figure 6.9: Example 2 – Panel 2 final design

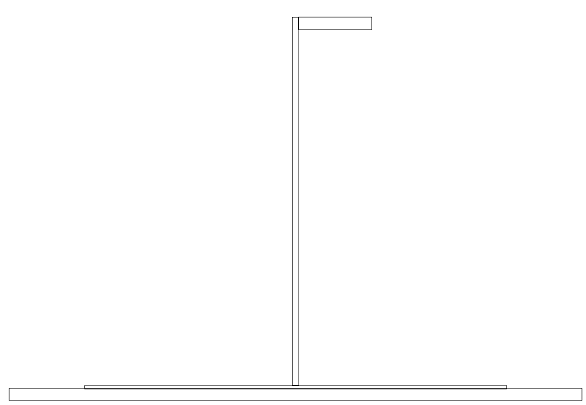

Figure 6.10: Example 2 – Panel 3 final design

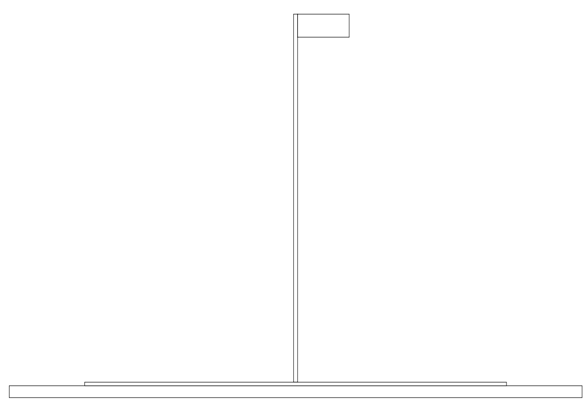

Figure 6.11: Example 2 – Panel 4 final design

Chapter 7

Conclusions and Recommendations

7.1 Conclusions

An analysis capability for the geometrically non-linear response of compressively loaded prismatic plate structures was developed. Both the "full" finite strip solution procedure and the "reduced" solution procedure were successfully implemented in a FORTRAN 90 computer code designated `NLISA`. Verification test cases included a variety of isotropic and composite flat plates as well as a blade stiffened panel. Comparisons were made with results available in the literature, and both the full and reduced `NLISA` analyses were demonstrated to provide accurate results for displacement and strain quantities through moderately large postbuckling loads.

The "full" method is a non-linear finite strip analysis of the semi-analytical multi-term type. Displacement fields are approximated in the longitudinal direction using trigonometric series and using cubic polynomials in the transverse direction. Individual finite strips are modeled as balanced, symmetric orthotropic laminated composite materials, and the resulting structure is loaded by uniaxial or biaxial compression. The boundary conditions at the loaded ends are simply supported out-of-plane, while a variety of in-plane and out-of-plane boundary conditions may be modeled at the unloaded edges. Geometric shape imperfections are permitted. The reduced solution method makes use of a reduced basis method in conjunction with the foregoing finite strip analysis. Here, the (potentially large) set of non-linear algebraic equations produced by the finite strip method are replaced by a small set of system equations. In the present implementation, the basis vectors consist of successive derivatives of the non-linear system equations with respect to the loading parameter, λ. A weighted norm of the full residual vector, e, is used to determine whether or not to generate a new set of basis vectors. If this norm is greater than a user specified tolerance, $\hat{e}$, a new set of basis vectors is generated before proceeding with the solution procedure; otherwise, the reduced solution procedure continues with the current set of basis vectors.

Depending on the nature of the problem, the reduced solution procedure is capable of computational savings of 60%+ compared to the full solution procedure. For any given analysis performed with the full solution method, there are two major tasks which take up most of the CPU time: (1) the factorization of the assembled system matrices and (2) the formation of the strip level non-linear stiffness matrices. The reduced solution method can significantly reduce the number of times that the (full) system matrices must be factored, but has no effect on the number of times in which the local stiffness matrices are formed. As a consequence, the reduced method is most effective in reducing the computational cost of the full method when the most significant portion of the cost of the original (full) problem is matrix factorization. In particular, the ratio, C_f, of the cost of matrix factorization to the cost of matrix formation is a rough indicator of the potential effectiveness of the reduced solution procedure. If this ratio (for the full problem) is large (> 1), the reduction in the cost of factorization will offset the costs of generating basis vectors, and the reduced solution procedure will be effective in reducing the overall computational cost. In general, a larger C_f will lead to larger computational savings. If, on the other hand, C_f (for the full problem) is small (≤ 1), the reduction in factorization costs will be offset by the costs of generating basis vectors, and the reduced method will be as costly (or more costly) compared to the full solution method. In general, then, the reduced solution method is most effective for problems with large numbers of finite strips. As the number of finite strips is increased, the cost of forming the local stiffness matrices increases linearly, while the factorization cost of the global stiffness matrix increases at a greater rate. The addition of longitudinal terms increases the costs of both the full and reduced solution procedures, but has little effect on their relative efficiencies.

In addition to the above considerations, the efficiency and robustness of the reduced solution method was found to be sensitive to the user specified error norm, $\hat{e}$, used during the solution procedure to determine when to generate new basis vectors. If $\hat{e}$ is too large, new sets of basis vectors are not generated when they are needed and the solution procedure either diverges or generates erroneous results. If $\hat{e}$ is too small, new sets of basis vectors are generated more often than they are needed, and the computational cost of the solution procedure increases. There is no fixed value for $\hat{e}$ that is best for all problems, although a value near $\hat{e} = 0.010$ appears to be a reasonable initial guess. The full solution procedure was found to be very robust for all the examples considered.

In parallel with the above effort, a new method for performing global/local design optimization of large complex structures (such as aircraft wings or fuselages) was developed. Using the McDonnell Douglas finite element code `ADOP` as a testbed, a simple but flexible interface between the global and local design optimization levels was constructed using response surface methods. The interface is structured so as to minimize the changes required in either the existing global design code or the local design code(s). Proper coupling is maintained between the global and local design levels via a "weight constraint" and the transfer of global stiffness information to the local design code. The method was verified using a simple global wing model (global level) and the panel design code `PASCO` (local level). `PASCO` is capable of generating optimal panel designs based on linear structural analysis.

7.2 Future Work

The next logical step in this line of research is to combine the two parallel threads of the present work: use the non-linear analysis capabilites developed here in the context of global/local design. The first step would be to wrap an optimizer around the non-linear analysis; this would allow optimal local panel designs to be generated based on non-linear analysis. The process of wrapping an optimizer around a complex analysis package is not necessarily trivial, as optimizers inevitably reveal and exploit any weaknesses in the analysis. Once developed, the optimal local designs could then be used to generate the response surface approximations required by the global/local design procedure.

With this general course of action in mind, the following specific recommendations for improving and refining the `NLISA` analyses are made:

- Investigate alternative formulations for the error norm, e. As presently implemented, it is difficult for the user to know ahead of time what value of $\hat{e}$ should be chosen so as to maximize the computational efficiency of the reduced solution procedure. An alternative formulation for e may result in a $\hat{e}$ value that is more problem independent.

- Modify the `NLISA` code so that the user may arbitrarily select the longitudinal terms to be included in a given analysis. At present, the user is restricted to choosing an ordered set of terms (such as terms 2 to 10 in steps of 4). Because the total number of longitudinal terms has a large influence on the computational cost, this action may allow the computational costs of both the full and reduced solution procedures to be reduced significantly for certain problems.

- Modify the finite strip formulation to include shear loading and additional boundary conditions at the loaded edges of the structure. This would make the analysis more suitable for use as a general purpose panel analysis and design code.

- Incorporate curved strips in the analysis. This would make the analysis more suitable for analyzing shell structures, such as are found in aircraft fuselages.

Bibliography

[1] Sharma, A.K., Sikes, G.D., Loikkanen, M.J., and Tzong, T.J.,"Aeroelastic Design Optimization Program (ADOP) Users Manual Version 1.1", McDonnell Douglas Report Number MDC92K0408, January 22, 1993.

[2] Stroud, W.J., and Anderson, M.S.,"PASCO: Structural Panel Analysis and Sizing Code, Capabilities and Analytical Foundations", NASA TM 80181, November, 1981.

[3] Dawe, D.J., Lam, S.E., and Azizian, Z.G.,"Non-linear Finite Strip Analysis of Rectangular Laminates Under End Shortening, Using Classical Plate Theory", International Journal for Numerical Methods in Engineering, Vol. 35, pp. 1087-1110, 1992.

[4] Noor, A.K., Peters, J.M., and Anderson, C.M.,"Two-Stage Rayleigh-Ritz Technique for Nonlinear Analysis of Structure", In *Innovative Numerical Analysis for the Applied Engineering Sciences, Proceedings of the Second International Symposium on Innovative Numerical Analysis in Applied Engineering Science*, June 16-20, 1980, Montreal, Canada, pp. 743-753. University Press of Virginia, Charlottesville, Virginia, 1980.

[5] Noor, Ahmed K.,"Recent Advances in Reduction Methods for Nonlinear Problem", *Computers and Structures*, Vol. 13, pp. 31-44, 1981.

[6] Budiansky, B., and Hutchison, J.W.,"Buckling: Progress and Challenges", from *Trends in Solid Mechanics 1979*, Ed., J.F. Besseling and A.M.A. van der Heijden, Delft University Press, Sijthoff and Noordhoff Int'l Pub., pp. 93-116, 1979.

[7] Stoll, F., Gürdal, Z., and Starnes, J.H. Jr.,"A Method for the Geometrically Nonlinear Analysis of Compressively Loaded Prismatic Composite Structure", Report No. CCMS-91-03 (VPI-E-91-01), Center for Composite Materials and Structures, Virginia Polytechnic Institute and State University, Blacksburg, VA, 1991.

[8] Wittrick, W.H., and Williams, F.W.,"Buckling and Vibration of Anisotropic or Isotropic Plate Assemblies Under Combined Loading", *International Journal of Mechanical Science*, Vol. 16, 1973, pp. 209-239.

[9] Perry, C.A., Gürdal, Z., Starnes, J.H. Jr.,"Minimum Weight Design of Compressively Loaded Stiffened Panels for Postbuckling Response", *Engineering Optimization*, Vol. 28, 1997, pp. 175-197.

[10] Chia, Cheun-Yuan, "Geometrically Nonlinear Behavior of Composite Plates: A Review", *Applied Mechanics Review*, Vol. 41, No. 12, December, 1988, pp. 439-451.

[11] Dawe, D.J.,"Finite Strip Buckling and Postbuckling Analysis", In *Buckling and Postbuckling of Composite Plates*, Ed., G.J. Turvey and I.H. Marshall, Chapman and Hall, London, pp. 108-153, 1995.

[12] Wittrick, W.H., "General Sinusoidal Stiffness Matrices for Buckling and Vibration Analysis of Thin Flat-Walled Structures", *International Journal of Mechanical Science*, Vol. 10, pp. 946-966, 1968.

[13] Kantorovich, L.V., and Krylov, V.I., "Approximate Method of Higher Analysis", Interscience Publishers, 1958.

[14] Williams, F.W., and Wittrick, W.H., *International Journal of Mechanical Science*, Vol. 11, pp. 979, 1969.

[15] Cheung, Y.K., "The Finite Strip Method in the Analysis of Elastic Plates With Two Opposite Simply Supported Ends", *The Institution of Civil Engineers*, Vol. 40, pp. 1-7, 1968.

[16] Cheung, Y.K., "Finite Strip Method Analysis of Elastic Slabs", *Journal of the Engineering Mechanics Division*, ASCE, Vol. 94, pp. 1365-1378, 1968.

[17] Przemieniecki, J.S., "Finite Element Structural Analysis of Local Instability", *AIAA Journal*, Vol. 11, No. 1, pp. 33-39, January, 1973.

[18] Plank, R.J., and Wittrick, W.H., "Buckling Under Combined Loading of Thin, Flat-Walled Structures by a Complex Finite Strip Method", *International Journal for Numerical Methods in Engineering*, Vol. 8, pp. 323-339, 1974.

[19] Graves Smith, T.R., and Sridharan, S., "A Finite Strip Method for the Buckling of Plate Structures Under Arbitrary Loading", *International Journal of Mechanical Science*, Vol. 20, pp. 685-693, 1978.

[20] Cheung, M.S., and Cheung, Y.K., "Natural Vibrations of Thin Flat-Walled Structures with Different Boundary Conditions", *Journal of Sound and Vibration*, Vol. 18, No. 3, pp. 325-337, 1971.

[21] Mawenya A.S., and Davies, J.D., "Finite Strip Analysis of Plate Bending Including Transverse Shear Effects", *Building Science*, Vol. 9, pp. 175-180, 1974.

[22] Benson, P.R., and Hinton, E., "A Thick Finite Strip Solution for Static, Free Vibration and Stability Problems", *International Journal for Numerical Methods in Engineering*, Vol. 10, pp. 665-678, 1976.

[23] Lau, S.C.W., and Hancock, G.J., "Buckling of Thin Flat-Walled Structures by a Spline Finite Strip Method", *Thin Walled Structures*, Vol. 4, pp. 269-294, 1986.

[24] Cheung, Y.K., and Fan, S.C., "Static Analysis of Right Box Girder Bridges by Spline Finite Strip Method", *Proceedings of the Institute of Civil Engineers*, Vol. 75, pp. 311-323, 1983.

[25] Lau, S.C.W., and Hancock, G.J., "Inelastic Buckling Analyses of Beams, Columns, and Plates Using the Spline Finite Strip Method", Vol. 7, pp. 213-238, 1989.

[26] Dawe, D.J., "Finite Strip Buckling Analysis of Curved Plates Assemblies Under Biaxial Loading", *International Journal of Solids and Structures*, Vol. 13, pp. 1141-1155, 1977.

[27] Morris, I.R., and Dawe, D.J., "Free Vibration of Curved-Plate Assemblies with Diaphragm Ends", *Journal of Sound and Vibration*, Vol. 73, pp. 1-17, 1980.

[28] Mohd, S., and Dawe, D.J., "Buckling and Vibration of Thin Laminated Composite Prismatic Shell Structures", *Composite Structures*, Vol. 25, pp. 353-362, 1993.

[29] Mohd, S., and Dawe, D.J., "Finite Strip Vibration Analysis of Composite Prismatic Shell Structures with Diaphragm Ends", *Computers and Structures*, Vol. 49, pp. 753-765, 1993.

[30] Graves Smith, T.R., and Sridharan, S., "A Finite Strip Method for the Post-Locally-Buckled Analysis of Plate Structures", *International Journal for Numerical Methods in Engineering*, Vol. 20, pp. 833-842, 1978.

[31] Sridharan, S., and Graves-Smith, T.R., "Postbuckling Analyses with Finite Strips", *Journal of the Engineering Mechanics Division*, ASCE., Vol. 107, No. EM5, October, 1981, pp. 869-888.

[32] Donnell, L.H., *Beams, Plates, and Shells*, McGraw-Hill, New York, 1976.

[33] Hancock, Gregory J., "Nonlinear Analysis of Thin Sections in Compression", *Journal of the Structural Division*, ASCE, Vol. 107, No. ST3, pp. 455-471, 1981.

[34] Kakol, Witold, "Stability Analysis of Stiffened Plates by Finite Strips", *Thin-Walled Structures*, Vol. 10, pp. 277-297, 1990.

[35] Azizian, Z.G., and Dawe, D.J., "Geometrically Nonlinear Analysis of Rectangular Mindlin Plates Using the Finite Strip Method", *Computers and Structures*, Vol. 21, pp. 423-436, 1985.

[36] Dawe, D.J., and Azizian, Z.G., "The Performance of Mindlin Plate Finite Strips in Geometrically Nonlinear Analysis", *Computers and Structures*, Vol. 23, pp. 1-14, 1986.

[37] Dawe, D.J., Lam, S.S.E., and Azizian, Z.G., "Nonlinear Finite Strip Analysis of Rectangular Laminates Under End Shortening, Using Shear Deformation Plate Theory", *International Journal for Numerical Methods in Engineering*, Vol. 36, pp. 1045-1064, 1993.

[38] Dawe, D.J., Lam, S.S.E., and Azizian, Z.G., "Finite Strip Post-Local-Buckling Analysis of Composite Prismatic Plate Structures", *Computers and Structures*, Vol. 48, pp. 1011-1023, 1993.

[39] Nagy, D.A., "Modal Representation of Geometrically Nonlinear Behavior by the Finite Element Method", *Computers and Structures*, Vol. 10, pp. 683-688, 1979.

[40] Almroth, B.O., Stern, P., and Brogan, F.A., "Automatic Choice of Global Shape Functions in Structural Analysis", *AIAA Journal*, Vol. 16, pp. 525-528, 1978.

[41] Noor, A.K., and Peters, J.M., "Reduced Basis Technique for Nonlinear Analysis of Structures", *AIAA Journal*, Vol. 18, No. 4, pp. 455-462, 1980.

[42] Thompson, J.M.T, and Walker, A.C., "The Non-Linear Perturbation Analysis of Discrete Structural Systems", *International Journal of Solids and Structures*, Vol. 4, pp. 757-768, 1968.

[43] Bergan, P.G., Holand, I., and Søreide, T.H., "Use of the Current Stiffness Parameter in the Solution of Nonlinear Problems", In *Energy Methods in Finite Element Analysis*, pp. 265-282, Wiley, New York, 1979.

[44] Noor, A.K., and Peters, J.M., "Recent Advances in Reduction Methods for Instability Analysis of Structures", *Computers and Structures*, Vol. 16, pp. 67-80, 1983.

[45] Noor, A.K., Andersen, C.M., and Peters, J.M., "Reduced Basis Technique for Collapse Analysis of Shells", *AIAA Journal*, Vol. 19, No. 3, pp. 393-397, 1981.

[46] Noor, A.K., and Peters, J.M., "Bifurcation and Post-Buckling Analysis of Laminated Composite Plates Via Reduced Basis Technique", *Computer Methods in Applied Mechanics and Engineering*, Vol. 29, pp. 271-295, 1981.

[47] Stroud, J.S., and Agranoff, N., "Minimum Mass Design of Filamentary Composite Panels Under Combined Loads: Design Procedure Based in Simplified Buckling Equations", NASA TN-D-8257, 1977.

[48] Swanson, G.D., and Gürdal, Z., "Structural Efficiency Study of Graphite-Epoxy Aircraft Rib Structures", *Journal of Aircraft*, Vol. 27, No. 12, 1990, pp. 1011-1020.

[49] Sobieszczanski-Sobieski, J., "An Integrated Computer Procedure for Sizing Composite Airframe Structures", NASA TP-1300, 1979.

[50] Starnes, J.H., Jr., and Haftka, R.T., "Preliminary Design of Composite Wings for Buckling, Strength, and Displacement Constraints", *Journal of Aircraft*, Vol. 16, 1979, pp. 564-570.

[51] Haftka, R.T, and Starnes, J.H., Jr., "WIDOWAC (Wing Design Optimization With Aeroelastic Constraints): Program Manual", NASA TM-X-3071, 1974.

[52] Schmit, L.A., and Mehrinfar, M., "Multilevel Optimum Design of Structures with Fiber-Composite Stiffened-Panel Components", *AIAA Journal*, Vol. 20, No. 1, 1980.

[53] Watkins, R.I., "Optimal Design of Large Laminated Structures", ICAS Paper No. 88 1.10.2, 1988, pp. 1480-1486.

[54] Frederick, D., Chang, T.S., *Continuum Mechanics*, Scientific Publishers, Inc., Cambridge, MA, 1965.

[55] Jones, R.M., *Mechanics of Composite Materials*, Hemisphere Publishing Corporation, New York, 1975.

[56] Zienkiewicz, O.C., *The Finite Element Method, Third Edition*, McGraw Hill, London, 1977, pp. 1-18.

[57] Stewart, C.B. (compiler), *The Computational Structural Mechanics Testbed Procedures Manual*, NASA TM 100646, December, 1991.

[58] Crisfield, M.A., "A Fast Incremental/Iterative Solution Procedure That Handles 'Snap-Through' ", *Computers and Structures*, Vol. 13, pp. 55-62, 1981.

[59] Thompson, J.M.T. and Hunt, G.W., *A General Theory of Elastic Stability*, John Wiley and Sons, New York, 1973.

[60] Golub, Gene, H., and Van Loan, Charles F., *Matrix Computations*, 2nd Edition, The Johns Hopkins University Press, Baltimore, 1989.

[61] Shin, D.K., "Minimum-Weight Design of Symmetrically Laminated Composite Plates for Postbuckling Performance under In-plane Compression Loads", Ph.D. dissertation, Engineering Science and Mechanics Department, Virginia Polytechnic Institute and State University, September, 1990.

[62] Marguerre, K., "The Apparent Width of Plates in Compression", NACA-TM-833, 1937.

[63] Starnes, J.H. Jr., and Rouse, M., "Postbuckling and Failure Characteristics of Selected Flat Rectangular Graphite-Epoxy Plates Loaded in Compression", AIAA Paper 81–0543, April, 1981.

[64] Engelstad, S.P., Reddy, J.N., and Knight, N.F., "Postbuckling Response and Failure Prediction of Graphite-Epoxy Plates Loaded in Compression", *AIAA Journal*, Vol. 30, No. 8, August, 1992.

[65] Almroth, B.O., Brogran, F.A., and Stanley, G.M., "Users Manual for STAGS – Volume I: Theory", NASA CR-165670, March, 1978.

[66] Almroth, B.O., Brogan, F.A., and Stanley, G.M., "Structural Analysis of General Shells – Volume II: User Instructions for STAGSC-1", LMSC-D633873, Applied Mechanics Lab., Lockheed Palo Alto Research Lab, Palo Alto, CA, December, 1982, updated 1985.

[67] Bushnell, D., "PANDA2 – Program for Minimum Weight Design of Stiffened, Composite, Locally Buckled Panels", *Computers and Structures*, Vol. 25, No. 4, 1987, pp. 469-605.

[68] Thurston, G.A., Brogan, F.A., and Stehlin, P., "Postbuckling Analysis Using a General-Purpose Code", AIAA Paper No. 85-0719-CP, *Proceedings of the AIAA 26th Structures, Structural Dynamics, and Materials Conference*, Orlando, Florida, 15-17 April 1985.

[69] Box, G.P., and Draper, N.R., *Empirical Model-Building and Response Surfaces*, John Wiley and Sons, New York, 1987.

[70] Narducci, R., Grossman, B., Valorani, M., Dadone, A. and Haftka, R.T., "Optimization Methods for Non-smooth or Noisy Objective Functions in Fluid Design Problems", *Proceedings of the AIAA 12th Computational Fluid Dynamics Conference*, Paper No. 95-1648-CP, June 1995.

[71] Vanderplaats, G.N., "ADS-A FORTRAN Program for Automated Design Synthesis – Version 1.10", NASA CR–177985, 1985.

Appendix A

Derivation of an Entry in the K_{ij}^2 Matrix

As noted in Chapter 3, the tangent stiffness matrix for a finite strip, $\bar{K}_{ij}^t$, may be written in the following convenient form:

$$\bar{K}_{ij}^t = \bar{K}_{ij} + \lambda \bar{K}_{ij}^* + \bar{K}_{ij}^1 + \bar{K}_{ij}^2. \tag{A.1}$$

where $\bar{K}_{ij}$, $\bar{K}_{ij}^*$, $\bar{K}_{ij}^1$, and $\bar{K}_{ij}^2$ are all symmetric matrices. $\bar{K}_{ij}$ and $\bar{K}_{ij}^*$ are matrices of constants (for a given finite strip), while $\bar{K}_{ij}^1$ is a linear function of the unknown coefficients and $\bar{K}_{ij}^2$ is quadratic in the unknown coefficients. In terms of these system matrices, the total potential energy is:

$$\Pi = \lambda x_j^T \bar{q}_i + x_i^T (\bar{K}_{ij} + \lambda \bar{K}_{ij}^*) x_j + \frac{1}{6} x_i^T \bar{K}_{ij}^1 x_j + \frac{1}{12} x_i^T \bar{K}_{ij}^2 x_j, \tag{A.2}$$

and the corresponding equilibrium equations are:

$$\lambda \bar{q}_i + (\bar{K}_{ij} + \lambda \bar{K}^*_{ij} + \frac{1}{2}\bar{K}^1_{ij} + \frac{1}{3}\bar{K}^2_{ij})x_j = 0. \tag{A.3}$$

In this appendix, the stiffness entries corresponding to a representative term in the potential energy expression are derived. A similar derivation must be performed for each term in the potential energy expression; the present derivation is presented in order to give the flavor of the general procedure. The potential energy term that will be examined is:

$$\Pi_1 = \frac{1}{4}A_{12}\int_0^L \int_{-b/2}^{b/2} (\frac{\partial u}{\partial y})^2 (\frac{\partial w}{\partial x})^2 \, dx \, dy. \tag{A.4}$$

This term is quadratic in the displacements, and will produce entries in the $\bar{K}^2_{ij}$ non-linear stiffness matrix. Recall the expressions for the u and w displacement fields:

$$u(x,y) = \lambda \hat{\epsilon}_{xl}(x - \frac{L}{2}) + \sum_{k=1}^{Kmax}\sum_{p=1}^{4} N_p(y) u_{pl} \sin(\frac{k\pi x}{L}) \tag{A.5}$$

$$w(x,y) = \sum_{n=1}^{Nmax}\sum_{p=1}^{4} M_p(y) w_{pn} \sin(\frac{n\pi x}{L}) \tag{A.6}$$

where

$$N_1(y) = (-\frac{1}{16} + \frac{y}{8b} + \frac{9y^2}{4b^2} - \frac{9y^3}{2b^3}) \tag{A.7}$$

$$N_2(y) = (\frac{9}{16} - \frac{27y}{8b} - \frac{9y^2}{4b^2} + \frac{27y^3}{2b^3}) \tag{A.8}$$

$$N_3(y) = (\frac{9}{16} + \frac{27y}{8b} - \frac{9y^2}{4b^2} - \frac{27y^3}{2b^3}) \tag{A.9}$$

$$N_4(y) = (-\frac{1}{16} - \frac{y}{8b} + \frac{9y^2}{4b^2} + \frac{9y^3}{2b^3}) \tag{A.10}$$

and

$$M_1(y) = (\frac{1}{2} - \frac{3y}{2b} + \frac{2y^3}{b^3}) \tag{A.11}$$

$$\begin{aligned} M_2(y) &= \left(\frac{b}{8} - \frac{y}{4} - \frac{y^2}{2b} + \frac{y^3}{b^2}\right) && \text{(A.12)} \\ M_3(y) &= \left(\frac{1}{2} + \frac{3y}{2b} - \frac{2y^3}{b^3}\right) && \text{(A.13)} \\ M_4(y) &= \left(-\frac{b}{8} - \frac{y}{4} + \frac{y^2}{2b} + \frac{y^3}{b^2}\right). && \text{(A.14)} \end{aligned}$$

The derivatives $\frac{\partial u}{\partial y}$ and $\frac{\partial w}{\partial x}$ are:

$$\begin{aligned} \frac{\partial u}{\partial y} &= \sum_{k=1}^{Kmax} \sum_{p=1}^{4} N_p'(y) u_{pl} \sin\left(\frac{k\pi x}{L}\right) && \text{(A.15)} \\ \frac{\partial w}{\partial x} &= \sum_{n=1}^{Nmax} \sum_{p=1}^{4} \frac{n\pi}{L} M_p(y) w_{pn} \cos\left(\frac{n\pi x}{L}\right) && \text{(A.16)} \end{aligned}$$

where the ($\prime$) superscript denotes differentiation with respect to y. Substituting these expressions into the potential energy expression (A.4) yields the following:

$$\begin{aligned} \Pi_1 = \; & \frac{1}{4} A_{12} \int_0^L \int_{b/2}^{b/2} \sum_{k=1}^{Kmax} \sum_{p=1}^{Kmax} \sum_{n=1}^{Nmax} \sum_{q=1}^{Nmax} \Bigg\{ \frac{nq\pi^2}{L^2} \\ & (N_1' u_{1k} + N_2' u_{2k} + N_3' u_{3k} + N_4' u_{4k})(N_1' u_{1p} + N_2' u_{2p} + N_3' u_{3p} + N_4' u_{4p}) \cdot \\ & (M_1 w_{1n} + M_2 \psi_{1n} + M_3 w_{2n} + M_4 \psi_{2n})(M_1 w_{1q} + M_2 \psi_{1q} + M_3 w_{2q} + M_4 \psi_{2q}) \cdot \\ & \sin\left(\frac{k\pi x}{L}\right) \sin\left(\frac{p\pi x}{L}\right) \cos\left(\frac{n\pi x}{L}\right) \cos\left(\frac{q\pi x}{L}\right) \Bigg\} \, dx \, dy. && \text{(A.17)} \end{aligned}$$

Given this potential energy expression, the corresponding equilibrium equations are obtained by taking derivatives with respect to the unknown coefficients and equating the results to zero. For example, the equilibrium equation corresponding to row u_{1k} is:

$$\begin{aligned} & \frac{1}{2} A_{12} \int_0^L \int_{b/2}^{b/2} \sum_{k=1}^{Kmax} \sum_{p=1}^{Kmax} \sum_{n=1}^{Nmax} \sum_{q=1}^{Nmax} \Bigg\{ \frac{nq\pi^2}{L^2} N_1' (N_1' u_{1p} + N_2' u_{2p} + N_3' u_{3p} + N_4' u_{4p}) \cdot \\ & (M_1 w_{1n} + M_2 \psi_{1n} + M_3 w_{2n} + M_4 \psi_{2n})(M_1 w_{1q} + M_2 \psi_{1q} + M_3 w_{2q} + M_4 \psi_{2q}) \cdot \\ & \sin\left(\frac{k\pi x}{L}\right) \sin\left(\frac{p\pi x}{L}\right) \cos\left(\frac{n\pi x}{L}\right) \cos\left(\frac{q\pi x}{L}\right) \Bigg\} \, dx \, dy = 0. && \text{(A.18)} \end{aligned}$$

Contributions to the tangent stiffness matrix are obtained by differentiating the left hand side of this equation with respect to the unknown coefficients. For example, taking the derivative with respect to w_{1q}, we have:

$$
\begin{aligned}
&A_{12}\int_0^L \int_{b/2}^{b/2} \sum_{k=1}^{Kmax}\sum_{p=1}^{Kmax}\sum_{n=1}^{Nmax}\sum_{q=1}^{Nmax}\Big\{\frac{nq\pi^2}{L^2}\cdot \\
&N_1'M_1(N_1'u_{1p}+N_2'u_{2p}+N_3'u_{3p}+N_4'u_{4p})(M_1w_{1n}+M_2\psi_{1n}+M_3w_{2n}+M_4\psi_{2n})\cdot \\
&\sin(\frac{k\pi x}{L})\sin(\frac{p\pi x}{L})\cos(\frac{n\pi x}{L})\cos(\frac{q\pi x}{L})\Big\}\,dx\,dy.
\end{aligned}
\tag{A.19}
$$

This expression is the entry in $\bar{K}^2_{ij}$ corresponding to row u_{1k} and column w_{1q} (it also corresponds to row w_{1q} and column u_{1k}). Other entries in the $\bar{K}^2_{ij}$ matrix may be obtained in a similar manner.

Integration with respect to x is carried out analytically. In the present example,

$$
\int_0^L \sin(\frac{k\pi x}{L})\sin(\frac{p\pi x}{L})\cos(\frac{n\pi x}{L})\cos(\frac{q\pi x}{L})\,dx = \begin{cases} \pm\frac{L}{8} \\ 0 \end{cases}
\tag{A.20}
$$

depending on the values of n, q, k, and p. The (+) sign applies if $(p = n+q+k)$, $(k = p+n+q)$, $(n+k = q+p)$, or $(n+p = q+k)$. The (−) sign applies if $(n+q = k+p)$, $(n = q+k+p)$, or $(q = n+k+p)$. If none of these expressions are true, the integral is zero.

Integration with respect to y is carried out using eight point Gauss-Legendre quadrature. As the integrand is at most a 12th order polynomial, this procedure yields results that are exact to within the round-off error of the machine. Note that this numerical integration only needs to be performed once for each finite strip in the analysis; the integration is performed at the beginning of the analysis and the results are stored for later use.

Vita

Scott Alan Ragon Was born in 1966 in Hartford City, Indiana, where he spent most of his childhood. He graduated from high school in Fairless Hills, Pennsylvania in 1984. After receiving a B.S. in Aerospace Engineering from Virgina Tech in 1989, he worked as a stress engineer for General Dynamics in Fort Worth for several years. He received a M.S. in Engineering Mechanics from Virginia Tech in 1994.

Scott A. Ragon

October 7, 1998.